Collisions in Compact Star Clusters and formation of massive Black Holes

Francesco Paolo Rizzuto

München 2021

Collisions in Compact Star Clusters and formation of massive Black Holes

Francesco Paolo Rizzuto

Dissertation
der Fakultät für Physik
der Ludwig-Maximilians-Universität
München

vorgelegt von
Francesco Paolo Rizzuto
aus Palermo

München, den 13/09/2021

Erstgutachter: Prof. Dr. Simon D.M. White

Zweitgutachter: Porf. Dr. Andreas Burkert

Tag der mündlichen Prüfung: 01/12/2021

Contents

List of Figures

List of Tables

Zusammenfassung

Einige der beobachteten jungen Sternhaufen im lokalen Universum, wie MGG-11 und Arches, scheinen relativ große Massen ($> 10^4$ M$_\odot$) zu haben, die in einem kleinen Radius $R \lessapprox 1$ pc eingeschlossen sind. Es wird erwartet, dass Sternhaufen mit ähnlichen Eigenschaften auch bei höherer Rotverschiebung existieren, und sie könnten in jeder Galaxie innerhalb der LIGO/Virgo/Kraga-Empfindlichkeit zu finden sein. Das Innere dieser kompakten Systeme kann eine ausreichend hohe Dichte erreichen ($\gtrsim 10^5$M$_\odot$/pc^3), um eine große Anzahl von Kollisionen zwischen Stellaren-, und Schwarzen Löchern (BHs) hervorzurufen. Daher haben dichte stellare Umgebungen die Eigenschaft, dynamische Verschmelzungen kompakter Objekte auszulösen, die die Quellen der beobachtbaren Gravitationswellensignale (GW) sind. Aufgrund ihrer hohen Dichte ist ihre Entwicklung jedoch nur wenig durch direkte N-Körper-Simulationen erforscht. Diese Arbeit widmet sich der numerischen Erforschung solcher Systeme. Zu diesem Zweck haben wir drei Sätze direkter N-Körper-Simulationen junger kompakter Sternhaufen bei niedriger Metallizität durchgeführt und analysiert, wobei wir uns auf die Bildung von GW-Quellen und die Bildung massereicher BHs oberhalb des stellaren BH-Massenbereichs konzentriert haben. Im ersten Satz simulierten wir 80 Systeme von $N = 1,1 \times 10^5$ Teilchen mit 10% primordialen Binären, für 300 Myrs. Die Simulationen wurden mit dem direkten N-Körper-Algorithmus NBODY6++GPU durchgeführt. Die Sternhaufen hatten Anfangsmassen von $\sim 10^5$ M$_\odot$, anfängliche Halbmassenradien von $R_\mathrm{h} \lesssim 1$ pc und zentrale Dichten von über $\gtrsim 10^5$M$_\odot$pc^{-3}. Wir haben relativistische Korrekturen einbezogen, um den Gravitationswellen-Energieverlust von harten Doppelsternen zu berechnen. Die Ergebnisse zeigen, dass sehr massereiche Sterne (VMS) bis zu ~ 400 M$_\odot$ durch eine Reihe von schnellen stellaren Kollisionen schnell wachsen. In einigen Fällen absorbieren massearme BH bei engen Wechselwirkungen einen großen Teil solcher VMS und erreichen Massen im Bereich von ~ 100 M$_\odot$ bis zu 350 M$_\odot$. Im zweiten Satz haben wir 16 der 80 Realisierungen des ersten Satzes mit aktualisierten Entwicklungsvorgaben für massereiche Sterne neu simuliert. Die Aktualisierungen beinhalten metallizitätsabhängige stellare Winde und Behandlungen für pulsationspaarinstabile Supernovae (PPISNe). Diese neuen Vorschriften haben zur Folge, dass isolierte massereiche Sterne oberhalb von < 45 M$_\odot$ keine BHs bilden können. Da unsere simulierten Sternhaufen jedoch viele BHs und stellare Fusionsereignisse beherbergen, ist es nicht ungewöhnlich, dass sich BHs weit über dieser Massengrenze bilden. Insgesamt erzeugen die Simulationen mehrere Dutzend BH-BH-Kollisionen mit Massen, die den gleichen Massenbereich abdecken wie die aktuellen LIGO/Virgo/Kagra-GW-Detektionen. Zwei Simulationen ergaben Ereignisse mit primären (~ 90M$_\odot$) und sekundären (~ 60M$_\odot$) Massekomponenten, die mit der GW190521-Detektion kompatibel sind, was ein Entstehungsszenario für

derartige Verschmelzungen aufzeigt, dass in dichten stellaren Systemen mit niedrigen Fluchtgeschwindigkeiten möglich ist. Die dritte Gruppe von Simulationen wurde durchgeführt, um die Rolle zu untersuchen, die Gezeiteneinfangereignisse (TCE) bei der Bildung massereicher BHs spielen könnten. Wir fügten daher Gezeiteneinfangbehandlungen in den N-Körper-Code FROST ein und entwickelten 9 Simulationen von sehr kompakten Sternhaufen mit $N = 256.000$ Sternen, anfänglichen zentralen Dichten $10^5 \mathrm{M}_\odot/\mathrm{pc}^3 < \rho_\mathrm{c} < 10^8 \mathrm{M}_\odot/\mathrm{pc}^3$ und zentralen Dispersionsgeschwindigkeiten $20\mathrm{km/s} < \sigma_\mathrm{c} < 40\mathrm{km/s}$. Das Ergebnis dieser Simulationen zeigt, dass TCE die Anzahl der BH-Stern-Kollisionen erheblich erhöht. Bei Simulationen mit eingeschalteten Gezeiteneinfangvorgaben verdoppelt sich die BH-Stern-Fusionsrate. In 4 Simulationen haben wir die Sternhaufen mit einer zentralen 300 $\mathrm{M}_\odot$ BH, umgeben von massearmen Sternen, initiiert. Auch in solchen Systemen scheint TCE die Anzahl der Kollisionen mit dem massereichen BH zu erhöhen. Wenn Gezeiteneinfang-Vorschriften einbezogen werden, verdoppelt sich die BH-Massenwachstumsrate und erreicht ~ 20 $\mathrm{M}_\odot$ /Myr in den dichtesten Systemen.

Abstract

Some of the observed young clusters in the local Universe, such as MGG-11 and Arches, appear to have relatively high masses ($> 10^4$ M$_\odot$) enclosed in a small radius $R \lesssim 1$ pc. Clusters with similar properties are expected to exist also at higher redshift and they could be located in any galaxy within the LIGO/Virgo/Kagra sensitivity. The inner part of these compact systems can reach high enough densities ($\gtrsim 10^5 \mathrm{M}_\odot/\mathrm{pc}^3$) to induce a large number of stellar and black hole (BH) collisions. Therefore, dense stellar environments have the attractive characteristic to be able to trigger dynamically compact object mergers, which are the sources of the observable gravitational wave (GW) signals. However, due to their high densities, they are computationally very expensive to simulate. For this reason, their evolution remains little explored through direct N-body simulations. This thesis is dedicated to the numerical exploration of such systems. We carried out and analyzed three sets of direct N-body simulations of young compact star clusters at low metallicity, focusing our attention on the formation of GW sources and massive BHs above the stellar mass BH range. In the first set, we simulated 80 systems of $N = 1.1 \times 10^5$ particles with 10% primordial binaries, for 300 Myrs. The simulations have been carried out using the direct N-body algorithm NBODY6++GPU. The clusters had initial masses of $\sim 10^5$ M$_\odot$, initial half-mass radii $R_\mathrm{h} \lesssim 1$ pc and central densities exceeding $\gtrsim 10^5 \mathrm{M}_\odot \mathrm{pc}^{-3}$. We included relativistic corrections to compute the gravitational wave energy loss of hard binaries. The results show that very massive stars (VMSs) up to ~ 400 M$_\odot$ grow rapidly through a series of rapid stellar collisions. In some cases, low mass BH absorb a large fraction of such VMSs during close interactions, and reach masses in the range between $\sim 100 \mathrm{M}_\odot$ up to 350 M$_\odot$. In the second set, we re-simulated 16 of the 80 realizations of the first set with updated evolution prescriptions for massive stars. The updates incorporate metallicity dependent stellar winds and treatments for pulsations pair-instability supernovae (PPISNe). As a consequence of these new prescriptions, isolated massive stars cannot form BHs above < 45 M$_\odot$. Nevertheless, since our simulated clusters host many BHs and stellar merger events, it is not uncommon to form BHs well above this mass limit. Altogether, the runs generate several tens of BH - BH collisions with masses that cover the same mass range of the current LIGO/Virgo/Kagra GW detections. Two realizations produced events with primary ($\sim 90 \mathrm{M}_\odot$) and secondary ($\sim 60 \mathrm{M}_\odot$) mass components compatible with the GW190521 detection, revealing a formation scenario for such mergers feasible in dense stellar systems with low escape velocities. We realize the third set of simulations to investigate the role tidal capture events (TCE) may play in the formation of massive BHs. We therefore inserted tidal capture treatments in the N-body code FROST and ran 9 simulations of very compact star clusters with $N = 256.000$ stars, initial central densities $10^5 \mathrm{M}_\odot/\mathrm{pc}^3 < \rho_\mathrm{c} < 10^8 \mathrm{M}_\odot/\mathrm{pc}^3$ and central dispersion velocities 20km/s $< \sigma_c <$ 40km/s. The outcome of these runs indicates TCE increase considerably the number of BH - star to collisions. Some realizations with tidal capture prescriptions switched on, double the BH - star merger rate. In 4 runs we initiated the clusters with a central 300 $M_\odot$ BH surrounded by low mass stars. Also in such systems, TCEs seem to boost the number of collisions experienced by the massive BH. When tidal capture prescriptions are included, the BH mass growth rate increases by $\sim$ 13% reaching 20 $M_\odot$ /Myr in the densest systems.

Chapter 1

Introduction

Thanks to the groundbreaking advancements of LIGO/Virgo/Kagra detectors we are able to obtain valuable data on previously unobservable astrophysical events. Already a few dozen of detected gravitational wave (GW) signals (Abbott et al., 2020) originating from the collision of compact objects (see Fig. 1.1), such as black holes (BHs) and neutron stars (NSs), have given us unexpected new insights that helped shaping our current understanding of the evolution of massive stars. At the same time they open up challenging questions that are pushing the scientific community to explore new frontiers of theoretical astrophysics (see Mapelli, 2021, for a complete review).

The very fact that two BHs manage to collide within a Hubble time ($t_{\rm Hubble} \sim 10$ Gyr) is not easy to explain with standard binary evolution models. The separation required for a binary of 30 $M_\odot$ BHs moving on a circular orbit, to merge in a Hubble time, is $\sim 40\,R_\odot$. Creating stellar BH binaries with such a small separation is challenging. For instance, we cannot naively assume that they originate from pre-existing stellar binaries of massive stars. In fact, once the massive stars reach the giant phase, their radii expand up to $\sim 5 \times 10^2\,R_\odot$. Therefore, if massive stars form binaries with an initial separation of $\lesssim 500\,R_\odot$ they would simply overlap during their giant phase, thus merging into a single star before collapsing into BHs. Only binaries with a larger initial semi-major axis would survive the giant stage, leaving BH components with a separation never less than a few $\sim 10^2\,R_\odot$. Since the coalescence time due to gravitational radiation, is proportional to the fourth power of the semi-major axis $t_{\rm coal} \propto a^4$, the BHs in these binaries are expected to merge in at least $\sim 10^4 t_{\rm Hubble}$!

It follows that one of the main theoretical challenges to be faced is to envisage plausible mechanisms to bring two compact objects in the range of separations where gravitational radiation is strong enough to lead to coalescence in a timescale comparable to the age of the Universe. A popular scenario to produce BH binaries with a small semi-major axis from pre-existing stellar binaries assumes that when one of the two stars becomes a red giant they do not merge. Instead, they evolve in a common envelope phase until the naked helium core of the giant undergoes a supernovae explosion and collapses into a BH. If the binary survives the supernovae, the other massive star also becomes a giant and might enter once again a common envelope phase with the newly formed BH. Because of the viscosity exerted by the envelope, the two objects lose angular momentum and spiral in. Consequently, a BH binary, with a small separation, can form as soon as the second helium core becomes a BH as well. This formation channel is very intricate. It depends on many not well-understood details of stellar physics. It is therefore not yet possible to determine quantitatively how efficiently such a scenario can lead to compact objects colliding (Belczynski, 2020).

An alternative mechanism is the dynamical formation channel. Compact object mergers might be triggered by interactions with external bodies. For instance, hierarchical perturbations of a third object[1] can excite the eccentricity of a binary (Lidov, 1962; Kozai, 1962; Heggie, 1975), and therefore can shorten the expected coalescence timescale since $t_{\rm coal} \propto a^4(1-e)^{7/2}$ (for $e \approx 1$). In addition, BH binaries tend to shrink their semi-major axis when experiencing frequent chaotic encounters[2] with single stars or other binaries (Heggie, 1975). In summary, a non-isolated BH binary can rapidly reach the GW regime through both hierarchical and chaotic interactions.

There are several ways we can discriminate whether a BH merger originates from the dynamical or the common envelope channel. Already the mass range of the two components can give some indication. For instance, the observed event GW190521 involves unexpectedly massive BH components (Abbott et al., 2020). Both these two objects exceed the accepted mass limit for a stellar BH ($\sim 50\,\mathrm{M}_\odot$) suggesting that GW190521 might have been produced dynamically through multiple collisions. This hypothesis is further confirmed by the residual eccentricity observed in GW190521 (Romero-Shaw et al., 2020; Gayathri et al., 2020). The dynamical scenario, contrary to the common envelope channel, can easily explain this excess in eccentricity at the moment of coalescence. Another observed feature that can help to distinguish the two formation paths is the spin orientation between the two colliding objects: the common envelope produces BHs with aligned spin, in the dynamical channel the spins of the two BHs are randomly oriented.

At present, GW190521 is probably the only GW signal whose observed properties seem to favour the dynamical scenario, although the observational uncertainties still leave room for debate. For all the other detected BH coalescences, the constrain are not stringent enough. It is therefore impossible to infer any conclusions on their origin. Only with more accurate observations in combination with deep quantitative analysis of the astrophysical mechanisms that can lead to the collision of two compact objects, we might be able to correctly interpret and predict current and future GW detections.

1.1 Star clusters as nurseries of gravitational waves sources

As we mentioned earlier, BH binaries can significantly shorten their expected merging time through few-body interactions. Both long-range perturbations and close energetic encounters have the overall effect of shrinking the semi-major axes and increasing the eccentricity. This mechanism can be efficient as long as the binaries experience a large enough number of interactions in a short timescale. In other words, these binaries need to be located in sufficiently dense stellar environments such as star clusters. Star clusters, are very attractive systems to study, precisely

[1] In a hierarchical interaction between an intruder and a binary, the separation of the third object is significantly larger than the binary size.

[2] An intruder and a binary undergo a chaotic encounter when the size of the binary and the separation of the third object are comparable.

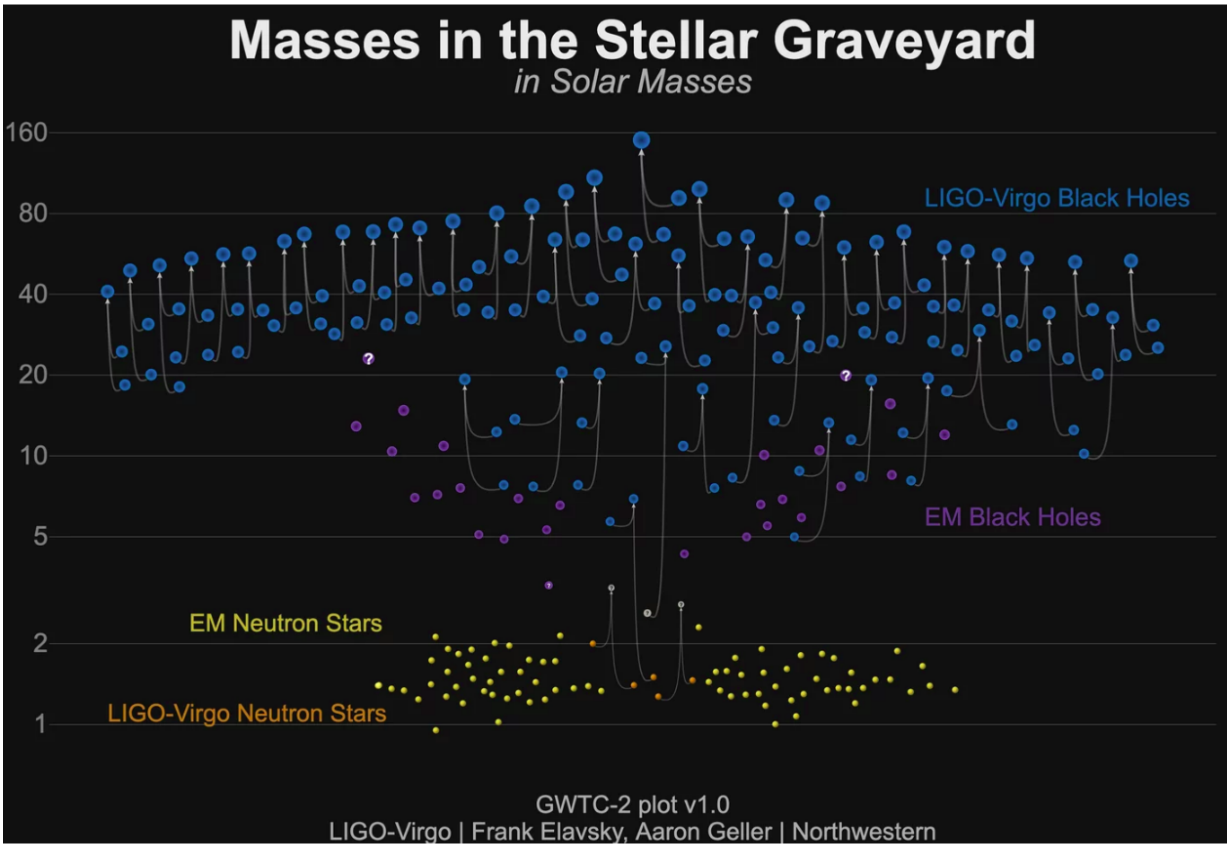

Figure 1.1: The collisions of compact objects discovered so far by LIGO/Virgo/Kagra detectors. The diagram shows in blue the BHs, in orange the NSs and compact objects of unknown nature in grey. Electromagnetic observations of BHs and NSs are illustrated respectively in violet and yellow. Credit: LIGO-Virgo / Northwestern University / Frank Elavsky & Aaron Geller.

because they are expected to generate and host a significant fraction of collisions between compact objects.

To determine the expected characteristics of GW sources triggered by a star cluster throughout its entire life, accurate N-body simulations are required. They, in fact, can provide reliable estimates on the compact object collision rate, and at the same time, they give detailed information on the mass range, mass ratio, eccentricity and spin of the colliding components.

The BH (and NS) coalescence spectrum spawned by a star cluster depends on the global attributes of the stellar system. Environments with different masses, radii, and central densities, are expected to give substantially different outcomes. Therefore, only a large sample of N-body simulations that explore the relevant parameter space of star cluster properties can yield quantitative constraints on the dynamical formation channel. In summary, numerical simulations of star clusters are expected to play a decisive role in achieving a deeper understanding of gravitational wave phenomenology.

1.2 Compact stellar systems as factories of massive objects

Among all stellar environments, compact star clusters are particularly interesting to look into. Both because they are expected to host a large number of gravitational wave sources, but also due to their high central densities, their inner region can reach extremely large collision rates, which in turn could lead to the formation of very massive stars (VMSs) and massive BHs. Due to their small sizes, compact star clusters have a very short mass segregation time. Hence, The most massive objects, such as stellar BHs and massive stars, rapidly sink into the inner part of the cluster where they can grow in mass through mergers (see Fig. 1.2 as an illustration). Such systems might uncover mechanisms that lead to the formation of intermediate-mass back holes (IMBHs) IMBHs have masses between $\gtrsim 100\ \mathrm{M}_\odot$ and $\lesssim 10^6\ \mathrm{M}_\odot$ or, in other words, their mass range is between stellar BHs and SMBHs. IMBHs are peculiar objects because, contrary to stellar BHs and SMBHs, there are only a few observations that reveal their existence. Probably the most convincing evidence is GW190521. Moreover, they are believed to power the most energetic observed X-ray sources (Kaaret et al., 2001; Farrell et al., 2009). Exploring IMBH formation scenarios can lead to the discovery of exotic GW sources that might be observed in the near future, and at the same time might provide new insights on understanding the origin of SMBHs.

1.3 Goal and structure of this work

With this thesis, we aim to explore the evolution of dense stellar environments such as compact star clusters by means of numerical methods. Specifically, we model stellar systems employing direct N-body codes. The latter computes every interaction between two particles directly and it adopts special regularization algorithms to integrate the evolution of close encounters. For this reason, direct N-body codes can follow with high accuracy not only the global evolution of the system but also the trajectory of each individual particle.

In the first chapter (Chap. 2) we give an overview of star cluster evolution. We aim to illustrate

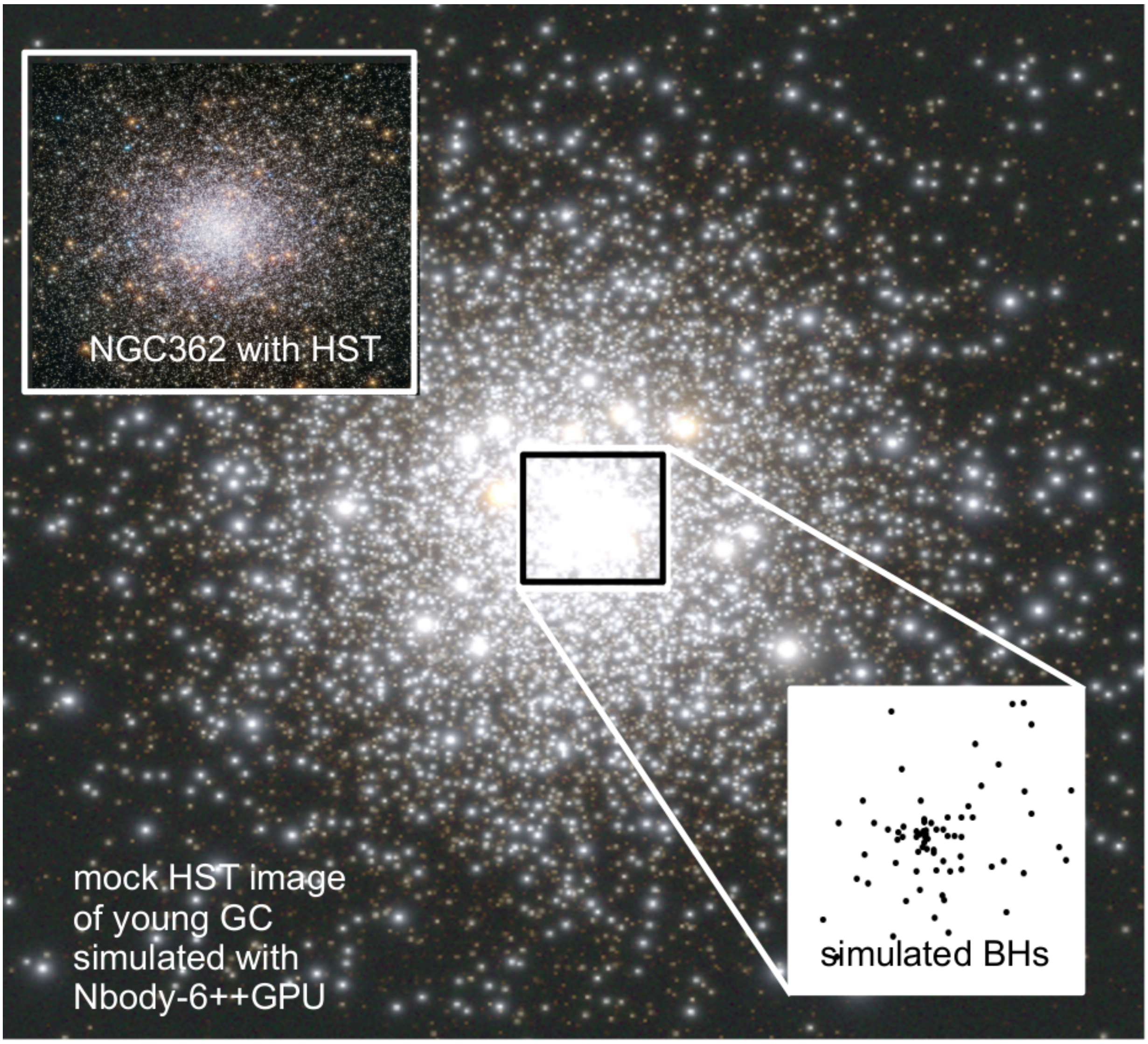

Figure 1.2: Compact star clusters are a promising environment for the formation of massive black holes and very massive stars. Due to their small sizes and high central density, massive objects (such as stellar black holes and massive stars) sink rapidly into the inner region where they can increase their mass through physical collisions and mass transfer events. The central image was created using a snapshot of one of the simulations presented in this thesis.

how the complex interplay between the mass loss from stellar winds, two-body relaxation effects and hard binaries regulate the overall evolution of these systems. In the same chapter, we explain how challenging it can be to build a direct numerical integrator for massive and compact star clusters and we explore the main issues that N-body algorithms need to solve to properly evolve such systems. Moreover, we discuss some of the most common numerical methods adopted to solve these problems.

In chapter 3 we run 80 N-body simulations of young compact star clusters with initial masses of about 10^5 $M_\odot$ and half mass radii ≤ 1.0 pc using the code NBODY6++GPU (Wang et al., 2015). We analyze the simulations focusing on the formation of massive BHs and intermediate-mass BHs (IMBHs[3]) through collisions.

In chapter 4 we repeat some of the simulations presented in chapter 3 but this time adopting updated recipes for the stellar evolution of massive stars. The updates include treatments for pulsation-pair instability supernovae (PPSN), pair-instability supernovae (PSN) and a new prescription for stellar winds. Also in this case the analysis of the simulations focuses on investigating the formation channels of massive BHs heavier than the most massive stellar BH that can be generated by an isolated star.

In chapter 5 we investigate the role that tidal capture might play in the formation of massive BHs. Using the direct N-body code FROST we run and analyze very compact star clusters with 256.000 particles and half mass radii ≤ 0.6 pc. In this last case, the simulations are initialized with an old stellar population to avoid the complexity of stellar evolution and focus on the dynamical evolution of the system. In the final chapter (Chap. 6), we discuss and summarise and discuss the main results of this Thesis.

[3]Hereafter, throughout the manuscript we will use the term IMBH to refer to the class of BHs with a mass in between 100 and 10^6 $M_\odot$.

Chapter 2

Theoretical background

2.1 Star Clusters

We devote this section to introduce the fundamental elements that govern the evolution of a star cluster. We will start giving a brief introduction on the properties of star clusters at their formation, when the system is still embedded in gas. We will then focus on the evolution of the cluster after gas ejection illustrating how the complex interplay between dynamical and stellar evolution shapes the structure of these systems.

2.1.1 Formation and early evolution

Star clusters are expected to form in massive turbulent molecular clouds where gas is rapidly converted into stars. The high level of turbulence in these stellar forming regions generates naturally small and irregular clumpy substructures leading to star formation spread throughout the whole cloud volume. Observations (Gutermuth et al., 2005; Sabbi et al., 2012) and numerical studies (Klessen, 2001; Bonnell & Bate, 2006) confirm the fractal-like structure of newly born clusters still embedded in the primordial gas from which their stars are forming. As shown by direct N-body simulations (Scally & Clarke, 2002; Hurley & Bekki, 2008), in about a **crossing time**[1] a violent relaxation erases all the initial clumpy substructures and leaves the cluster with a density profile compatible with the Elson, Fall, and Freeman (EFF) profile Elson et al. (1987). The EFF profile is more extended than the typical King density profile King (1966). The former describes clusters that were not affected by any external tidal force while the latter is more suitable to approximate tidally truncated clusters.

At the very beginning, gas and newly formed stars coexist in the same system. Once massive stars have formed, stellar feedback and stellar winds blow out a fraction of the gas, which is completely ejected after the last supernovae explosions. This process can be very violent and can lead to the complete dissolution of the clusters; only the most compact systems are capable to survive. For this reason, analytical studies suggest star clusters must be very compact at the time

[1] the dynamical time of a star cluster (also called **dynamical time**) is defined as $t_{\rm dyn} \sim \frac{R_h}{\sigma}$, where σ is the velocity dispersion of the cluster and R_h is its half-mass radius.

of their formation (Marks & Kroupa, 2012). Recent N-body simulations of embedded $\lesssim 10^4$ $M_\odot$ clusters confirm these results (Pelupessy & Portegies Zwart, 2012; Fujii et al., 2021). They also reveal that the gas gets removed completely from the cluster in a time scale of the order of 9 Myr, right after the explosion of the last massive stars.

At the same time, we observe the absence of dense gas in clusters such as Arches, Trumpler 14, and NGC 3603 despite being 2 Myr old (sse Portegies Zwart et al., 2010; Longmore et al., 2014, and citations therein). The gas in these systems is removed well before the first supernovae can occur ($\sim$ 3 Myr). This suggests another mechanism of gas removal. It is possible that in these clusters most of the gas is actually converted into stars and the gas is removed through exhaustion rather than ejection. This might work only if the initial gas density of the molecular cloud is high enough. In fact, in very dense gas regions, the stellar formation efficiency (SFE) attain high values freeing the clusters from its initial gas in a very short amount of time (see Longmore et al., 2014, for more details). Consequently, the clusters in question remain extremely compact, maintaining an effective radius of the order of $\lesssim 0.7$ pc.

In this section, we illustrated how clusters form and we described the very early stage of their evolution when gas and newly formed stars coexisted in the same system. We showed that clusters are likely to possess at the beginning an irregular hierarchical structure that is rapidly washed out by a violent relaxation phase leading to an approximately spherically symmetric configuration well described by an EFF or King density profile. We also showed how less compact clusters are likely to undergo an initial rapid expansion due to gas ejection while more compact one are expected to retain their initial sizes thanks to their high SFE: most of the gas is converted in stars leaving the system gas-free in a short amount of time. Given this, young massive and compact clusters are ideal systems to be followed with direct N-body simulations, in spite of the fact that they are little affected by processes associated with gas. In addition, they are the most interesting environments to investigate since they are likely to trigger a long chain of stellar collisions that lead to the formation of massive objects. For the rest of this thesis, we will focus our attention on these types of clusters, we will therefore neglect the impact of gas ejection in the early evolution of these systems and we will assume that the clusters maintain their initial compactness.

2.1.2 Evolution after gas removal

The evolution of an isolated star cluster is regulated by a complex interplay between stellar evolution and dynamical interactions. The former has a strong impact on the early phase, while the latter plays a major role in driving the long-term changes. We will discuss these two effects separately in the next two subsections. In the first subsection, we will briefly show when and how stellar evolution affects can impact the cluster structure. While in the second part we will focus our attention on the dynamical evolution, describing in detail how two-body and three-body interactions (hard binary + single star) shape the structure of the cluster over time.

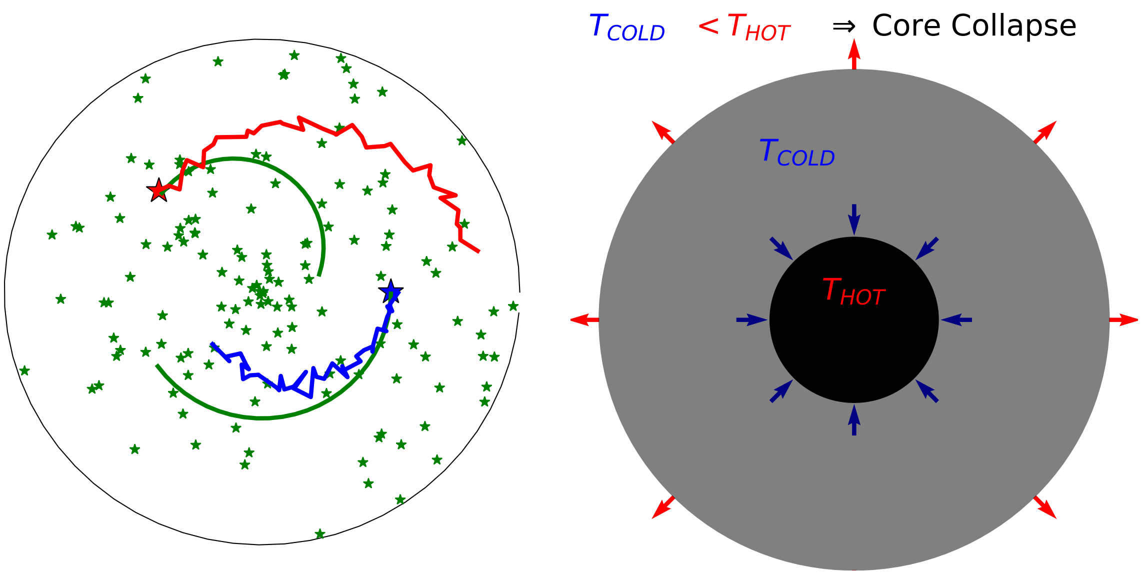

Figure 2.1: The plot on the left panel illustrates, with a cartoon, the trajectory of two particles embedded in a star cluster. The cumulative effect of two-body interactions forces the particles to deviate from their original trajectories dictated by the potential of the whole cluster (green trajectories). In addition, as a consequence of two-body encounters, a particle might lose kinetic energy and sink towards the centre (blue), or it might gain kinetic energy end move in the outer part of the system (red). The particle that loses energy during these interaction moving towards the centre convert potential energy into kinetic energy. Therefore, once they stabilize in an orbit closer to the centre they on the average move with higher velocity. The opposite consideration is true for particles that move in the outer part of the system. Consequently the cluster, over time, tends to develop a compact hot core and a cold expanded halo as shown in the right panel. The panel also indicate that the core will shrink since its temperature, higher than the temperature of the halo, continue increasing.

2.1.3 The effect of stellar evolution

It is well established in the literature that stellar evolution mass loss has a strong impact on the global properties of star clusters in their early-stage (Chernoff & Weinberg, 1990; Fukushige & Heggie, 1995). As a consequence of mass loss due to supernovae explosion and stellar winds, star clusters are affected by a strong monotonic inflation in the first ~ 10 Myr. In other words, stellar evolution mass loss triggers a strong expansion on early cluster evolution. After this stage, the picture is dominated by dynamic interactions: the overall cluster structure is affected by the two-body long and middle range interactions while the inner part of the system (the core) is mainly influenced by close interactions that involve hard binaries.

2.1.4 The effect of two-body interactions

When stellar evolution can be neglected the only component that governs the evolution of a star cluster is gravity. In this scenario, the trajectory of a single particle is painted by the gravitational potential of the whole system. While moving along this trajectory the particle is weekly perturbed by two-body close encounters (see the left plot of Fig. 2.1 for an illustration).

Typically, after few crossing time, the particles still move along their original orbit. However, after an interval of time called **two-body relaxation time** $t_{\rm rel}$ the particles forget its original trajectory because of the overall effect of many two-body close interactions. The $t_{\rm rel}$ can be estimated using the following equation Spitzer (1987):

$$t_{\rm rel} = \frac{0.138 N^{1/2}}{\ln \Lambda} \left(\frac{R^3}{G \bar{m}} \right)^{1/2} . \tag{2.1}$$

Here N is the number of stars in the cluster, R is the size of the cluster, $\bar{m}$ is the average star mass of the cluster and the argument of the Coulomb logarithm is $\Lambda = \gamma N$. Numerical experiments indicates a value for the parameter $\gamma = 0.11$ for single-mass systems and $\gamma = 0.02$ for multi-mass stellar systems Giersz & Heggie (1994, 1996). The shorter $t_{\rm rel}$ is, the stronger the effect of two-body interactions contribution is. Eq. 2.1 shows that $t_{\rm rel} \propto R^{3/2}$ when keeping N and $\bar{m}$ constant. This is because systems with large R are less compact and particles are on average further away from each other therefore two-body interaction is statistically less significant. On the other hand, when R and $\bar{m}$ are constant $t_{\rm rel} \propto \frac{N^{1/2}}{\log(N)}$, in other words the larger the number of particle is the longer it takes for the cluster to relax. This result might appear at first glance counter intuitive because a large number of particles in the same space implies more and stronger two-body encounters. However, when increasing the total particles number, also the total mass of the system increases $M \propto N \times \bar{m}$. Therefore the potential created by the whole system has more influence on the motion of every single particle: it takes longer for pairwise interactions to significantly influence trajectories.

As a consequence of two-body interactions, some particles decreases their kinetic energy while others increase it (see the sketch in the left panel of Fig. 2.1). The former sink into the inner part of the cluster stabilizing in a orbit closer to the core; instead the latter move in a wider orbit away from the center. While sinking towards the core particles convert potential energy into kinetic energy they, therefore, tend to increase their average velocity. The opposite is true for particles that move away from the center: they transform kinetic energy into potential energy and therefore decrease their average velocity. In summary, the overall effect of cumulative pare-wise gravitational interactions is to form a dense compact hot (high dispersion velocity) core surrounded by an extended lose cold halo. For example, let us consider a 10k cluster of 1 $M_\odot$ stars initialized according to a Plummer density profile with a 1 pc half mass radius. The relaxation time of this system $t_{\rm rel} \approx 30$ Myr. Consequently, after about 30 Myr the cluster develops an extended halo around a dense core. Due to its high density the dispersion velocity of the core σ_c is higher then the dispersion velocity of the halo σ_H; consequently $T_c \sim \frac{1}{2} \bar{m} \sigma_c >> T_H \sim \frac{1}{2} \bar{m} \sigma_H$. This allows use a simple thermodynamic model to predict qualitatively the future evolution of the cluster. The key idea is to divide the cluster into two separated thermodynamic systems: a hot core and a cold halo. Since the temperature of the core T_c is larger than the temperature of the halo T_H the energy flows from the core to the halo. Stars in the center keep losing kinetic energy in favor of the one located in the halo, the core keeps shrinking and increase its density while the halo expands (as sketched in the right panel of Fig. 2.1). Therefore, the temperature difference between the core and the halo becomes even more extreme. According to this simplistic thermodynamical description, the collapse of the core cannot be halted. this fact is also known as gravothermal catastrophe (Nakada, 1978; Lynden-Bell & Eggleton, 1980).

2.1.5 The effect of hard binaries

The thermodynamical description we just presented provides a too simplistic model of the evolution of a star cluster. In reality, core-collapse, leading to dramatic growth in the central density, triggers violent three-body close interactions. Three-body chaotic encounters can lead to the formation of **hard binaries**. The latter, once formed, prevent the core to collapse further. This is because during a single star-hard binary interaction the binary tends to increase the kinetic energy of the single star at the expense of their internal energy. In other words, utilizing triple chaotic encounters binaries release energy in the core and balance the loss of energy from the center halting the core to keep collapse collapsing (see Heggie & Hut, 2003, and references therein).

In an isolated equal-mass system, this happens on the order of $15t_{\rm rel}$ Cohn (1980). In real systems, the time scales can be shorter. In fact, real star clusters are born with a large fraction of primordial binaries that will start releasing energy into the system at moderately high density. The actual time scale needed to stop the core-collapse depends on the fraction of primordial binaries as well as their initial properties (such as mass ratio and semi-major axis).

In addition, observed star clusters have a broad mass spectrum, low mass stars tend to gain kinetic energy when interacting with massive stars; the former tend to expand their orbits, while the latter tend to lose kinetic energy and quickly segregate to the central part of the cluster. In this case, core collapse is driven by the amassing of heavy stars in the core that typically occur in a time scale of the order of the segregation time Spitzer & Hart (1971); Portegies Zwart et al. (2004)

$$t_{\rm s} = \frac{\bar{m}}{M_{\rm max}} \frac{0.138N}{\ln\left(0.11M/M_{\rm max}\right)} \left(\frac{R_{\rm h}^3}{GM}\right)^{1/2} \tag{2.2}$$

where $M_{\rm max}$ is the mass of the most massive object in the cluster and M is the total mass of the cluster. Consequently multi-mass clusters undergo core collapse in much shorter time then single-mass systems.

We conclude this section by emphasizing the fact that hard binaries play a key role in the evolution of star clusters. Any numerical method used to evolve star clusters must be able to model hard binaries and interactions involving hard binaries with high accuracy. This can be very challenging and require special regularization techniques that we explore in detail in the next part of the chapter.

2.2 Building a direct N-body code to evolve star clusters

In this section, we describe the main components needed to realize an accurate and computationally efficient direct N-body integrator for star clusters. Any algorithm designed to follow the gravitational evolution of a massive and compact stellar environment faces three main challenges. First of all the computational cost: for the direct summation method the computational time scales with $\sim N^2$ (where N is the number of a particle of the system) the integration can become rapidly very computationally expensive with increasing N. Simulating clusters with $N > 10^5$ require advanced numerical methods in combination with efficient palatalization schemes that can exploit the computational power of multiple graphics processing units (GPUs). Secondly, the interaction time scales in star clusters range from the order of few hours such as the orbital periods of compact objects in hard binaries up to several kiloyears for isolated stars located in the outer part of the system, which orbits are little affected two-body interactions. This drastic difference in time scale can be challenging to integrate efficiently. Star cluster numerical integrators must be able to follow organically and efficiently, interactions over a huge range of time scales. The third problem is related to the singularity of the Newtonian force. It happens frequently that particles in a compact cluster experience very close interactions, form hard binaries, or even undergo physical collisions. Hence the separation of the interacting objects reach very small values leading to round-off errors that in turn generate wrong values of the Newtonian force. In these situations, standard integration methods fail to give an acceptable approximation of the trajectories. It is, therefore, necessary to apply regularization methods that remove analytically or algorithmically the Newtonian singularity. In the following, we will discuss some of the most common numerical techniques employed by direct N-body codes to address the problems we just listed.

2.2.1 The Hermite Scheme

In order to build a direct N-body code we need first of all to have an accurate and fast way to update positions and velocities making sure to include the effect of every gravitational interaction. A very common way to compute these updates is by means of a Taylor expansion. Since the phase-space coordinates $(r_i(t), v_i(t))$ of a particle i, are smooth functions of the time, their evolution for an interval of time $\Delta t = t - t_0 < 1$ can be approximated to arbitrary precision through the expansion:

$$\begin{cases} r_i(t) = \sum_{k=0}^{\infty} \frac{r_i^{(k)}(t)|_{t_0}}{k!} \Delta t^k \\ v_i(t) = \sum_{k=0}^{\infty} \frac{v_i^{(k)}(t)|_{t_0}}{k!} \Delta t^k . \end{cases} \tag{2.3}$$

In case all the interactions are Newtonian, it is very simple to find an approximation up to the second order. In fact the second derivative of the position, the acceleration, is given by:

$$r_i^{(2)} = v_i^{(1)} = a_i = -\sum_{j \neq i} \frac{G m_j (r_i - r_j)}{|r_i - r_j|^3}. \tag{2.4}$$

Where the index j run over all the particles of the system excluding i. Computing directly the first derivative of the acceleration is also relatively straightforward to evaluate:

$$r_i^{(3)} = v_i^{(2)} = a_i^{(1)} = -\sum_{j \neq i} Gm_j \left[\frac{(v_i - v_j)}{|r_i - r_j|^3} + 3\frac{(r_i - r_j)[(r_i - r_j) \cdot (v_i - v_j)]}{|r_i - r_j|^5} \right] \tag{2.5}$$

It follows a simple but straightforward way to update the trajectory (r, v) of a particle i for an interval of time $\Delta t = t - t_0$:

$$\begin{cases} r_i(t) = r_i(t_0) + v_i(t_0)\Delta t + \frac{1}{2}a_i(t_0)\Delta t^2 + \frac{1}{6}a_i^{(1)}(t_0)\Delta t^3 \\ v_i(t) = v_i(t_0) + a_i(t_0)\Delta t + \frac{1}{2}a_i^{(1)}(t_0)\Delta t^2 \end{cases} \tag{2.6}$$

where $a_i(t_0)$ and $a_i^{(1)}(t_0)$ are respectively the acceleration and the jerk experienced by the particle i at t_0. Practically speaking the equations 2.6 can predict positions and velocities with satisfactory small errors only for very small values of Δt, making the integration computationally inefficient. A natural way to improve eq. 2.6 is to expand the Taylor series to a higher order. Several numerical experiments indicate that only $\geq 4^{\text{th}}$ order approximations lead to an integrator that is, at the same time, accurate and efficient (Aarseth, 2003). To obtain a fourth-order integrator we need to compute the second and the third derivative of the acceleration $a_i^{(2)}, a_i^{(3)}$. However, derivatives of the acceleration higher than the first turn out to be quite cumbersome to evaluate. We need to find a way to estimate $a_i^{(2)}$ and $a_i^{(3)}$. Once again we can Taylor expand to approximate their values as follows:

$$\begin{cases} a_i(t) = a_i(t_0) + a_i^{(1)}(t_0)\Delta t + \frac{1}{2}a_i^{(2)}(t_0)\Delta t^2 + \frac{1}{6}a_i^{(3)}(t_0)\Delta t^3 + O(t^4) \\ a_i^{(1)}(t) = a_i^{(1)}(t_0) + a_i^{(2)}(t_0)\Delta t + \frac{1}{2}a_i^{(3)}(t_0)\Delta t^2 + O(t^4) \end{cases} \tag{2.7}$$

Solving the system of equations in 2.7 for $a_i^{(2)}(t_0)$ and $a_i^{(3)}(t_0)$ we obtain:

$$\begin{aligned} a_i^{(2)}(t_0) &\approx -6\frac{a_i(t_0) - a_i(t)}{(t - t_0)^2} - 2\frac{2a_i^{(1)}(t_0) + a_i^{(1)}(t)}{(t - t_0)} \\ a_i^{(3)}(t_0) &\approx 12\frac{a_i(t_0) - a_i(t)}{(t - t_0)^3} + 6\frac{a_i^{(1)}(t_0) + a_i^{(1)}(t)}{(t - t_0)^2} \end{aligned} \tag{2.8}$$

therefore to estimate $a_i^{(2)}(t_0)$ and $a_i^{(3)}(t_0)$ we would need to know a_i and $a_i^{(1)}$ at the instant t. However, to compute $a_i(t), a_i^{(1)}(t)$ we must know $r_i(t)$ and $v_i(t)$, which are the unknown quantities that we would like to estimate. The trick to proceed is to first compute the approximated values of the positions $\widetilde{r}_i(t)$ and velocities $\widetilde{v}_i(t)$ at instant t using equation 2.6. Then use the approximations $\widetilde{r}_i(t)$ and $\widetilde{v}_i(t)$ to estimate $a_i(t), a_i^{(1)}(t)$ that in turn are used to evaluate $a_i^{(2)}(t_0)$ and $a_i^{(3)}(t_0)$ by means of equation 2.8; arriving, in this way, to the desired result. The scheme just described is called the Hermite scheme and it is employed by NBODY6++GPU to compute middle and long range interactions. Here we give a schematic summary on how this algorithm evolves a particle i from t_0 to t :

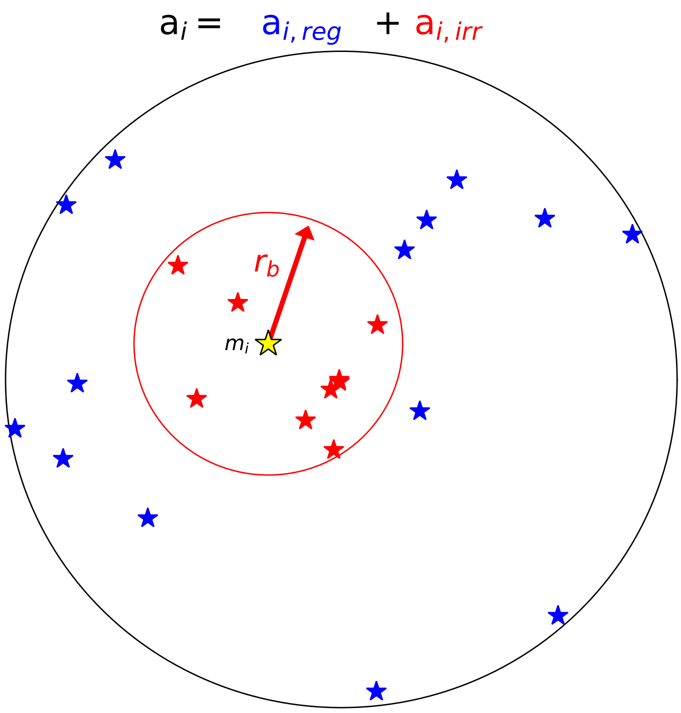

Figure 2.2: Sketch of the neighbourhood radius r_b and the neighbourhood sphere. The force between the yellow and the close particles (red) can change significantly after a small interval of time Δt in both absolute value and direction. On the other hand, the change in the force between the distant (blue) and the yellow particles is negligible.

1. Estimate position $\widetilde{r_i}$ and velocities $\widetilde{v_i}$ at instant t using equation 2.6
2. Use the values $\widetilde{r_i}$ and velocities $\widetilde{v_i}$ to find the approximate value of acceleration a_i and jerk $a_i^{(1)}$ at time t.
3. Compute a_i and jerk $a_i^{(1)}$ at time t_0.
4. Plug the just calculated values of $a_i(t_0), a_i(t), a_i^{(1)}(t_0), a_i^{(1)}(t)$ inside equation 2.8 to find $a_i^{(2)}(t_0)$ and $a_i^{(3)}(t_0)$
5. Find a more accurate values of position $r_i(t)$ and velocities $v_i(t)$ using a 4$^{\text{th}}$ order Taylor expansion.

The Hermite scheme belongs to the class of predictor-corrector algorithms. These type of algorithms, they employ two steps to find the solution of ordinary differential equations. Firstly they "predict" the approximated solution value to a subsequent new point, next they "correct" the initial approximation by using the initially predicted value.

2.2.2 Block Time Steps

As we mentioned before star cluster time scales span over several orders of magnitudes. The time step Δt introduced in the previous section changes its value from particle to particle. If the particle i experiences a strong interaction or is a component of a hard binary Δt_i can be of the order of days or even hours. On the other hand, if i is an isolated particle located in the outer region of the cluster, it does not need to update pistons and velocity with such a high frequency; to economize the calculation, i is allowed to move for a much larger distance and can have an associated time step Δt_i that might be of the order of $\sim 10 - 100$ kiloyears.

A standard way to evaluate the time step Δt_i is computing the minimum between the free - fall time step $\Delta t_{\mathrm{ff},i}$ and the fly-by time-step $\Delta t_{\mathrm{fb},i}$ that are defined as follow:

$$\Delta t_{\mathrm{ff},i} \propto \min_{j \neq i} \left(\frac{|r_i - r_j|^3}{G(m_i + m_j)} \right)^{1/2} \qquad \Delta t_{\mathrm{fb},i} \propto \min_{j \neq i} \frac{|r_i - r_j|}{|v_i - v_j|} \tag{2.9}$$

However, many numerical experiments suggest that the most robust way to estimate Δt_i is Aarseth's time step criteria (for this reason adopted in NBODY6++GPU):

$$\Delta t_i \propto \sqrt{\frac{|a_i||a_i^{(2)}| + |a_i^{(1)}|^2}{|a_i^{(1)}||a_i^{(3)}| + |a_i^{(2)}|^2}} \tag{2.10}$$

Although each particle has its individual time step Δt_i we cannot evolve every particle individually. This would be extremely computationally inefficient. It is much more convenient to group particles in different timestep blocks and update the trajectory of all the particles of a specific block at the same time. For instance, NBODY6++GPU associates the same time step to all the particles that have a similar value of Δt_i. Specifically, all the particles with time step in between $2^{n-1}\Delta t_{\mathrm{min}} < \Delta t_i < 2^n \Delta t_{\mathrm{min}}$[2] are grouped in the same block and their coordinates are updated in synchrony with the same time step $2^n \Delta t_{\mathrm{min}}$. Hence, particles in the block $m > n$ are updated less frequently.

To evolve particles that have short time steps, the integrator needs to use also the positions and velocities of particles with longer time steps. In other words, to update the coordinates of the particles in the group n at the instant $t_0 + 2^n \Delta t_{\mathrm{min}}$, the integrator needs to find the positions and velocities of the particles in the block m at the same instant of time. Since the coordinates of the particles in m are not updated at $t_0 + 2^n \Delta t_{\mathrm{min}}$, the algorithm extrapolates them using a Taylor expansion.

The procedure that we have just illustrated breaks Newton's third law: at the instant $t_0 + 2^n \Delta t_{\mathrm{min}}$ particles in the block n experience the force generated by the particles in m but the opposite is not true. As a consequence of that, linear and angular momentum are not conserved. Although this might be problematic for the integration of certain systems, in general, it might not have significant effects since the relative amount of non-conserved momentum is negligible. We will see in the next sections how this problem can be solved by adopting an appropriate Hamiltonian splitting scheme (see appendix C for a brief introduction on the Hamiltonian splitting scheme).

[2] Here $n \geq 0$ is an integer, while Δt_{min} is the minimum time step and is chosen small enough to allow the code to include every interactions in realistic systems.

2.2.3 The Ahmad–Cohen scheme

The most computationally expensive part of a direct N-body algorithm is the calculation of the force. Computing the force on a single particle requires $N - 1$ steps. Since this procedure must be repeated for all the particles of the system, overall, the force evaluation needs $\sim N^2$ steps. To evaluate the force efficiently maintaining high accuracy NBODY6++GPU adopts the Ahmad–Cohen "neighbor scheme". In brief, the Ahmad–Cohen scheme economizes the force calculation by separating the contribution of near and distant particles and making frequent updates only taking into account the contribution of neighboring particles. To describe this scheme in more details we start with the consideration that the acceleration of a given star $a_{i,\mathrm{reg}}$ can be split in a regular and a irregular component:

$$a_i = a_{i,\mathrm{reg}} + a_{i,\mathrm{irr}} \tag{2.11}$$

$a_{i,\mathrm{reg}}$ represents the contribution to the total acceleration that come from interactions with distant particles. This quantity varies slowly in time, because, for small-time steps, the positions of remote particles do not vary much with respect to the particle i providing a quasi-static smooth potential. On the other, hand $a_{i,\mathrm{irr}}$ is the acceleration experienced by i generated by its N_b neighbourhoods. This quantity is likely to change rapidly over time (see particles blue in the left panel of Fig. 2.2), with stronger fluctuations, so it must be determined more frequently than its regular counterpart. More quantitatively, if we compute the time step using equation 2.10 separately for the regular and irregular component, we obtain $\Delta t_{\mathrm{irr}} << \Delta t_{\mathrm{reg}}$. It is therefore unnecessary to update the full acceleration at each time step, it is enough to include all the particles contribution every Δt_{reg}, while updating more frequently the local contributions.

This is what the Ahmad–Cohen scheme does concretely: For each particle i it finds a list of N_b neighborhoods that lay within a specified sphere with radius r_b (the neighborhood radius) as illustrated in Fig. 2.2. All the particles, close to the sphere that are moving towards the sphere ($v \cdot r < 0$) are also included in the neighborhood list. At each irregular time step $a_{i,\mathrm{irr}}$ is computed directly from the neighbourhood list while $a_{i,\mathrm{reg}}$ is extrapolated by means of a Taylor series. The full force calculation is therefore computed only every Δt_{reg}. Both the neighborhood list and the neighbor radius r_b are updated at each regular time step using the latest coordinates.

2.2.4 A recursive Hamiltonian splitting scheme alternative to the block time step method

The block time-step scheme we discussed early is a simple and effective way to deal with the large range of timescales that characterize star cluster dynamics. Coupled with this scheme, numerical integrators can evolve simulations more efficiently by focusing the computational resources on the parts of the system that undergoes the most energetic interactions. However, as we already mentioned, this method violates Newton's third law and therefore does not conserve linear and angular momentum.

The algorithm proposed by (Pelupessy et al., 2012) retains the desirable properties of the block time-step scheme, but at the same time conserves the integrals of motion. This algorithm operates in such a way that the interactions between particles are computed pairwise thus ensuring the Newton third law is respected. Moreover, the method, if used with fixed values of the time - step, is symplectic, or in other words, preserve phase-space volumes.

In general, it is beneficial to construct, whenever possible, a numerical integrator that is symplectic. Algorithms with this property manifest good energy conservation and are reliable on long-time integration (see appendix B for more details). One way to building symplectic integrators is by means of an Hamiltonian splitting scheme. The latter consist on splitting the Hamiltonian of a system into two simpler and solvable subsystems ($H = H_A + H_B$). The split might be based on energy and momentum, but more generic type of division can be employed (see Wisdom & Holman, 1991, as an example). Thanks to the split, the time evolution operator $\exp dtH$ (see appendix A) can therefore be approximated with a second order symplectic integrator as follow:

$$\exp(dtH) \approx \exp(\frac{dt}{2}H_A) \cdot \exp(dtH_B) \cdot \exp(\frac{dt}{2}H_A) \tag{2.12}$$

Here, the Hamiltonians that appear in the equation are to be understood as operators. For a broader discussion on the Hamiltonian Splitting, scheme sees appendix C.

Pelupessy's algorithm employs a special recursive Hamiltonian splitting method, which division is based on the time-step of each individual particle. In brief, the algorithm works as follows: first of all, for each particle is associated an individual time-step Δt_i using the equation 2.10 or similar. Then the system is split into fast $\Delta t_i < \tau$ and slow $\Delta t_i > \tau$ moving subsystem. Here τ is an initial pivot time step whose value is arbitrarily initialized at the start of the integration. The corresponding split in the Hamiltonian is:

$$H = H_S + H_F \tag{2.13}$$

Where H_S, H_F are the Hamiltonian of the subsystems containing slow and fast particles respectively. The procedure is then repeated for H_F, using a pivot τ half the value of the previous one, until there are no fast particles left.

There are several possible ways to define the fast and the slow Hamiltonian. For instance, the term of the potential that represents interactions between slow and fast particles here indicated with the symbol V_{SF} could be arbitrarily distributed in both Hamiltonians. However, numerical experiments indicate the following to be the most efficient splitting scheme (see Pelupessy et al., 2012, for more details):

$$\begin{aligned} H_S &= P_S + V_{SS} + V_{SF} \\ H_F &= P_F + V_{FF} \end{aligned} \tag{2.14}$$

where P_S and P_F are the fast and slow kinetic energy; V_{SS} is the potential containing all interactions between the slow particles, while V_{FF} includes all interactions between fast particles. Note that the potential cross terms V_{SF} was intentionally inserted in H_S. With this choice, the interaction between the particles in the slow and fast systems takes place in the slowest time-step. Hence the split can be expected to be computationally very efficient. Moreover this cross interactions are computed simultaneously. Consequently, this scheme, contrary to the block time step method, computes, for every $i \rightarrow j$ interaction, the corresponding $j \rightarrow i$ interaction at the same time. It follow that this method manifestly conserves the momentum (and the angular momentum).

2.2.5 Frost: a 4^{th} order forward symplectic integrator inserted in a fourth-order hierarchical Hamiltonian splitting scheme

When we presented the Hermite scheme (see Section 2.2.1) we explicitly stated that numerical experiments favour $\geq 4^{\text{th}}$ order integrators, because algorithms that utilize lower-order approximations require time steps ridiculously low to maintain a satisfactory accuracy. They are therefore not suitable to evolve large systems such as massive star clusters and globular clusters that have more than $N > 10^5$ number of particles. The method illustrated in Pelupessy et al. (2012), that we described in the previous section, despite being symplectic and being momentum conserving, is a 2^{nd} order integrator. It is therefore problematic to use such an integrator to follow the evolution of massive star clusters for a long integration time (~ 1 Gyr).

A very popular and also simple method to build symplectic integrators of arbitrary large even order is described in Yoshida (1991). Unfortunately, integrators beyond the second-order derived with this method lead to negative integration sub-steps. This causes problems when evolving time-irreversible dynamical processes such as tidal dissipation and gravitational radiation.

A way to avoid negative time steps in a 4^{th} order symplectic integrator is illustrated in Chin (1997); Chin & Chen (2005). These studies lead to the development of a family of forward symplectic integrators which, by means of evaluating the force gradient, require only positive integration sub-steps.

Exploiting these new class of integrators Rantala et al. (2021) managed to successfully extend the 2^{nd} recursive Hamiltonian splitting scheme described in Pelupessy et al. (2012) to a 4^{th} order integrator. In addition, to be symplectic and suitable to integrate systems with a huge dynamical range, this novel algorithm, thanks to an efficient MPI-CUDA parallelization to run on multiple GPUs assigned to different computing nodes, is capable to evolve direct summation N-body simulations beyond $N = 10^6$ particles.

It is important to mention that both Pelupessy's and Rantala's methods are symplectic as long as they use constant time-steps which cannot be efficiently applied to integrate star clusters of realistic sizes: individual adaptive time-steps are required to follow the evolution of systems with such a large amount of particles.

Losing the symplecticity (as well as time-reversibility) is an unavoidable consequence of the use of adaptive time-steps, which in turn causes a secular energy error growth in long-term simulations. It is however possible, utilizing a so-called time-step symmetrized procedure (see Pelupessy et al., 2012; Dehnen, 2017; Rantala et al., 2021, for more details), to partially restore the lost time-reversibility, and this can be very beneficial because reversible integration algorithms have many virtues similar to those of symplecticity integrators. First, of all, they help to decrease the energy error drift.

2.2.6 Regularization Methods

In the inner region of a compact star cluster, it is likely that stars get very close, experiencing close interactions or even physical collisions. This is also true for star clusters, not necessarily very dense, that have a large fraction of primordial hard binaries.

In general, handling the integration of primordial binaries, hyperbolic encounters and close energetic interactions can be very challenging for standard numerical methods even for 4^{th} or higher-order integrators. When the separation of two objects is very small the singularity in the gravitational potential leads to extremely high values for the acceleration and truncation errors start to become significant. Standard integrators, for example the 4^{th} order Hermite scheme, might be able to follow these types of interaction, with reasonably good accuracy, only reducing the time steps to prohibitively small values, making the computation excessively time-consuming. Moreover, an integrator such as the Hermite scheme when used to follow the evolution of hard binaries would be affected by energy drift that, in long integration time, would lead to completely wrong trajectories. To rephrase it, since standard non-symplectic integrators lead to unbound energy error[3], they are not suitable to evolve hard binaries. One might argue that a symplectic integrator might help in this regard because such an integrator guarantee the energy error to be bounded (see appendix B). However, even for a symplectic integrator, it is necessary to use extremely small time steps to reach high accuracy making the integration extremely inefficient. Assume for example to evolve a hard binary with high eccentricity. In order to preserve the symplecticity and to have a good approximation of the trajectory, the integrator must use a fixed time-step small enough to resolve the pericenter passage. The latter can be an order of magnitude smaller than the time-step in the proximity of the apocenter. As a consequence of that, the computation become immensely expensive for long-term evolution.

To solve the issues we just illustrated, the most advanced direct N-body codes for star cluster simulations combine their usual integrator for medium or long-range interaction with a regularisation method for short-range interactions. A regularization method is an elegant way to deal with Newtonian singularity and treat particles that are experiencing a strong interaction or are moving in a hard binary. The basic idea is to detach the close interacting subsystem (such as a hyperbolic encounter, a hard binary, a triple etc.) from the main integration cycle. Continue the standard integration replacing the subsystem with its centre of mass. Move to the centre of mass coordinates of the subsystem (to limit the growth of truncation errors) and resolve the internal dynamics with a special technique.

Here, in the next subsections, we described two of these "special techniques": The Logarithmic Hamiltonian (logH) and the Kustaanheimo-Stiefel regularization. The former has been adopted in FROST and NBODY7 (Aarseth, 2012), it time-transforms the Keplerian Hamiltonian into a new separable Hamiltonian, whose equations of motion can be easily and efficiently solved by any symplectic integrator. The latter, adopted in NBODY6++GPU, exploit a rotation in the quaternion space to reduce the Keplerian Hamiltonian into the Hamiltonian of a 4D harmonic oscillator. By doing so it removes analytically the Newtonian singularity.

Algorithmic regularization: the logarithmic Hamiltonian

A simple but effective trick to use a symplectic algorithm, for example the "drift-kick-drift" (DKD) leap-frog algorithm (see appendix D), to follow the dynamics of an eccentric binary (or hyperbolic encounters) without spoiling the symplecticity of the integrator, is to perform the

[3]The energy error increases inevitably over time.

integration with respect to a fictitious time variable s that is related to the real-time through the following equation also know as the Poincaré time transformation:

$$dt = g(q,p)ds \tag{2.15}$$

where $g(q,p)$ is the time step function that regulates the size of the real-time step $\Delta t = g(q,p)\Delta s$, and in general it might depend on the position q and momentum p of the particles. In doing so we can maintain the integration time step Δs constant (therefore we preserve the symplecticity) but at the same time, we can vary the physical time Δt step making the integration more efficient. For example, choosing $g(q,p) \propto |q|$ (where $|q|$ is the separation of the two body) leads to small-time steps near the pericenter and large time steps near the apocenter.

Since the real time variable t depends directly on s, $t(s)$ must also be included in the integration [4]. In other words t have been promoted to a coordinate. We theretofore need to perform a change of coordinates in the standard Keplerian Hamiltonian $H(q,p) = \frac{p^2}{2\mu} - \frac{M\mu}{q}$ and extend our phase space from $\{q,p\}$ to $\{Q,P\}$ defined as:

$$Q = (q_0, q); P = (p_0, p) \tag{2.16}$$

where $q_0 = t$ and p_0 is the momentum of time. The equation of motion in the extended phase space are:

$$\begin{cases} \frac{dt}{ds} &= g(q,p) \\ \frac{dq}{ds} &= \frac{dq}{dt}\frac{dt}{ds} = g(q,p)\frac{\partial H}{\partial p} \\ \frac{dp}{ds} &= \frac{dp}{dt}\frac{dt}{ds} = -g(q,p)\frac{\partial H}{\partial q} \\ \frac{dp_0}{ds} &= \frac{dp_0}{dt}\frac{dt}{ds} = g(q,p)\frac{dp_0}{dt} \end{cases} \tag{2.17}$$

Now for convenience we set $p_0 = -H$. Note that if the two interacting bodies are isolated the energy is conserved and p_0 the momentum of time is constant; this consideration is not true for a perturbed binary; in this case the effect of the external perturbations is taken into account calculating the change of p_0 over time. With our choice on the initial value of p_0 the Hamiltonian corresponding to the new equation of motion 2.17 takes the following form:

$$\Lambda(Q,P) = g(q,p)(H(q,p) + p_0). \tag{2.18}$$

It is easy to check that indeed the Hamiltonian in 2.18 lead to the equations 2.17. For a generic choice of $g(q,p)$ the new Hamiltonian $\Lambda(Q,P)$ is not separable and therefore a sympathetic integrator cannot be applied straightforwardly by means of the Hamiltonian splitting scheme we illustrated earlier. However, we can solve this problem employing a simple trick on the choice of $g(q,p)$. First of all the Hamitonian $H(q,p)$ can be rewritten as:

$$H(q,p) + p_0 = T + U + p0 = \lim_{X \to T + p_0}(X + U). \tag{2.19}$$

[4]If we integrate only $q(s)$ and $p(s)$, we know the position and the velocity of our system but we do not know when the system has that specific configuration, because we do not know the relation between t and s

Now let us assume the time step function g can be written as the derivative of a new function $f(X)$ computed at $X = -U$(in doing so we are implicitly assuming that g is only a function of the potential U):

$$g = \frac{\partial f(X)}{\partial X}|_{X=-U} = \lim_{X \to -U} \frac{f(X) - f(-U)}{X - (-U)} \tag{2.20}$$

since we choose $p_0 + U + T = 0$, then

$$g = \lim_{X \to p_0 + T} \frac{f(X) - f(-U)}{X - (-U)} \tag{2.21}$$

consequently the new Hamiltonian can be calculated as follow:

$$\Lambda = \lim_{X \to T + p_0} (X + U) \lim_{X \to -U} \frac{f(X) - f(-U)}{X - (-U)} \tag{2.22}$$

since the product of two limits is equal to the limit of the product, Λ can be written as:

$$\Lambda = g(q,p)(H(q,p) + p_0) = \lim_{X \to T + p_0} (X + U) \frac{f(X) - f(-U)}{X - (-U)} = f(T + p_0) - f(-U) \tag{2.23}$$

So with this smart mathematical trick we managed to rewrite the new Hamiltonian Λ in a separable form. Now we have to find a smart choice for $f(X)$. As we illustrated before, it is very natural to set $g \propto R$ because in this way we ensure Δt to decrease when the two objects are closer and increase when they are far away. The simplest assumption that follows this consideration is to choose $g(U) = -\frac{1}{U}$ that in turn leads $f(X) = \log(X)$ (see eq. 2.20). With this choice the new Hamiltonian become:

$$\Lambda(Q,P) = \log(T(P) + p_0) - \log(-U(Q)) \tag{2.24}$$

and starting from eq. 2.17 we derive the new equations of motions:

$$\begin{cases} \frac{dt}{ds} & = -\frac{1}{U} \\ \frac{dq}{ds} & = -\frac{1}{U}\frac{\partial H}{\partial p} = -\frac{1}{U}\frac{p}{\mu} \\ \frac{dp}{ds} & = \frac{1}{U}\frac{\partial H}{\partial q} \\ \frac{dp_0}{ds} & = \frac{1}{U}\frac{\partial U}{\partial t}. \end{cases} \tag{2.25}$$

We stress the fact that, for this new set of equations, the integration is done with respect to the variable s. So we can use any simplistic algorithm and guarantee that its properties are respected by maintaining the step of the integration Δs constant.

It turns out that choosing $g(U) = -\frac{1}{U}$ is very convenient because the integrator DKD leap-frog does follow the Keplerian trajectory exactly. This means that the position and velocity of the binary are precisely those of the real Keplerian orbit without introducing any error. This result is valid only for the DKD leapfrog, not for the "kick-drift-kick" leap-frog (see appendix of Preto & Tremaine, 1999, for the proof). The only uncertainty appears in the integrated time $t(s)$. We can determine exactly the phase-space trajectory of the two particles but we cannot know precisely the time of arrival at a given location in the phase-space. In other words, using this numerical technique the only error we introduce is a phase shift in the integrated binary.

Kustaanheimo-Stiefel Transformation

The Kustaanheimo-Stiefel (KS) transformation (Kustaanheimo & Stiefel, 1965) is a coordinate and time transformation in the phase-space that turns the Kepler problem into a harmonic oscillator.

The transformation start by applying once again the Poincare time transform $dt = |q|ds$ (choosing $g(q,p) = |q| \propto -1/U$) to obtain the Hamiltonian given in eq. 2.18 that for the Keplerian problem take the form:

$$\Lambda = |q| \left(\frac{|p|^2}{2\mu} - \frac{M\mu}{|q|} + p_0 \right) \tag{2.26}$$

Now to change Λ into an harmonic oscillator we need to find a new set of coordinates $\{Q, P\}$ that respect the qualities:

$$|q| = |Q|^2; \qquad |p| = |P|/(2|Q|) \tag{2.27}$$

in fact, substituting the equations given in 2.27 in the Hamiltonian 2.26 we get:

$$\Lambda = |Q|^2 \left(\frac{P^2}{8|Q|^2\mu} - \frac{M\mu}{|Q|^2} \right) = \frac{P^2}{8\mu} - M\mu + Q^2 p_0 \tag{2.28}$$

which is the Hamiltonian of an harmonic oscillator shifted from the origin. Thus the collision singularity has been removed. The actual transformation that connect the old with the new coordinates can be formally represented in a matrix form:

$$\begin{aligned} q &= M(Q)Q \\ p &= M(Q)P/(2|Q|^2) \end{aligned} \tag{2.29}$$

the only requirement to fulfil eq. 2.27 is that $M(Q)M^\intercal(Q) = I|Q|^2$ (where I is the identity matrix). In other words, the inverse matrix $M^{-1}(Q)$ does exist and it is proportional to its transpose ($M^{-1}(Q) \propto M^\intercal(Q)$): in other words $M(Q)$ must be orthogonal.

The fact that $M(Q)$ is invertible is essential for practical applications. In fact, we need to be able to map $\{q, p\}$ into $\{Q, P\}$ at the beginning to then transform back to the original coordinates at the end of the integration.

Now we are left with the task of finding in concrete the components of $M(Q)$. In 1D this would be very trivial: in this case $M(Q)$ is a scalar equal to $M(Q) = |Q|^2 = Q^2$.

The 2D case is less trivial. To find the explicit form of the transformation in two dimension it is convenient to represents the vectors $Q = (Q_1, Q_2)$ and $q = (q_1, q_2)$ as complex numbers: $q = q_1 + iq_2$ and $Q = Q_1 + iQ_2$. In fact, every vector in the 2D space can be represented by complex numbers. In our case this case $q = q_1 + iq_2$ and $Q = Q_1 + iQ_2$. To ensure that $|q| = |Q|^2$ we impose that[5]:

$$(Q_1 + iQ_2)^2 = q_1 + iq_2 \tag{2.30}$$

[5]since $q = q_1 + iq_2 = |q|e^{i\phi}$ and $Q = Q_1 + iQ_2 = |Q|e^{i\theta}$, the equality $(Q_1 + iQ_2)^2 = q_1 + iq_2$ implies $= |Q|^2 e^{i2\theta} = |q|e^{i\phi}$ that in turn leads to $|Q|^2 = |q|$

This in turn leads to the relations $q_1 = Q_1^2 - Q_2^2$ and $q_2 = 2Q_1Q_2$ that in turn conduce to:

$$M(Q) = \begin{bmatrix} Q_1 & -Q_2 \\ Q_2 & Q_1 \end{bmatrix} \tag{2.31}$$

The matrix just found is the Levi-Civita matrix in two dimensions. This matrix, in addition to being orthogonal, has the property of having all elements linear and homogeneous functions of the Q components.

Finding the Levi-Civita matrix in higher dimensions is essential to regularize the Keplerian Hamiltonian in 3D. Unfortunately, a matrix with such properties cannot be constructed in 3 dimensions. Nevertheless, it can be constructed in 4D. A very elegant approach to derive the elements of the 4D Levi-Civita matrix transformation employs the use of quaternions Heggie & Hut (2003); Saha (2009). This derivation leads to the matrix:

$$M(Q) = \begin{bmatrix} Q_1 & -Q_2 & -Q_3 & Q_4 \\ Q_2 & Q_1 & -Q_4 & -Q_3 \\ Q_3 & Q_4 & Q_1 & Q_2 \\ Q_4 & -Q_3 & Q_2 & -Q_1 \end{bmatrix} \tag{2.32}$$

In order to find a univocal relation between the physical coordinated q_1, q_2, q_3 and Q, one of the components of Q must be fixed. To guarantee that the KS transformation is numerically well defined for solving the 3D Keplerian equation of motion it is convenient to impose that (Aarseth, 2003, see):

$$Q = \begin{cases} (Q_1, Q_2, Q_3, 0), \text{for} & q_1 \leq 0 \\ (Q_1, Q_2, 0, Q_3), \text{for} & q_1 > 0 \end{cases} \tag{2.33}$$

This choice for Q lead to the following relation:

$$\begin{aligned} q_1 &= Q_1^2 - Q_2^2 - Q_3^2 \\ q_2 &= 2Q_1Q_2 \\ q_3 &= 2Q_1Q_3 \end{aligned}$$

instead the relation to obtain the components of Q from the physical equations are:

$$\begin{aligned} Q_1 &= \sqrt{\frac{1}{2}(|q| + |q_1|)} \\ Q_2 &= \frac{1}{2} q_2 / Q_1 \\ Q_3 &= \frac{1}{2} q_3 / Q_1 \end{aligned}$$

The equations of motion derived from the regularised Hamiltonian (eq. 2.27) are:

$$\begin{aligned} \frac{d^2Q}{ds^2} &= -\frac{p_0}{2\mu} Q \\ \frac{dt}{ds} &= Q^2 = |q| \end{aligned}$$

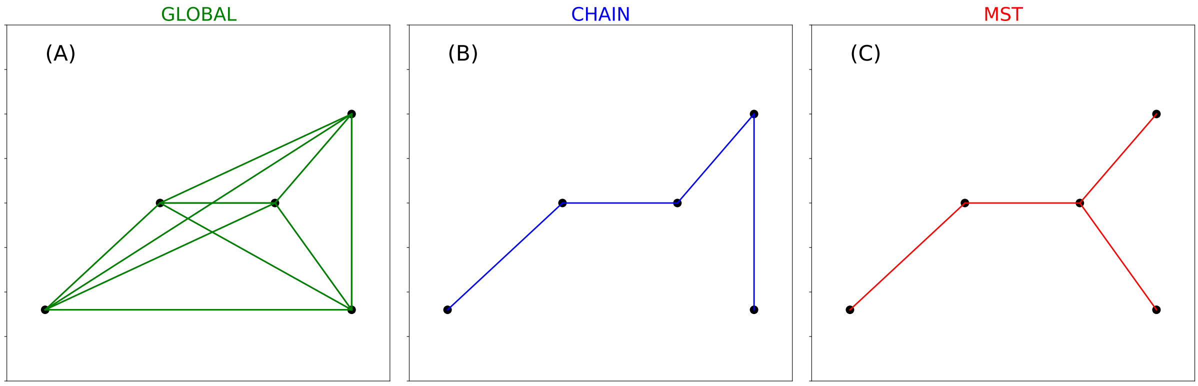

Figure 2.3: The figure illustrates schematically the regularized interactions in global method of Heggie (left panel), in the chain method (central panel) and in the minimum spanning tree algorithm (right panel).

as long as the binary is isolated ($p_0 = -H$ is constant). In the case of a perturbed binary the equations becomes

$$\frac{d^2Q}{ds^2} = -\frac{p_0}{2\mu}Q + \frac{1}{2}Q^2M^\intercal(Q)F$$
$$\frac{dp_0}{ds} = 2\mu\frac{dQ}{ds}M^\intercal(Q)F$$
$$\frac{dt}{ds} = Q^2 = |q|$$

Where F is the external force that perturbs the motion of the two particles. Since the equations are regular, any symplectic integrator can provide accurate, efficient, and stable numerical solutions.

Regularization Methods for $N \geq 3$

So far we showed how to use the regularization methods (KS, logH) to solve the two-body gravitational problem. In this section we briefly summarize some of the most common ways to extend these methods for close interactions that involve $N \geq 3$ particles.

Probably the first approach ever developed is Heggie's global regularization (Heggie, 1974). In this approach every single pairs of particle is regularized, as sketch in panel A of Fig. 2.3. In practice, this technique can become cumbersome and computationally expensive for large N.

A more effective approach is the chain regularization method (Mikkola & Aarseth, 1993) that provides is a simpler solution to the problem with almost identical integration accuracy. This method does not regularize all the pairs of the system, it regularizes only some of them. To select the pairs that must be regularized it first finds and links the two particles with the shortest distance, which become head and tail of the chain. The next tail (head) is the non-chained particle closest to the current tail (head). The procedure is repeated until all particles are chained (see panel B of Fig. 2.3 for an illustration).

In Rantala et al. (2020) instead of using the chain method, they adopted the minimum spanning tree (MST) algorithm to find the pairs of particles to regularize. This new approach is, in many cases, more accurate then the standard chain structure because it successfully links each particle to its closest neighborhood thus ensuring that interactions with less separation are regularised (see comparison between panel B and C of Fig. 2.3).

2.3 Stellar evolution

Real astrophysical star clusters are composed of stars, which, affected by their internal evolution tend to change their properties (such their mass, their radii, etc) in time. Unavoidably, stars, evolving over time, affect the gravitational evolution of the cluster where they are located. For instance, mass loss due to stellar winds and supernovae explosions play an important role in the early stage of the cluster causing a rapid expansion of the system. Moreover, the details of the physics that govern the last moments before stellar collapse have a significant impact on determining the mass distribution of compact objects such as BHs and NSs which in turn are extremely relevant to correctly interpret and predict GW detections.

Therefore, to make a consistent comparison with observations, N-body simulations of star clusters need to incorporate many effects of stellar evolution. to put it another way, N-body codes require prescriptions to follow the change in time of the properties of the stars contained within the cluster. The stellar models suitable for gravitational integrators must be able to describe all the relevant stages of a star. They should be able to estimate, with reasonable accuracy, the main property of a star, over the course of its entire life, starting from the main sequence phase to the remnant stage. At the same time, they must be computationally inexpensive: they should provide the required information without significantly affecting the computational time of the simulation.

NBODY6++GPU follows the evolution of individual stars using a set of fitting function included in the SSE package Hurley et al. (2000). This set of routines, dividing the life of a star into 15 stages[6], are able to track mass, core mass, radius, core radius, and luminosity of a star, with initial mass in the range between 0.08 up to 100 $M_\odot$, for its entire lifetime. By employing fitting functions, calibrated using observations, they are able to estimate these rapidly and efficiently. As we illustrated earlier binaries play a major role in the dynamical evolution of star clusters. As such, N-body models have been equipped with special regularization techniques with the porpoise of following their dynamical evolution. Equally important, are the effects of stellar evolution in binaries. They can lead to very interesting events such as mass transfer, common envelope evolution, and collisions which in turn generate important observational phenomena and exotic objects such as X-ray binaries, gamma-ray bursts, and blue stragglers.

Including binary stellar evolution in an N-body code presents several challenges because the dynamical and stellar evolution often influences one another. The parts of the code, respectively

[6]The stages are enumerated from 0 to 14. They include main sequence (0, 1, 7), Hertzsprung gap (2, 8), red giant (3, 4, 5, 6, 9) and remnant stage (10, 11, 12, 13, 14).

used model respectively gravity and stars, therefore, need to smoothly exchange reciprocal information. For instance, if a binary undergoes an event of mass transfer, the change in mass of the two components must be communicated to the dynamical integrator with minimal delay to ensure an accurate evaluation of the gravitational force. Conversely, the dynamical interface of the code must communicate on time whether the orbital parameters of a binary have been modified by external perturbations so that the stellar evolution can evaluate the consequences for the binary evolution outcomes.

To model binary stellar evolution NBODY6++GPU uses the package BSE that is a composed by a set of analytical formula to follow the main properties of single stars (such as radius, mass, luminosity, and core mass) from the zero-age main-sequence to the remnant stage. For tight enough binary, BSE includes prescriptions for mass transfer, Roche phase, and common envelope evolution. The first two studies presented in this thesis (see Chap. 3 and 4) have been realized using NBODY6++GPU coupled with an updated version of the standard BSE.

2.3.1 The evolution of massive stars

The results of the first two projects presented in this thesis depend strongly on the treatments adopted to evolve stars heavier than 25 $M_\odot$. At the end of their life, such stars are expected to collapse into BHs, whose mass heavily depends on the stellar winds models adopted. In the original BSE, the stellar winds mass-loss rate are based on analytical formulae little affected by metallicity. Such early formulae ignored the possibility for a photon to experience multiple scattering before being absorbed or escape the photosphere. The work by Vink et al. (2001) had already accounted for multiple scattering and found massive stars stellar winds to be strongly dependent on metallicity, but these relations were not commonly adopted because, at the time, there was no strong evidence that they were necessary. The situation was reversed thanks to the LIGO/Virgo/Kagra detections, which pointed out the existence of many BHs with masses $\gtrsim 30$ $M_\odot$. Prescriptions on stellar winds dependent on metallicity raised in popularity, since adopting such recipes, at low metallicity, massive stars can easily form BHs with masses $\gtrsim 30$ $M_\odot$. On the other hand, utilizing the standard treatments, the maximum BH mass conceivable is slightly below 30 $M_\odot$.

At the beginning of the core-collapse, stars with massive helium cores ($\sim 30-130$ $M_\odot$) can trigger efficient electron-positron production which in turn leads to a radiation-pressure drop. Consequently, the inner part of the star contracts and, reaching higher densities, ignites the burning of carbon and oxygen. The latter release an amount of energy comparable to the binding energy of the star which can be totally destroyed (pair-instability supernova) or lose a large fraction of its mass (pulsation pair-instability supernova) depending on the mass of the helium core.

This process, that has important implications in GW astrophysics as it shapes stellar BH mass distribution, was also ignored for many years by the star cluster N-body community and only it became popular after the LIGO/Virgo/Kagra observations. Therefore it have been included in the BSE package only in recent time Banerjee (2020). We discuss more in detail the effects that (pulsation) pair-instability supernova has on the outcome of direct N-body simulations in Chap. 4.

2.3.2 Collisions

Star clusters that are initially populated with a large fraction of primordial binaries are expected to host a large number of mergers. To model collisions, we adopt the manly the prescriptions given in BSE. Therefore, we assume that mergers involving red giants or red giant-like stars lead to common-envelope evolution; the envelope of the giant encircles both the two objects. The final outcome of this evolution depends on the orbital energy of the two cores as well as the binding energy of the envelope. If the latter is too low, the envelope might be removed from the two-body system before the two cores merge, leaving behind a binary composed of the appropriate remnants. Otherwise, the two cores spiral into each other. If a non red giant star collides with a BH, the two bodies instantly mergers as soon their separation is smaller then the tidal radius defined as:

$$r_{\rm tide} = 1.3 R_1 \left(\frac{M_1 + M_{BH}}{2M_1} \right)^{1/3} \tag{2.34}$$

where M_1 and $M_{\rm BH}$ are the masses of the star and the compact object respectively, and R_1 is the radius of the star. The mass of the final object $M_{\rm f}$ is set equal to:

$$M_{\rm f} = M_{\rm BH} + f_{\rm c} \times M_1, \tag{2.35}$$

where $0 < f_{\rm c} < 1$ represents fraction of stellar mass absorbed by the BH during the coalescence. In our work, we treat $f_{\rm c}$ as a free parameter and explore scenarios with different values of $f_{\rm c}$.

In order to ensure the collision between two compact objects, we need to include the effects of relativistic corrections. The procedure adopted in the first two projects of this thesis (respectively discussed in Chap. 3 and 4) includes the effect of GW energy loss of hard compact binaries using the average change of energy and angular momentum per orbit from Peters & Mathews (1963). This provides a good description of the orbital contraction and circularization driven by gravitational radiations until the time scale of orbit contraction becomes similar to the orbital time. When this occurs, the time to the final merger is very short and we assume coalescence. In our last work, we follow the close interactions of compact objects adopting the post-Newtonian expansion at the second-and-a-half order.

Chapter 3

Formation of Intermediate Mass Black Holes in Compact Star Clusters

The content of this chapter is based on the peer-reviewed and published paper Rizzuto et al. (2021b).

3.1 Abstract

Young dense massive star clusters are promising environments for the formation of intermediate mass black holes (IMBHs) through collisions. We present a set of 80 simulations carried out with NBODY6++GPU of 10 models of compact $\sim 7 \times 10^4 M_\odot$ star clusters with half-mass radii $R_\mathrm{h} \lesssim 1pc$, central densities $\rho_\mathrm{core} \gtrsim 10^5 M_\odot pc^{-3}$, and resolved stellar populations with 10% primordial binaries. Very massive stars (VMSs) up to $\sim 400 M_\odot$ grow rapidly by binary exchange and three-body scattering with stars in hard binaries. Assuming that in VMS - stellar BH collisions all stellar material is accreted onto the BH, IMBHs with masses up to $M_\mathrm{BH} \sim 350 M_\odot$ can form on timescales of $\lesssim$ 15 Myr, as qualitatively predicted from Monte Carlo MOCCA simulations. One model forms an IMBH of 140 $\mathrm{M}_\odot$ by three BH mergers with masses of 17 : 28, 25 : 45, 68 : 70 $\mathrm{M}_\odot$ within $\sim$ 90 Myr. Despite the stochastic nature of the process, formation efficiencies are higher in more compact clusters. Lower accretion fractions of 0.5 also result in IMBH formation. The process might fail for values as low as 0.1. The IMBHs can merge with stellar mass BHs in intermediate mass-ratio inspiral events (IMRIs) on a 100 Myr timescale. With 10^5 stars, 10 % binaries, stellar evolution, all relevant dynamical processes, and 300 Myr simulation time, our large suite of 80 simulations indicate another rapid IMBH formation channel in young and compact massive star clusters.

3.2 introduction

At the end of the 1930s Oppenheimer & Snyder (1939) suggested that after the exhaustion of all thermonuclear energy sources, heavy stars might collapse. The objects created in these events are stellar black holes (BH) with masses from 5 $M_\odot$ up to about 60 $M_\odot$ [1]. A large number of X-ray and optical observations provide solid evidence for the existence of stellar BHs (Webster & Murdin, 1972; Remillard & McClintock, 2006; Casares & Jonker, 2014). Their presence is further confirmed by the recent discovery of gravitational waves generated by BH mergers (Abbott et al., 2016, 2017, 2019). It is also well established that massive galaxies in the local Universe host supermassive black holes (SMBHs) with masses above 10^6 $M_\odot$ (see Kormendy & Ho, 2013, for a general review). Before the detection of GW190521 (Abbott et al., 2020) - which was published after the initial submission of this work - there was no clear observational evidence for the existence of BHs bridging the mass range between stellar and supermassive black holes. The 150 $M_\odot$ BH observed in the last LIGO/virgo detection, is the merger product between a 66 and a 85 $M_\odot$ black hole (Abbott et al., 2020). In general, intermediate-mass black holes (IMBHs) could originate from stellar BHs and might be the seeds for SMBHs. Finding them and understanding their formation mechanism is crucial for a full understanding of the BH population in the Universe. There are three theoretical paths for IMBH formation leading to SMBHs discussed in the literature (see reviews Volonteri, 2010; Koliopanos, 2017, and citations there). In the first scenario IMBHs form through direct collapse of dense gas at high redshifts. This scenario predicts the formation of IMBHs of 10^4 to 10^6 $M_\odot$ (Begelman et al., 2006; Agarwal et al., 2012; Luo et al., 2020). A second possibility is that IMBHs are the remnants of first generation (PopIII) stars. These stars formed from zero metallicity gas and are expected to collapse into IMBHs more massive than 100 $M_\odot$ (Madau & Rees, 2001; Ryu et al., 2016). A third family of models assumes that IMBHs are generated in dense stellar environments through runaway collisions. Several studies have demonstrated that IMBHs can form through dynamical interactions in dense stellar systems. Those studies include analytical approaches (Begelman & Rees, 1978; Stone et al., 2017) as well as N-body simulations (Portegies Zwart & McMillan, 2002; Portegies Zwart et al., 2004; Mapelli, 2016; DiCarlo et al., 2020), and Monte Carlo simulations (Freitag et al., 2006; Gürkan et al., 2006; Giersz et al., 2015). In particular, the effect of tidal capture of stars by BHs has been discussed in Patruno et al. (2006) for massive star clusters and Stone et al. (2017) for nuclear star clusters.

Several IMBHs candidates have been discovered in our galaxy and others nearby. For example, IMBHs have been proposed to explain the nature of ultra-luminous X-ray emitters (ULXs). ULXs are extra-galactic and off-center X-ray sources that could be generated by BHs of intermediate mass which accrete gas isotropically below the Eddington rate (Colbert & Mushotzky, 1999). Most ULXs observed are, however, more likely generated by smaller objects such as magnetized neutron stars and stellar BHs with super-Eddington accretion (Feng & Soria, 2011; Gladstone, 2013; Roberts et al., 2016; Kaaret et al., 2017; King & Lasota, 2020). This is also confirmed by dynamical evidence (Liu et al., 2013) as well as X-ray pulsations, which indicate the presence of neutron stars (Fürst et al., 2016). Nevertheless, there exists a group of hyper-luminous X-ray sources (HLXs) that might be laborious to explain by super-Eddington accretion since their luminosity exceeds $\sim 10^{41}$ erg s^{-1}. Probably the best IMBH candidate known so far is HLX-1. This HLX is believed to host an IMBH because it has an X-ray luminosity of 1.1×10^{42} erg s^{-1}

[1] The lower and upper mass boundaries depend on the stellar evolution model, i.e. details of stellar wind mass loss and supernova explosions

(Farrell et al., 2009). This luminosity would imply a mass of 500 $M_\odot$ even assuming an accretion rate ten times larger than the Eddington limit (Farrell et al., 2009). The mass estimates of the BH associated with HLX-1 is estimated between 3.0×10^3 and 3.0×10^5 $M_\odot$ (see review Mezcua, 2017, and references therein). Other notable sources in the same category are NGC 5252 and NGC 2276-3C, which have been estimated to host IMBHs of $\sim 10^5 M_\odot$ Kim et al. (2020) and $\sim 5 \times 10^4 M_\odot$ (Mezcua et al., 2013, 2015), respectively. Another HLX is M82 X-1. This X-ray source is associated with a young massive star cluster (MGG-11) in the starburst galaxy M82 (Matsumoto & Tsuru, 1999; Kaaret et al., 2001). First observations have suggested that it is generated by a BH with a mass of $200 - 5000$ $M_\odot$ (Kaaret et al., 2001; Matsumoto et al., 2001; Strohmayer & Mushotzky, 2003; Patruno et al., 2006). A more recent analysis indicates the presence of an IMBH, estimating its mass to ~ 400 $M_\odot$ (Pasham et al., 2014). However, M82 X-1 could still be a stellar mass BH with super-Eddington accretion (Brightman et al., 2016).

Globular clusters have been popular targets for the search of IMBHs. Due to their high central density, and possibly even higher density at formation (Lahén et al., 2019), they provide a promising environment for the formation of IMBHs through runaway core-collapse and collision. Many studies have attempted to detect IMBHs in globular clusters through their accretion signatures. However, so far G1 in M31 is the only globular cluster detected in X-rays (Pooley & Rappaport, 2006; Kong, 2007). This signal might be generated by an IMBH with a mass of about 2×10^4 $M_\odot$ (Gebhardt et al., 2002, 2005). A recent observational study reports the lack of IMBHs accretion signatures in 19 globular clusters located in the early-type galaxy NGC 3115 (Wrobel & Nyland, 2020). Observations based on kinematic measurements might suggest the presence of IMBHs in globular clusters such as M15 (Bahcall & Wolf, 1976; Peterson et al., 1989), ω Centauri (Noyola et al., 2008, 2010), NGC 1904 and NGC 6266 (Lützgendorf et al., 2013). However, these observations could also be explained by a central concentration of compact objects (Baumgardt et al., 2003; van den Bosch et al., 2006; Baumgardt et al., 2020). Measurements of pulsar accelerations indicate that the globular cluster 47 Tucanae might host an IMBH of 2300^{+1500}_{-850} $M_\odot$ (Kızıltan et al., 2017). Another study suggests, that current observations of pulsar accelerations are insufficient to confirm the presence of an IMBH in 47 Tucanae, they can only be used to estimate an upper limits on its mass Abbate et al. (2018).

Dwarf galaxies are very promising systems for IMBH searches. NGC 4395 seems to be one of the most plausible candidates for an active and central IMBH. Observations of the central stellar velocity dispersion reveal a value of 30 km/s (Filippenko & Ho, 2003), suggesting an IMBH mass of $\sim 10^5$ $M_\odot$. Further measurements based on the broad profile of the Hβ line, from X-ray variability (Filippenko & Ho, 2003), reverberation mapping (Peterson et al., 2006; Edri et al., 2012), and integral field kinematics (den Brok et al., 2015) indicate a mass in the range between 10^4 to 10^5 $M_\odot$. Also our Galaxy might host an IMBH in the vicinity of the galactic center as suggested by recent high-resolution molecular line observations that indicates the presence of a $\sim 10^4$ $M_\odot$ candidate BH in the central region of the Milky Way (Takekawa et al., 2020).

In this chapter, we study IMBH formation paths in young concentrated star clusters with numerical simulations. The simulations incorporate detailed models for single and binary stellar evolution as well as mass loss due to stellar winds. In Section 2, we describe the N-body code used to simulate star cluster evolution and focus on the description of the adopted stellar evolution and collision models. In Section 3, we describe the initial conditions for our models. The results

Model Name	r_c pc	ρ_c $M_\odot$ / pc ^{3}	W_0	R_h pc	σ km/s	t_{rh} Myr	t_s Myr	f_c	# IMBH	M_{IMBH} $M_\odot$	t_{form} Myr	M_*/M_{IMBH}
R06W9F01	0.04	3.0×10^7	9	0.6	15	56	1.4	0.1	0/8	/	/	/
R06W9F05	0.04	3.0×10^7	9	0.6	15	56	1.4	0.5	2/8	138, 110	5.5, 6.3	79%, 81%,
R06W6	0.19	1.1×10^5	6	0.6	15	56	1.4	1.0	4/8	307, 151, 138, 122	8.6, 83.9, 6.4, 8.4	86%, 26%, 72%, 80%
R06W7	0.13	5.0×10^5	7	0.6	15	56	1.4	1.0	2/8	148, 147	22.9 , 8.2	76%, 87%
R06W8	0.06	3.0×10^6	8	0.6	15	56	1.4	1.0	3/8	336, 171,110	6.6, 12.3, 8.1	98%, 87%, 77%
R06W9	0.04	3.0×10^7	9	0.6	15	56	1.4	1.0	3/8	355, 349, 120	8.57, 8.19, 16.3	81%, 89 %, 73 %
R1W7	0.2	1.0×10^5	7	1.0	12	120	3.0	1.0	0/8	/	/	/
R1W8	0.11	4.0×10^5	8	1.0	12	120	3.0	1.0	0/8	/	/	/
R1W9	0.05	3.0×10^6	9	1.0	12	120	3.0	1.0	1/8	239	16.4	92%
R1W10	0.03	1.8×10^7	10	1.0	12	120	3.0	1.0	2/8	133, 110	13.2, 7.8	83%, 83 %

Table 3.1: Model parameters of the cluster simulations: r_c : initial core radius; ρ_c : initial central density; W_0 : central potential parameter for the King density profile (King, 1966); R_h : half mass radius; σ : dispersion velocity; t_{rh}: half mass relaxation time computed using eq. 3.3 with $\gamma = 0.02$; t_s: segregation time scale for 100 $M_\odot$ objects computed using eq. 3.4; f_c : fraction of mass absorbed by a compact object during a direct collision with a star; # IMBH : Number of BHs with masses $\geq$ 100 $M_\odot$ formed out of 8 realisations; M_{IMBH}: IMBH masses; t_{form}: IMBHs formation times; M_*/M_{IMBH}: the total stellar mass accreted by the IMBH divided by its final mass.

of our simulations are discussed in Section 4. In Section 5 we compare these results with previous studies. In the final section we summarise the main points of this chapter.

3.3 The Method

To investigate the possible formation of IMBHs in massive star clusters we generated initial conditions for 80 isolated systems[2] using MCLUSTER (Küpper et al., 2011). The systems were set up with two different half-mass radii and various central concentrations. Each initial condition is evolved for a few hundred million years employing NBODY6++GPU (Wang et al., 2015, 2016), a direct N-body simulation code designed to follow the dynamical and stellar evolution of individual stars and binaries.

3.3.1 NBODY6++GPU

NBODY6++GPU[3] is a high-precision direct N-body simulation code based on the earlier N-body codes NBODY1-6 (Aarseth, 1999) and NBODY6++ (Spurzem, 1999). For time integration it uses the Hermite scheme. This together with the hierarchically blocked variable time step scheme allows an efficient parallelization of the code for massively parallel supercomputers (since nbody6++); gravitational forces between particles are offloaded to graphics processing units (GPUs), used for high-performance general purpose computing (NBODY6++GPU, Wang et al. (2015)). The parallelisation is achieved via MPI and OpenMP on the top level, distributing work within a group of particles due for time integration, and efficient parallel use of GPU cores at the base

[2]We study clusters in isolation to investigate internal dynamical effects without possible external influences.
[3]Link to repository: http://silkroad.bao.ac.cn/repos/Nbody6++GPU-Aug2020/

level (every MPI process using a GPU), for computing the gravitational forces between particles. The GPU implementation in NBODY6++GPU provides a significant performance improvement, especially for the long-range (regular) gravitational forces (see Nitadori & Aarseth, 2012; Wang et al., 2015, 2016).

The code accurately computes the evolution of binaries, multiples and close encounters between them and single stars and between multiple systems, using the Kustaanheimo-Stiefel (KS, Kustaanheimo & Stiefel, 1965) regularisation with the classical chain algorithm by Mikkola & Aarseth (1998). It also follows single and binary stellar evolution based on the SSE and BSE recipes by Hurley (see Sect. 3.3.2), including also rapid tidal circularization for binaries with small pericenters and tidal captures according to the prescription given in Mardling & Aarseth (2001), which is based on the previous work of Press & Teukolsky (1977); Lee & Ostriker (1986); Mardling (1996). The integrator fully resolves orbits and dynamical evolution of binaries, even during phases of mass loss or when one of the two stars undergoes a supernova explosion. The binary orbit is adjusted to the corresponding loss of mass, energy and angular momentum with appropriate time stepping; in case of a supernova explosion it is always ensuring that the remnant and its companion leave the explosion with the corrected orbital positions and velocities.

In the implementation used for this study we compute the gravitational wave energy loss of hard binaries according to the orbit averaged approximation of Peters & Mathews (1963), using the average change of energy and angular momentum per orbit from their work. At each KS integration time-step, which is much smaller than the orbital time, we apply a corresponding fractional loss of energy and angular momentum. This allows for the proper representation of the evolution of gravitational radiation driven shrinking and circularization of the orbit, until the time scale of orbit shrinking becomes comparable to the orbital time. When this happens, the time to final coalescence is very short and we assume coalescence. Relativistic kicks are not included in the current implementation.

The publicly available code NBODY6++GPU has been significantly upgraded in three respects:

1. For collisions between a compact remnant and a main sequence star or red giant a free parameter f_c is introduced, which described the mass loss from the system in the process. The previous NBODY6 versions used only $f_c = 1$, i.e. no mass loss in the process (see Eq. (1) and (2) above). Routine involved: `coal.f`.

2. Simultaneous treatment of classical tidal interactions (Roche lobe overflow) and Post-Newtonian orbit-averaged orbit shrinking due to gravitational wave emission has been made possible. Both are treated technically in a similar way, and can now be switched on together. Routines and parameters involved: `ksint.f, kstide.f, tides3.f, KZ(27)`.

3. Strongly bound binaries of two compact objects, which are subject to Post-Newtonian relativistic energy loss are prevented from chain integration: they are treated exclusively in the two-body KS integrator. Routine involved: `impact.f`.

3.3.2 Stellar Evolution

The simulations in this chapter were performed with the same stellar evolution models as the DRAGON simulations presented in Wang et al. (2016). Stellar evolution is implemented using analytical fits to the models of (Eggleton et al., 1989, 1990) developed by (Hurley et al., 2000) and (**?**) for single stars (SSE) and by (Hurley et al., 2002) for binary stars (BSE). A few updates were included for strong kicks at neutron star birth (Hobbs et al., 2005) and for fallback and more massive black hole formation of massive stars at low metallicities (Belczynski et al., 2002).

The code is able to follow the main properties of single stars (such as radius, mass, luminosity, and core mass) from the zero-age main-sequence to the remnant stage. This also includes mass loss due to stellar winds for a wide range of masses and metallicities. As long as the orbit of a binary star is wide enough, the evolution of each star is assumed not to be affected by its companion and just the single star tracks are used. However, if one of the two stars is losing mass by a stellar wind, the companion has the chance to accrete material and deviate from its standard evolution. For close enough orbits either star might fill its Roche-lobe leading to mass transfer. For these cases, the code computes the accretion rate as a function of the masses, the radii, the stellar types, and the separation of the donor and the accretor, ensuring that it never exceeds 100 times the Eddington limit. If the matter ejected by a star is not entirely absorbed by its companion it might accumulate in a common envelope around the two stars. All the above effects: mass transfer, Roche phase, and common envelope evolution have significant consequences for the orbit and stellar properties of the binary and are included in the simulations based on the models of Tout et al. (1997).

Our stellar evolution treatment does not include the latest stellar winds prescriptions. With our recipes, an isolated star, independently on its initial mass, can never form a BH with a mass larger than 30 $M_\odot$. On the contrary, according to most updated models (Vink et al., 2000; Gräfener & Hamann, 2008; Vink et al., 2011; Sander & Vink, 2020), a massive star with low zero-age main-sequence metallicity is expected to lose little mass through stellar winds. At the same time, non-rotating metal-poor stars in the mass range between 70 and 140 $M_\odot$ are expected to end their life as pulsational pair-instability supernovae (PPISN); consequently, they are expected to eject a large fraction of their masses leaving a BH remnant with a maximum mass of about 40 − 50 $M_\odot$ (Heger et al., 2003; Woosley, 2017). Metal-poor stars, with mass at least 140 $M_\odot$ up to roughly 260 $M_\odot$, will experience a single violent pulse that disrupts the entire star as a pair-instability supernova (PISN); no remnant is left behind. Our simulations do not include treatments for PPISN and PISN. The absence of these two effects together with the conservative stellar winds model adopted, might have altered the dynamical processes that lead to the formation of the IMBHs. Therefore, with an updated prescription of stellar winds and with treatments for PPISN and PISN we might obtain different masses of the IMBHs.

In dense environments, where stellar collision rates are high, runaway collisions (Lee, 1987; & Shapiro, 1987; Quinlan & Shapiro, 1989, 1990), can generate stars above the maximum IMF mass of 100 $M_\odot$ (Portegies Zwart & McMillan, 2002; Portegies Zwart et al., 2004; Gürkan et al., 2004; Mapelli, 2016; DiCarlo et al., 2020; Wang et al., 2020) for which we use the term "very massive stars" (VMS). To track the evolution of VMSs, in the absence of observational constraints, we extrapolate our stellar evolution model to stars with arbitrary large masses. Therefore, VMSs are affected by strong stellar wind mass loss and lose a significant fraction of their mass during their lifetime. In our stellar evolution framework, it is therefore impossible to form massive BHs from direct stellar collapse. In fact, with the adopted stellar evolution recipes, even an isolated star with a mass of 500 $M_{\odot}$ generates a BH of only about 30 $M_{\odot}$.

It is worth mentioning that theories of stellar evolution predict that a low metallicity star more massive than 260 $M_{\odot}$ collapses directly into a BH without significant mass loss in supernova explosions (see Woosley & Heger, 2015, and citations therein). However, it is important to take into account the complex stellar structure acquired by VMSs during merger events. A detailed computation of the evolution of collision products shows that, VMSs formed through runaway collisions and tidal capture, are dominated by mass loss from stellar winds that drastically reduce their final remnant mass (Glebbeek et al., 2009).

Despite using a stellar evolution model where stellar winds strongly affects the most massive stars and direct collapse into IMBHs is not possible we can still form BHs more massive than 100 $M_{\odot}$ through BH-BH and BH-star collisions. We will show, in the next sections, that BH-VMS collisions provide the main channel for the formation of IMBHs. In other words, our results show that black holes with a mass above 100 $M_{\odot}$ form when a stellar black hole merges with a VMS in agreement with revious works (Giersz et al., 2015; Mapelli, 2016). Runaway tidal captures (Stone et al., 2017) can also produce IMBHs.

3.3.3 Collisions

The outcome of a collision depends on the relative velocity, the relative sizes and the internal structure of the two colliding objects. In general, full 3D radiation magneto-hydrodynamical simulations are required to robustly determine the properties of the final object (such as mass, size, and internal structure). In the absence of results covering the full parameter space NBODY6++GPU adopts a simplified treatment. If a collision does not involve red giants the two objects are merged when the radii of two colliding objects overlap and the merger of the two masses is assumed to be instantaneous. If M_1 and M_2 are the masses of two stars or two compact objects (black holes, neutron stars, withe dwarf, etc.), the final object will have a mass $M_{\rm f}$ equal to:

$$M_{\rm f} = M_1 + M_2. \tag{3.1}$$

Otherwise, if M_1 is the mass of a compact object and M_2 is the mass of a star, the final mass of the compact object, $M_{\rm f}$, is given by:

$$M_{\rm f} = M_1 + f_{\rm c} \times M_2, \tag{3.2}$$

where $0 < f_{\rm c} < 1$ represents the amount of stellar material falling back and accreted onto the black hole during the coalescence.

The value of $f_{\rm c}$ has been debated in the literature only for tidal disruption events involving a SMBH and a low mass star ($M_{BH} >> M_*$). Several analytical and numerical studies indicate $0.25 < f_{\rm c} < 0.5$ (Shiokawa et al., 2015; Law-Smith et al., 2019; Lu & Bonnerot, 2020; Bonnerot & Lu, 2020) in agreement with a recent observational work Wen et al. (2020). The latter shows that in some tidal distruption events, $f_{\rm c}$ can be measured, and has a value in the range between

0.2 – 0.5. Another work explores the scenario in which most of the stellar material is ejected in an outflow during the tidal interaction with the SMBH arguing that $f_c < 0.1$ is not impossible (Metzger & Stone, 2016).

Our case of interest ($M_{BH} \lesssim M_*$) is more uncertain and needs future investigation. In our theoretical work, we treat f_c as a free parameter and explore scenarios with $f_c = 0.1, 0.5$, and 1.0 (see Fig. 3.10). Here we anticipate that the main IMBH formation mechanism proposed in this work is strongly suppressed when $f_c = 0.1$.

Collisions involving a giant or giant-like star with a dense core and a large envelope are assumed to lead to common-envelope evolution. In this situation the envelope of the red giant wraps around both cores of the two objects [4]. The outcome depends on the orbital energy of the two cores as well as the binding energy of the envelope. If the latter is too low, the wrapper might be removed from the system before the two cores merge, leaving behind a binary composed of the appropriate remnants. Otherwise, the two cores are destined to spiral into each other. The final mass depends on their relative density. If they are of different compactness, equation 3.2 applies, otherwise the code uses 3.1.

When two stars of similar compactness merge, we assume that they coalesce and mix completely. As a consequence the final star can be rejuvenated since the core of the final object absorbs new fuel. This phenomenon is well established as it explains the peculiar evolution of blue stragglers as the product of binary evolution and direct stellar collisions (Smith & Tombleson, 2015; Davies et al., 2004; Davies, 2015). This rejuvenation procedure also applies to MS stars, even if they are assumed to have no core. For more details see section 2.6.6 of Hurley et al. (2002).

When two black holes (or neutron stars) form hard binaries, gravitational waves emission is computed with the Peters & Mathews formulae (Peters & Mathews, 1963). The semi-major axes and the eccentricities are then changed according to the amount of gravitational wave energy emitted.

3.4 Initial Conditions

We created initial conditions for 10 isolated [5] star cluster models following a King density profile (King, 1966) with two different half-mass radii and five different central densities varying the dimensionless central potential parameter $6 \leq W_0 \leq 10$. For a fixed value of the half-mass radius, the central density increases with increasing W_0 [6] (see Fig. 3.1). All simulated clusters were initialized with a very low metallicity of $Z = 0.0002$ and $N = 1.1 \times 10^5$ stars sampled from a Kroupa IMF (Kroupa, 2001) as zero-age main-sequence stars in a mass range of 0.08 $M_\odot$ to 100 $M_\odot$ (see Fig. 3.2). No primordial mass segregation was included. Because of computing

[4] For main sequence stars and black holes, the core mass coincides with the mass of the objects itself.

[5] According to the code, a star escapes from an isolated cluster when its energy is larger than zero, $E > 0$ and its distance from the center is larger than $30R_h$.

[6] The exact definition of the parameter $W_0 = \frac{\psi(0)}{\sigma^2}$ where $\psi(0)$ is the potential at the center of the cluster and $\sigma^2$is a parameter connect to the velocity dispersion defined from the distribution function; see (King, 1966) section 3 and (Heggie & Hut, 2003) chapter 8 for more details.

Model Name	R_{h} pc	σ km/s	N	t_{rh} Myr	M_f/M_i
R06W6	2.45	6.09	106800	519	0.695
R06W7	2.57	5.93	106400	573	0.693
R06W8	2.69	5.71.	106700	620	0.690
R06W9	2.82	5.56	105900	671	0.688
R1W7	2.92	5.48	107800	772	0.702
R1W8	3.11	5.41	107500	820	0.698
R1W9	3.24	5.33	107200	860	0.692
R1W10	3.41	5.25	106700	894	0.689

Table 3.2: Half mass radius R_{h}, dispersion velocity σ, half mass relaxation time t_{rh}, number of particles N, and final to initial total cluster mass ratio M_f/M_i after 300 Myr; where M_i is the initial mass of the cluster while M_f is the final mass of the cluster.

performance limit, we did not use very high primordial binary fraction as suggested by some observations (Sana et al., 2012; Moe & Di Stefano, 2017). Our clusters are initialized with 10.000 initial binaries (a primordial binary fraction of 10%) with a uniform semi-major axis distribution on a logarithmic scale from 0.001 AU to 100 AU [7], a uniform distribution of mass ratios, and a thermal distribution of eccentricities; With this binary distribution about 30% of the primordial binaries are weak and they dissolve in the cluster at the beginning of the simulation. For each initial condition parameter set we created 8 realisations with different random number seeds. In Tab. 3.1 we list the initial conditions parameters of the 10 models including the number of realizations that lead to the formation of IMBHs and their respective masses. All simulations were run for more than 300 Myr up to 500 Myr[8].

The clusters studied in this work are initialized with a low metallicity value (about two orders of magnitude lower then the solar metallicity), they are rather compact with high initial central densities and small half-mass radii. For this reason, they do not resemble the typical properties of young massive star clusters (YMSCs) in the observable range. The latter have higher, and closer to solar, metallicity and are typically less compact; observed YMSCs with masses similar to our models have virial radii typically in the range from 3 to 30 pc (Portegies Zwart et al., 2010). Even considering the expansion driven by stellar and dynamical evolution our less compact systems would have a virial radius from 2 to 30 times smaller then most of the observed massive clusters.

However, it is still possible to find a few compact YMSCs in the local Universe. An example is Westerlund 1, which has a virial radius of ~ 1.7 pc (our $R_{\mathrm{h}} = 0.6$ pc model at the same age has a virial radius of about 1.15 pc) and a mass $\sim 6 \times 10^4\ \mathrm{M}_{\odot}$ (Mengel & Tacconi-Garman, 2007; Portegies Zwart et al., 2010). Another exception is MGG-11 in M82. This cluster has a half-light radius of about 1.2 pc and a mass of about $3.50 \times 10^5\ \mathrm{M}_{\odot}$ (McCrady et al., 2003).

Our models start with velocity dispersions σ between 15 km/s and 12 km/s (see Tab. 3.1)

[7]To generate the semi-major axis distribution we impose the further constraint that the initial semi-major axes of each binary are larger than the sum of the diameters of the two stars.

[8]We evolved for longer time the clusters that formed an IMBH to check whether the BH would keep growing in mass or it would be ejected from the cluster through a strong interaction.

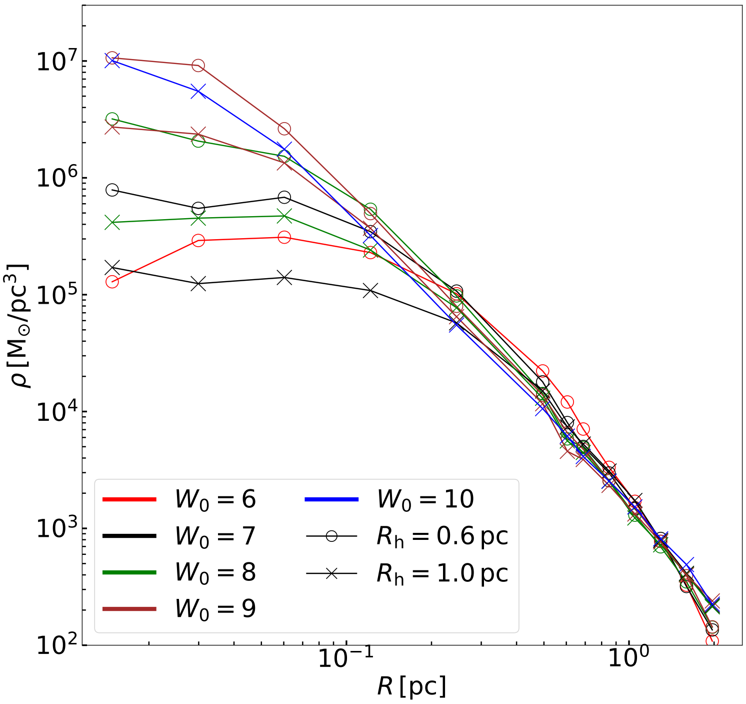

Figure 3.1: Initial density distributions for the cluster simulations presented in Tab. 3.1, initialized with a King density profile (King, 1966) with two half-mass radii and different central potential parameters W_0 (different colours). Systems with $R_h = 0.6$ pc are represented with filled circles while models with $R_h = 1.0$ pc are represented by crosses.

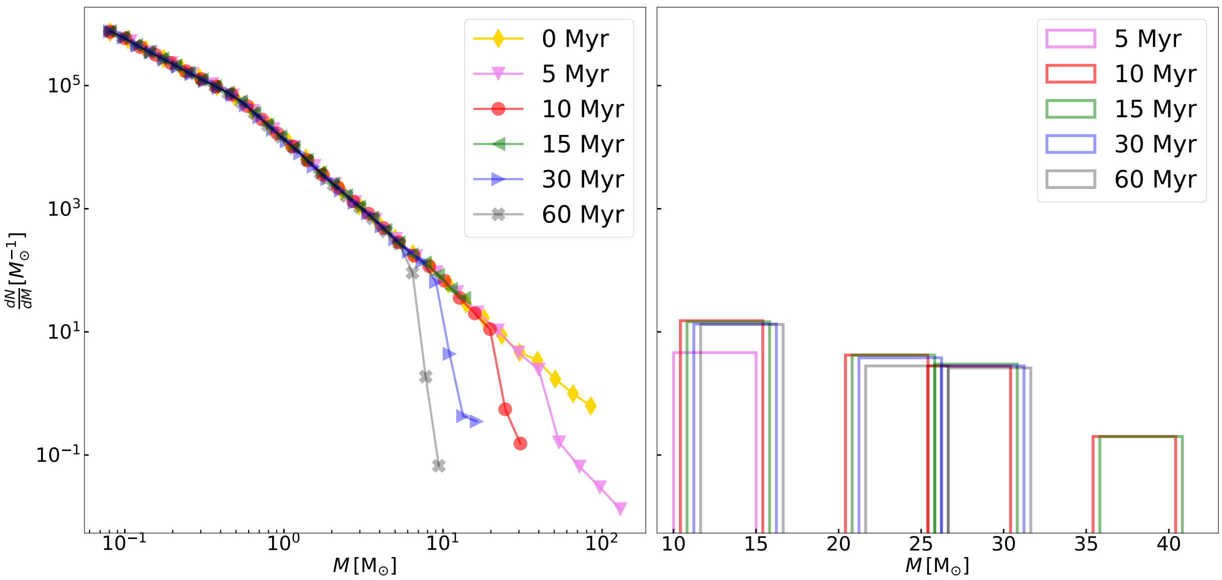

Figure 3.2: Left panel: stellar mass function (the mass function is computed including all stellar types apart from compact objects) at 0, 5, 10, 15, 30 and 60 Myr. Right panel: compact objects mass function (the mass function includes only BHs, all neutron stars are ejected from the cluster due to supernovae kick.) at 0.0, 5, 10, 15, 30 and 60 Myr.

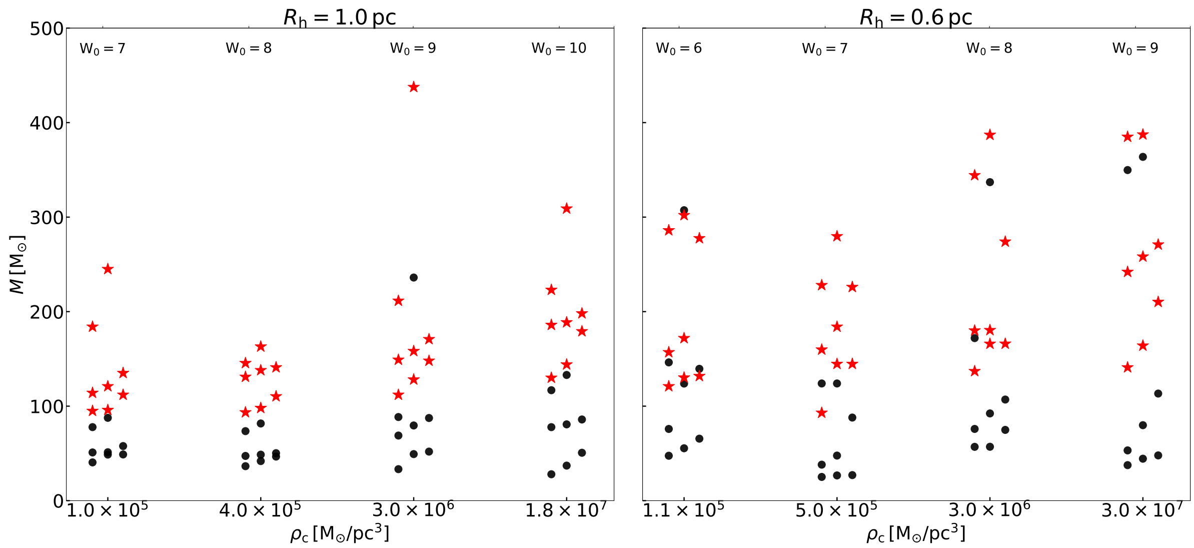

Figure 3.3: Peak masses of the very massive stars (VMS) formed by collisions (red stars) and black holes (black circles) for all simulations with $f_c = 1$ sorted by initial core density (see Tab. 3.1). The left (right) panel shows models with a half-mass radius of $r_h = 1$ pc ($r_h = 0.6$ pc). Each model has 8 realizations (plotted with random offset). W_0 does not seem to have a strong impact on the final black hole mass. A larger cluster half-mass radius apparently makes black holes mass growth less likely (left panel).

which drop to values between 6.1 km/s and 5.3 km/s after 300 Myr as shown in Tab. 3.2. We also show the half mass radius, the relaxation time, the number of particles and fraction of total mass left in the cluster after 300 Myr. It is interesting to notice that R06W9, which formed the most massive IMBHs, after 300 Myr has a dispersion velocity and half mass radius very similar to the least compact model R1W7 (see table 3.2), which never formed a BH more massive than 100 $M_\odot$. The velocity dispersions are shown in Tab. 3.2 are approximately in the same range of the observed values of the globular clusters in our Galaxy (Baumgardt & Hilker, 2018). However, our clusters are too small to resemble the initial conditions of present-day globular clusters and estimating the particle number of our clusters at late times using equation 22 in Gieles et al. (2011), our systems might not survive for 10 Gyr even if we assume no external tidal forces.

We have chosen these initial conditions mainly to investigate the formations of IMBHs through dynamical interactions. Nevertheless, our theoretical models might approximate the properties of clusters formed at a high redshift, which may be located around any galaxy in the LIGO/Virgo sensitivity volume (~ 1 Gpc^3).

3.5 Results

The dynamical evolution of a star cluster is dominated by two-body relaxation on time scales longer than the relaxation time (Spitzer, 1987) :

$$t_{\rm rh} = \frac{0.138 N^{1/2}}{\ln \Lambda} \left(\frac{R_{\rm h}^3}{G\bar{m}} \right)^{1/2} . \tag{3.3}$$

Here N is the number of stars in the cluster, $R_{\rm h}$ is the half mass radius and, $\bar{m}$ is the average star mass of the cluster and the argument of the Coulomb logarithm is $\Lambda = \gamma N$. Numerical experiments indicates a value for the parameter $\gamma = 0.11$ for single-mass systems (Giersz & Heggie, 1994) and $\gamma = 0.02$ for multi-mass stellar systems (Giersz & Heggie, 1996). We have used Eq. 3.3 to estimate half-mass relaxation times of 56 Myr and 120 Myr for systems with 0.6 pc and 1 pc half-mass radii, respectively (see Tab. 3.1).

The internal structure of star clusters evolves into a dense hot core and an extended halo. Since bound self-gravitating systems have negative heat capacity (Lynden-Bell & Wood, 1968; Lynden-Bell, 1999), the center will keep releasing energy to the outer part and contracts in a core collapse. In an isolated equal-mass system, this happens on the order of $15 t_{\rm rh}$ (Cohn, 1980). In clusters with a broad mass spectrum, low mass stars gain kinetic energy when interacting with massive stars; the former tend to expand their orbits, while the latter tend to lose kinetic energy and segregate to the central part of the cluster. In this case, core collapse is driven by the amassing of heavy stars in the core that typically occur in a time scale of the order of the segregation time (Spitzer & Hart, 1971; Portegies Zwart et al., 2004):

$$t_{\rm s} = \frac{\bar{m}}{M_{\rm max}} \frac{0.138 N}{\ln\left(0.11 M / M_{\rm max}\right)} \left(\frac{R_{\rm h}^3}{GM} \right)^{1/2} \tag{3.4}$$

where $M_{\rm max}$ is the mass of the most massive object in the cluster and M is the total mass of the cluster . Consequently multi-mass clusters undergo core collapse in much shorter time then single-mass systems. According to equation 3.4 our $R_{\rm h} = 0.6$ pc and $R_{\rm h} = 1.0$ pc models are expected to experience mass segregation at $t_{\rm s} \sim 1.4$ and 3 Myr respectively (see Tab. 3.1).

Core collapse lead to dramatic growth in the central density which in turn triggers violent few-body interactions between single stars and binaries, either primordial or dynamically formed. By means of this interaction binary stars release energy in the core and balance the loss of energy from the centre preventing the core to collapse further (see Heggie & Hut, 2003, and references therein).

We show in Fig. 3.3 that the most massive stars formed in each simulation (red crosses) consistently have masses much higher than the initial limit of 100 $M_\odot$. These system have formed by mergers of lower mass main sequence stars. As described in section 3.3.2 our stellar evolution recipes do not allow for the formation of a stellar black hole more massive than 30 $M_\odot$. Nevertheless, Fig. 3.3 demonstrates that several cluster systems generate BHs more massive than 100 $M_\odot$. In our framework, the only possible way to grow such a massive object is through dynamical interactions (see Sec. 3.5.1).

The likelihood to form a very massive star by mergers or tidal captures seems to be correlated with the compactness of the cluster. Only 6 star clusters with $R_{\rm h} = 1.0$ pc form stars with masses above 200 $M_{\odot}$, while clusters with $R_{\rm h} = 0.6$ pc form 15 stars more massive than 200 $M_{\odot}$ (see Fig. 3.3). Those stars play an important role in the production of IMBHs as their collisions with stellar BH are the main IMBH formation channel. Such a formation path for IMBHs has been predicted by Monte-Carlo models (Giersz et al., 2015) and is discussed in more detail below.

3.5.1 Intermediate Mass Black Hole Formation

Figure 3.4 illustrates how IMBHs of a few hundred solar masses are typically generated in our simulations. The formation consists of three main steps. First, a sequence of binary stellar collisions, triggered by triple interactions and hyperbolic collisions generates a VMS which can live up to 10 Myr due to mixing rejuvenation (see section 3.3.2). Second, in a merger with a stellar mass BH, a great part of the mass of the VMS is absorbed by the BH. In a third step, the IMBH can grow in mass by collisions with other stellar BHs. Our results indicate that, for our models, the dominant process for the formation of IMBHs is a collision between a VMS and a stellar mass BH. This type of collisions can lead to the formation of IMBHs of up to 350 $M_{\odot}$ within the first 10 Myr of cluster evolution. Our simulations also indicate that after all massive stars disappear from the cluster, the IMBH can still grow moderately in mass by merging with other stellar mass black holes and other types of stars.

The IMBH formation scenario shown in our work might change with the inclusion of PPISN, PISN prescriptions and updated stellar winds recipes. Although the inclusion of these treatments should not prevent the dynamical formation of IMBHs shown by our simulations, further investigation in this direction must be done in order to understand how these effects can influence our final outcome.

Our most compact models register about 300 collisions within 300 Myr, 40% of which happen in the first 15 Myr. Most of these collisions are triggered by three-body scattering events [9] between a hard binary and a third particle. These interactions have the overall effect of increasing the binding energy of the binaries and they can also raise their eccentricity (Heggie, 1975; Nash & Monaghan, 1978; Hut & Bahcall, 1983; McMillan & Hut, 1996). In general, when the distance of closest approach of the third object is comparable with the semi-major axis of the hard binary, the net effect of the interaction is to harden the binary (Heggie, 1975; Nash & Monaghan, 1978; Hut & Bahcall, 1983; McMillan & Hut, 1996). On the other hand, when the pericenter of the intruder is considerably larger then the size of the binary, the interaction is approximately adiabatic, and there is no exchange of energy between the binary and the intruder. However, the binary and the third object can form a hierarchical triple, which excites the eccentricity of the inner binary to values close to unity (Lidov, 1962; Kozai, 1962) and induces the two components of the binary to merge. Figure 3.5 illustrates the dynamical process leading to the collsion of two massive stars with 170 and 80 $M_{\odot}$, respectively. The 170 $M_{\odot}$ star approaches a binary (0.1 – 80 $M_{\odot}$) in a

[9] About 2% of collisions are hyperbolic.

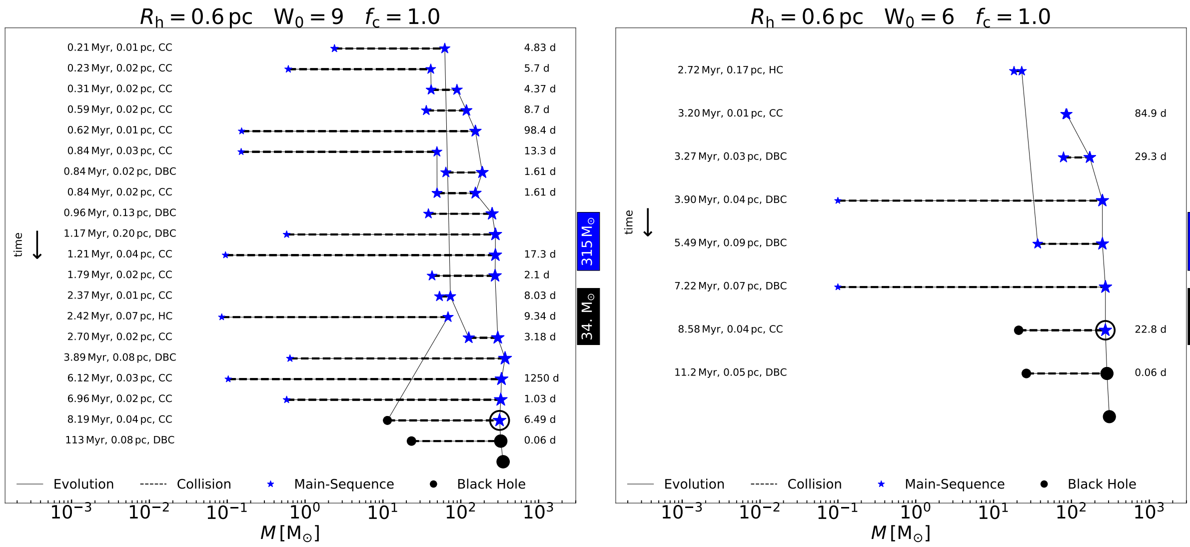

Figure 3.4: The left panel shows - from top to bottom - the formation history of an IMBH in a simulation with $W_0 = 9$, $R_h = 0.6$ pc and $f_c = 1.0$. A massive main-sequence star (MS, blue) grows by mergers (dashed horizontal lines) with other MS stars and evolves into ≈ 300 $M_\odot$ MS star colliding with a 10 $M_\odot$ BH, forming an IMBH about 8.2 Myr after the start of the simulation (the open black circle indicates the collision that leads to the formation of the IMBH.) . At about 113 Myr the IMBH collides with an other BH. In a similar fashion, an IMBH of about 300 $M_\odot$ is generated in a lower density cluster with $W_0 = 6$, $R_h = 0.6$ pc and $f_c = 1.0$ just with less merger of more massive stars (right panel). In each panel we indicate the time of the collision after the start of the simulation in Myr and the radius from the center in pc. We also characterise the type interaction in the following way: **BC**: Binary collision - the two colliding objects formed a binary before the collision, **PBC**: the binary is primordial, **DBC** the binary has formed dynamically, **HC**: hyperbolic collision, **CC**: chain collision - all collisions not classified as **DBC** or **HC**. If the two colliding objects formed a binary before coalescence the period is given in d. In the blue (black) boxes we indicate the amount of stellar (black hole) material accreted by the IMBH. Here it is important to mention that the figure shows all collisions experienced by each participant; if an object appears in the plot only once it implies that the object never experiences any collision before.

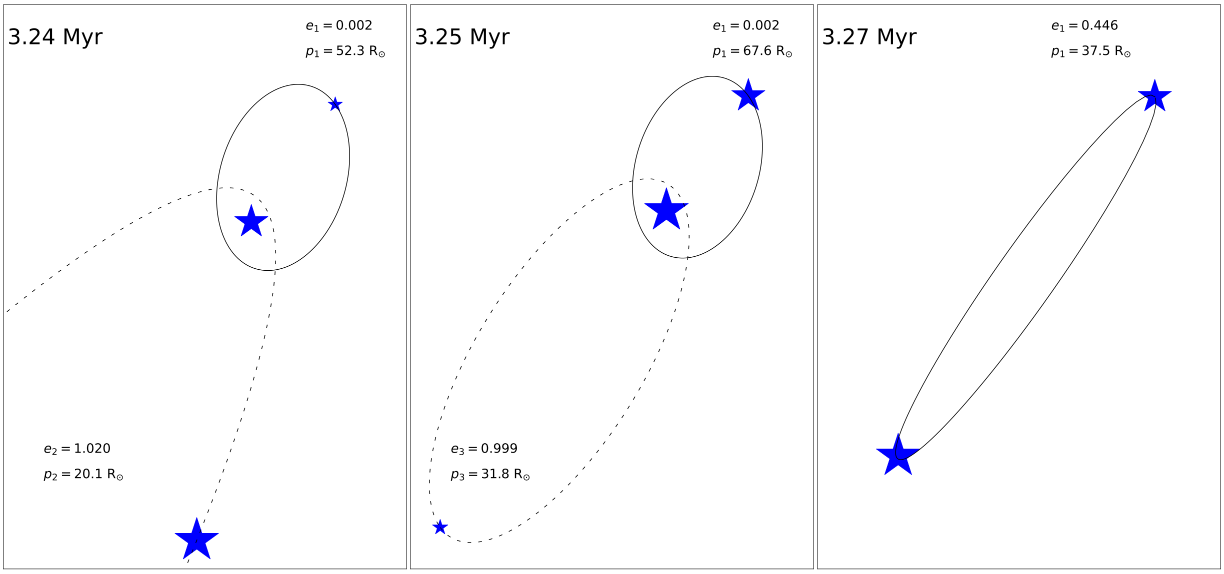

Figure 3.5: Sketch of the triple interaction that induces the collision of two massive stars of 170 and 80 M$_\odot$. Left panel: the 170 M$_\odot$ approaches a binary in a hyperbolic orbit. Central panel: the exchange between the lightest component of the binary and the intruder of 170 M$_\odot$. Right panel: the perturbed 170-80 M$_\odot$ binary increase its eccentricity, the two components are about to merge.

hyperbolic orbit (left panel); during the interaction, the intruder forms a hard binary with the 80 M$_\odot$ star, while the lightest component escapes in a wider orbit (panel 2). Due to the perturbation of the third object the eccentricity of the new $170-80$ M$_\odot$ binary increases from 0.002 to 0.45 and the two massive stars crash into each other. Figure 3.5 also shows that the colliding objects do not necessarily need to be in a primordial binary. Exchanges are very frequent in triple interactions. Typically, encounters leading to exchange increase the mass of the components of a hard binary because the lowest mass is most likely to escape (see Heggie & Hut, 2003, and references therein).

In summary, when a single object interacts with hard binaries, the binaries tend to harden and become more massive, and they also gain angular momentum and eccentricity. For all these reasons triple interactions drive the chain of star-star collisions leading to the formation of VMSs. They are also the main process that triggering BHs-VMSs mergers (see Fig. 3.6).

Here it is important to mention that relativistic kicks are not implemented in our simulations. Theoretically, an IMBH could be ejected from the cluster by gravitational wave recoil after a collision with one of the stellar mass BHs left in the system. However, except for of the simulation illustrated in Fig. 3.7, we expect the clusters to have good chances of retaining their IMBHs as the IMBH - BH mass ratio is small (figure 3.4 shows the typical mass ratio in a collision between an IMBH and a stellar BH: $\frac{m_{BH}}{M_{IMBH}} \approx \frac{20}{300} \approx 0.067$). According to **?**Baker et al. (2008); Lousto & Zlochower (2009); Kulier et al. (2015); Morawski et al. (2018); Zivancev et al. (2020) the maximum gravitational velocity kick is $\sim (0.067)^2 \times 4000$ km/s ~ 18 km/s and it is smaller than the cluster escape velocity in the core that is about 25 km/s.

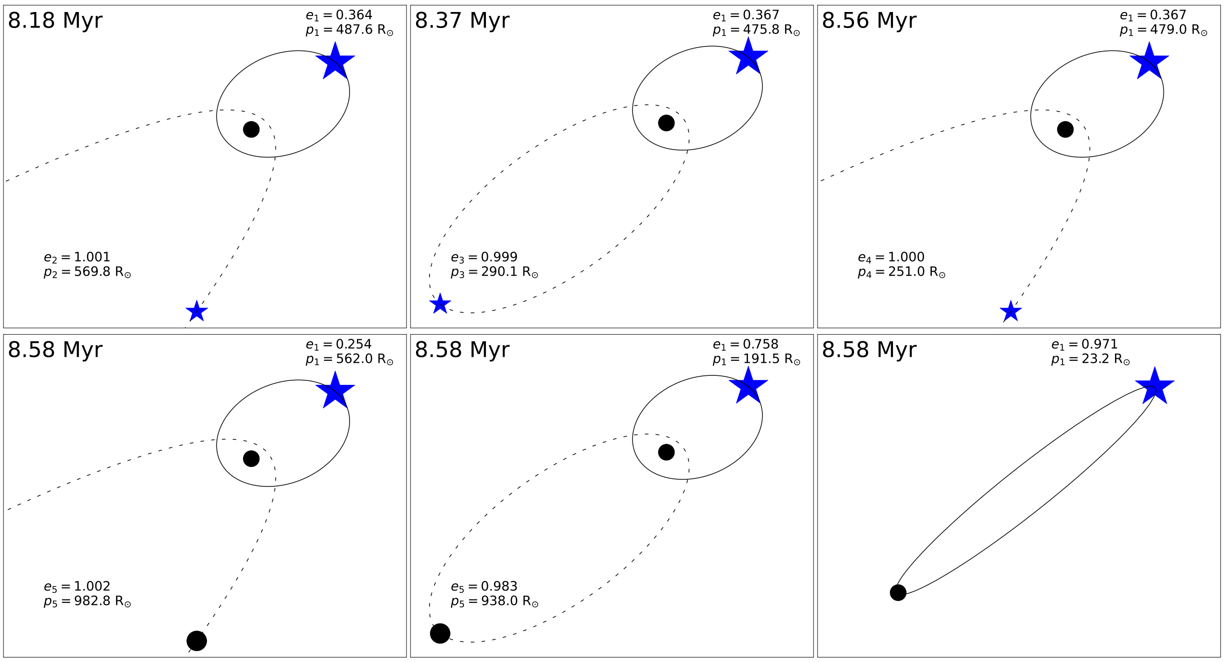

Figure 3.6: Sketch of the last five triple interactions experienced by a BH-VMS binary before the collision. In the last interactions, the BH-VMS binary forms a hierarchical triple with a stellar BH. Consequently the binary increases its eccentricity to a value close to unity that leads the BH to merge with the VMS.

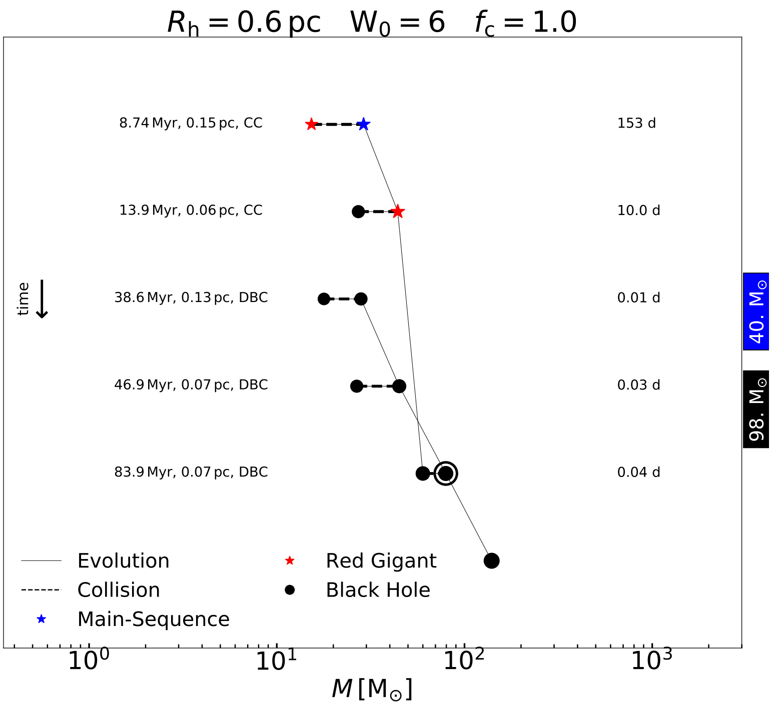

Figure 3.7: Formation and evolution of an IMBH in a simulation with $W_0 = 6$, $R_h = 0.6\,\mathrm{pc}$ and $f_c = 0.1$, similar to Fig. 3.4. However, here the black hole reaches a mass of about $140\,\mathrm{M}_\odot$ mostly through collisions (horizontal dashed lines) with other BHs. This is the only case, out of 80 simulations analysed, where a BH above 100 $\mathrm{M}_\odot$ built up its mass mostly through collisions with other BHs.

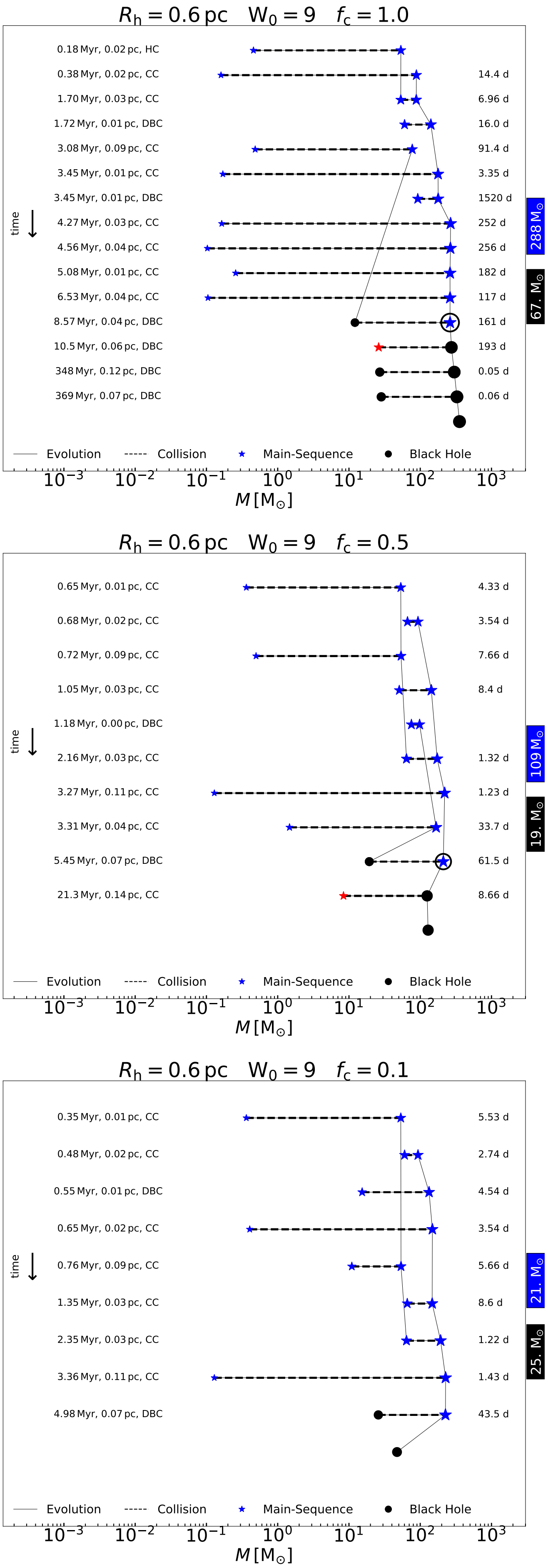

Figure 3.8: Comparison of three models with identical initial conditions and decreasing f_c of 1, 0.5, and 0.1 from top to bottom. For f_c =0.1 no IMBH forms. The time of IMBH formation is indicated by a black circle in the two top panels. Here we show a different realization of model R06W9 than in Fig. 3.4.

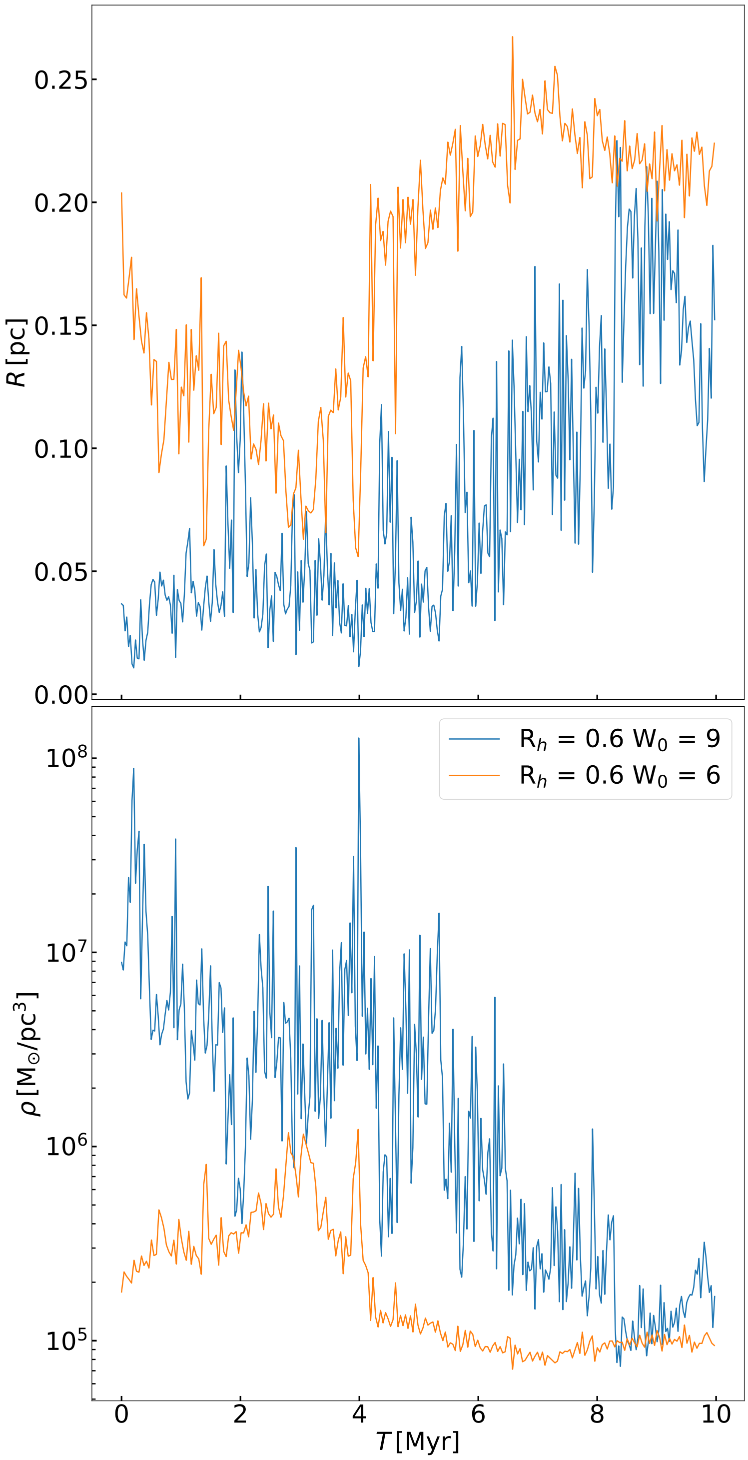

Figure 3.9: Time evolution of core radius (top panel) and core density (bottom panel) for two models with the same initial size $R_{\rm h}$ = 0.6 pc but different initial central potential parameter W_0 (blue: R06W9, orange: R06W6). The figure shows a constant rapid expansion for the R06W9 model as opposed to an initial contraction for R06W6 simulation. The initial central density difference in the two models decreases in the first few Myr.

The absence of relativistic recoil velocity does not influence the series of collisions and interactions that lead to the VMS-BH mergers. The BHs involved in these collisions are the remnant of massive stars and they did not merge with any other BH. This can be clearly seen from fig. 3.4 and fig. 3.8. Both figures report all the collisions experienced by each object that participates in the collision chain. Therefore if a BH appears in the plot only once it implies that the object never experiences any collision before.

The IMBHs in our simulations are mainly growing through two channels:

- Accretion of stellar material through binary collisions with stars and, to a lesser extent, through hyperbolic collisions with stars.

- Collision with low mass BHs.

BHs can also become more massive through multiple mass transfer events that do not lead to coalescence. However, the mass absorbed in those events is negligible. Moreover, BHs could also grow through tidal captures. However, according to our simulations, tidal captures do not seem to be relevant for the IMBHs final mass. Tidal captures are very rare (10-15 events per run) and only a small fractions of these events lead to collisions.

Collisions with stellar BHs typically add little ($\sim 10 - 30\%$, see Tab. 3.1) to the total IMBH mass. BH-BH collisions are not very likely to occur. This type of binary requires very small semi-major axes, or very high eccentricities to enter in the post-Newtonian regime, experience gravitational wave energy loss, and eventually merge. This requires the BH binary to undergo several strong triple interactions (or binary-binary interactions). For this reason, as we can see in Fig. 3.4, and later also in Fig. 3.8, that most of the material accreted onto a massive BH originates from stars. We form in total 17 BHs with a masses above 100 $M_{\odot}$ (see Tab. 3.1). Despite being unlikely, one of the IMBHs grows its mass almost entirely by swallowing other black holes (as shown in Fig. 3.7). The formation process occurred in about ~ 90 Myr and it involves a chain of low mass BH mergers with masses of $17 : 28, 25 : 45, 68 : 70$ $M_{\odot}$. This mechanism is particularly interesting because it provides a straightforward explanation of GW190521, the last LIGO/VIRGO detection (Abbott et al., 2020). The GW190521 gravitational signal is produced by the merger of two black holes around 66 and 85 $M_{\odot}$. Both masses might fall in the predicted pulsation pair-instability "mass gap" (Woosley, 2017). Our simulation indicates that collisions triggered by dynamical interactions can lead to the formation of black holes in this mass gap in agreement with (Kremer et al., 2020).

According to Fig. 3.3 the less concentrated model R06W6 and the more dense model R06W9 have comparable probability to produce IMBHs and VMSs despite the marked difference in the initial central density. Fig. 3.9 displays the time evolution of the core radius (plot on the top) and the core density (plot on the button) for two simulations with $W_0 = 9$ and $W_0 = 6$. The two systems experience different initial evolution: the core of the cluster with higher central density expand from the beginning of the simulation due to primordial binaries interactions, contrarily clusters with $W_0 = 6$ undergo core collapse. (this is also confirmed by the evolution of the Lagrangian radii shown in Fig. 3.12). Consequently, the initial concentration discrepancy between the two models rapidly decreases. This fact might explain why clusters with $W_0 = 6$ and $W_0 = 9$ lead to comparable results although the initial central densities of the two models differ of more then two orders of magnitude.

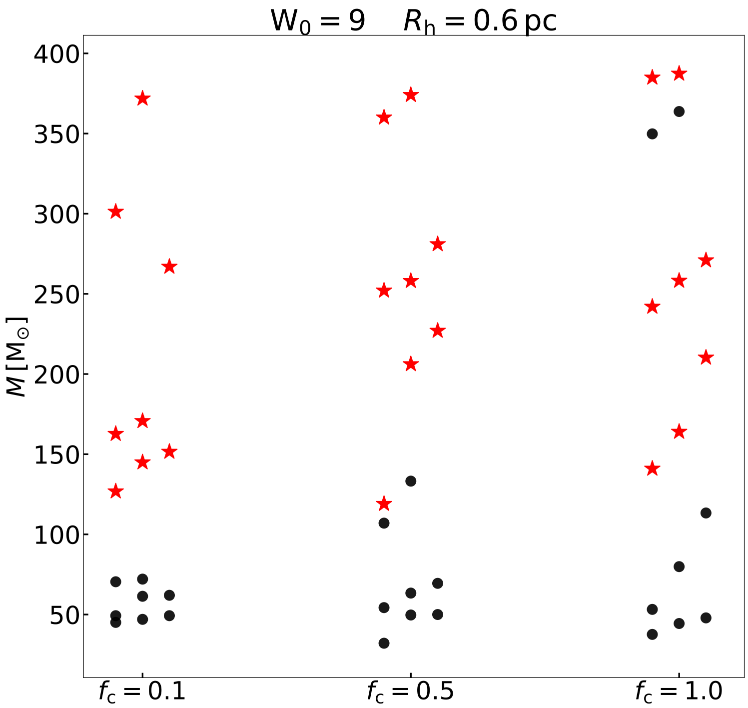

Figure 3.10: Comparison between R06W9, R06W9F05, and R06W9F01. Each black circle (red star) shows the mass of the most massive BH (MS star) formed in a single simulation.

3.5.2 Collision Fractions Comparison

So far we have assumed an accretion fraction of f_c=1 i.e. in star - BH collisions all stellar material is accreted onto the BH. Under these circumstances IMBHs regularly form in the simulations. However, the accretion fraction is highly uncertain (see section 3.3.3 for more details). Therefore, we have simulated R06W9 with lower fractions of f_c=0.5 and f_c=0.1. The results indicate that the accretion fraction can significantly change IMBH growth (see Fig. 3.10). In fact, while the stars still grow in mass by collisions, no IMBH is formed in the simulation with $f_c = 0.1$ (R06W9F01, the most massive BH has a mass of about 60 $M_\odot$). Even for simulations with $f_c = 0.5$ just two (out of 8 simulations) IMBHs form with masses only slightly above a hundred solar masses. Apart from the obvious effect that the BHs grow less in a collision with a VMS, there are also secondary effects. Less massive BHs have a higher probability to escape from the cluster after strong interactions and they have lower probabilities of experiencing additional collisions due to lower gravitational cross-sections decreasing the probability to experience close encounters.

Secondly, BH-VMS collisions with lower accretion fractions result in instantaneous mass removal from the inner part of the cluster [10] leading to cluster expansion, lower densities, and a lower merger rate. As we can see in Fig. 3.11, this effect is particularly enhanced in $f_c = 0.1$ simulations because in this case when a star collide with a BH 90% of the mass of the star is instantly ejected from the cluster.

Secondly, BH-VMS collisions with lower accretion fractions result in instantaneous mass

[10] In all our simulations BH-VMS collisions occur in the central region of the cluster.

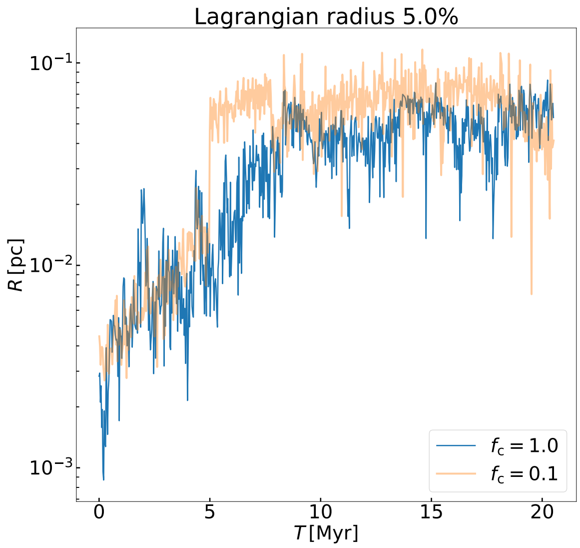

Figure 3.11: Comparison between 5% Lagrangian radii (see subsection 3.5.3 for the definition of Lagrangian radii) for a simulation with $f_c = 1.0$ (blue) and a simulation with $f_c = 0.1$ (orange). Observing the orange line we can notice a fast expansion at about 5 Myr triggered by mass-loss. This dilatation is generated by a BH-VMS collision event that occurred at 4.98 Myr. During the collision 90 % of the total mass of the VMS is assumed to be ejected instantly from the cluster. For simulations with $f_c = 1.0$, these type of expansions do not occur because the mass of stars is fully retained in the cluster when BH-star collisions occur.

removal from the inner part of the cluster [11] leading to cluster expansion, lower densities, and a lower merger rate. As we can see in Fig. 3.11, this effect is particularly enhanced in $f_c = 0.1$ simulations because in this case when a star collide with a BH 90% of the mass of the star is instantly ejected from the cluster.

3.5.3 Cluster Evolution

In this section, we highlight the evolution of three different simulations resulting in very different peak BH masses, which we label, for simplicity, with S_1, S_2 and S_3. S_1 and S_2 are two different realizations of the model R06W6. The latter creates an IMBH of 140 $M_\odot$ (the evolution path of this BH is shown in Fig. 3.7). The most massive BH in S_1 only reaches 60 $M_\odot$. S_3 is one realization of the model R06W9 generating an IMBH, with a mass of about 350 $M_\odot$ (see evolution path in Fig. 3.4). The left, center and right panels in Fig. 3.12 refer to S_1, S_2 and S_3. respectively. Each panel consist of three plots. The plots at the top display the time evolution of the radii enclosing 3%, 5%, 10%, 30%, 50% and 70% of the cumulative stellar mass (Lagrangian radii). The middle plots illustrate the evolution of the average stellar mass within 3%, 5%, 10% and 30% Lagrangian radii. The plots at the bottom show the mass (and the type) of the most massive object in each cluster as a function of time and its distance from the cluster center.

The evaluation of these three systems highlights the complex interplay between stellar evolution and dynamical interactions. The former has a strong impact on the early phase, while the latter plays a major role in driving the long-term change. Stellar evolution mass loss triggers a strong expansion on early cluster evolution (Applegate, 1986; Chernoff & Shapiro, 1987; Chernoff & Weinberg, 1990; Fukushige & Heggie, 1995) Our simulations confirm these results. The 30%, 50%, 70% Lagrangian radii indicate a strong monotonic cluster inflation in the first ~ 10 Myr as a consequence of mass loss due to supernovae explosion and stellar winds followed by

[11] In all our simulations BH-VMS collisions occur in the central region of the cluster.

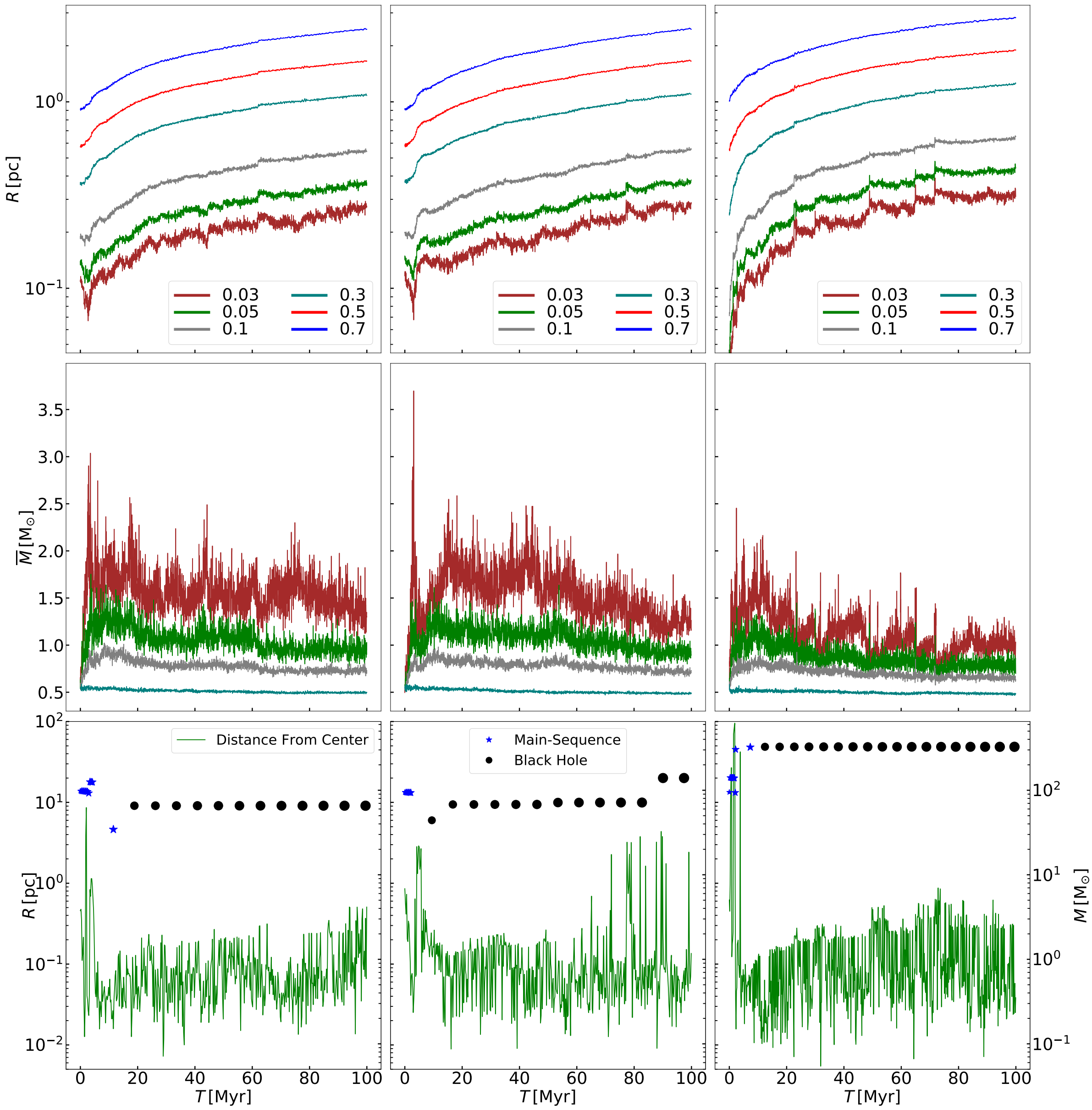

Figure 3.12: Lagrangian radii evolution (upper plots), particle mass average evolution (central plots), distance and mass of the most massive object (button plots). The left central and right panels report the results of three different simulations. The simulation on the left is a realization of the R06W6 model that does not form IMBHs (the most massive BH has a mass of 60 M$_\odot$). The central panel refers to another realization of the R06W6 model that generated an IMBH of 140 M$_\odot$ through a chain of BH-BH collisions. The plots on the right report the outcome of a R06W9 realization where an IMBH of about 350 M$_\odot$ formed in a VMS-BH collision.

a moderate expansion driven by primordial binaries and further mass loss due to stellar/binary evolution.

Since our three simulations are multi-mass systems they undergo mass segregation in about ~ 1.4 Myr (see table 3.1). As a consequence of that, the average stellar mass in the inner part of the three clusters strongly increases in the first ~ 2 Myr (middle panels of Fig. 3.12). S_1 and S_2 also register an initial core collapse connected with mass segregation (rapid decrease for 3%, 5%, and 10% Lagrangian radii) in agreement with previous numerical work (Portegies Zwart & McMillan, 2002; Portegies Zwart et al., 2004; Gürkan et al., 2004; McMillan, 2008). On the other hand, S_3 does not show any indication of core collapse. The system is already so dense that binary interactions prevent the collapse and force the core to expand (the innermost Lagrangian radii are in constant expansion since the beginning of the simulation. See top-right plot of Fig. 3.12).

Subsequently, the death of the most massive stars leads to a mass average drop in the inner part of the cluster for both $S_1$and S_2 (see red line in central plots). The average mass then continues to oscillate, but while in S_1 it presents a steady decline, S_2 raises again due to a BH-BH merger after about 15 Myr. After that, it declines at a constant rate due to stellar evolution mass loss. The initial drop is less evident in S_3 also because the presence in the center of the IMBH[12] compensates for the absence of the massive stars.

Massive objects located in the core of the cluster experience frequent strong interactions. This effect is reflected in the strong oscillations of the mass average in the core (see central plots) as well as the strong variations in the position of the IMBHs (see green lines in the button plots). In S_3 the IMBH oscillates in position between 0.01 and 0.5 pc with an average position of about 0.1 pc. Similarly the BH in S_1 moves around 0.1 pc with slighter stronger oscillations due to its lower mass. On the other hand, the BH in S_2 experiences strong radial change few millions years before its coalescence with an other BH at 84 Myr. These heavy oscillations are generated by the strong interactions that triggered the last BH-BH collision.

3.5.4 Comparison with Observations

Very massive stars, formed through collisions between lower mass stars, appear in almost all the realizations of our ten models. If the VMSs formation mechanism proposed in this and other works (Portegies Zwart & McMillan, 2002; Portegies Zwart et al., 2004; Gürkan et al., 2004; Mapelli, 2016; DiCarlo et al., 2020; Wang et al., 2020) is correct they might be observed inside or close to dense star clusters. Early studies of the Arches cluster indicated an upper star mass limit of 150 $M_\odot$ Figer (2005). However, more recent observations indicate the existence of stars greatly exceeding this limit, suggesting the presence of VMSs up to 300 $M_\odot$ in the vicinity of young massive star clusters (Crowther et al., 2010). Another study claimed the discovery of a VMS of initial mass in the range between $90 - 250$ $M_\odot$ in the central cluster of the region W49 (Wu et al., 2014). These stars might be generated via runaway collisions as indicated by the outcome of our and previous studied discussed in section 3.6. However, gas accretion could be an equally valid mechanism for the formation of VMSs (Krumholz, 2015).

[12]In S_3 the IMBH form very fast, at about 8 Myr. On the other hand, the IMBH in S_2 is generated after 84 Myr.

It has been shown that the massive BH that power the hyper-luminous source associated with MGG-11 might have a dynamical origin. The high density and compactness of this cluster allow for the formation of a few thousand solar masses star via collisional runaway, which might directly collapse into an IMBH (Portegies Zwart et al., 2004). Also, our results suggest that IMBHs could be the origin of HLXs associated with dense star clusters. It is not rare for our simulated IMBHs to accrete mass and merge with stars, as shown in the top and central plots of Fig. 3.8 (both plots show the IMBH merging with a red giant at 10 and 21 Myr). However, even if our results show that IMBHs do receive mass from other stars, the mass transfer events are very often interrupted by strong interactions and therefore they do not last more than 1 Myr. In other words the IMBHs tend to spend only a small fraction of their time accreting material from their companion. This, in addition with the fact that IMBHs have a non negligible probability to be ejected from the cluster after a BH-IMBH collision (Arca-Sedda et al., 2020; Mapelli et al., 2020), might explain the absence of IMBHs accretion signature in may star clusters and most of globular clusters (Wrobel et al., 2015; Wrobel & Nyland, 2020).

Our simulations reveal that IMBHs, right after formation, tend to bind with a low mass black hole in a BH-BH binary. The binary, located a the center of the cluster, experiences constant gravitational interaction with other objects, and it merges in an interval of time between $\sim 10-100$ Myr generating gravitational wave signal. The results also show that hierarchical black hole mergers [13], could be observed in dense stellar systems, as shown in fig. 3.7 and3.8 (top panel), however as pointed out in recent studies (Mapelli et al., 2020; Arca-Sedda et al., 2020) these events might be suppressed by the gravitational wave kicks. The latter were not included in our simulations although we expect them to generate a large recoil velocity especially if the two colliding BHs have comparable masses (**?**Baker et al., 2008; Lousto & Zlochower, 2009; Kulier et al., 2015; Morawski et al., 2018; Zivancev et al., 2020).

BH-IMBH coalescence, as well as the inspiral phase, will be detected by the next generation of gravitational wave detectors. Events that involve an IMBH with mass < 200 $M_\odot$ should be detected by LIGO while signal generated by IMBHs with masses < 2000 $M_\odot$ should be observable with the (Fragione et al., 2018; Arca-Sedda et al., 2020).

3.6 Comparison with previous work

Various groups have predicted runaway merger scenario for the formation of VMSs and IMBHs in dense stellar environments. For example, direct N-body simulations, carried out by Portegies Zwart et al. (2004), indicate the formation of a few thousand solar masses stars produced by multiple stellar mergers. The simulated star clusters, containing $128k$ stars, were evolved for 12 Myr using Starlab (Portegies Zwart et al., 2001) and NBODY4 (Aarseth, 1999). The stellar evolution prescription adopted was based on Hurley et al. (2000) for stars with masses ≤ 50 $M_\odot$ while more massive stars follow the evolution track given by Stothers & Chin (1997) and Ishii et al. (1999) . With these models stars more massive than 260 $M_\odot$ collapse directly into IMBHs without losing mass in supernova explosions.

[13]Multiple mergers of BHs that form more massive ones.

A similar mechanism is observed in the 30 simulations presented by Mapelli (2016) where VMSs reach about 500 $M_\odot$ through runaway collisions. Each of these simulations is initialized with 10^5 stars following a King density profile with $W_0 = 9$ and $R_h = 1.0$ pc . The clusters were evolved for 17 Myr using Starlab. Due to the different stellar evolution model adopted for massive stars, these simulations generate IMBHs of few hundred solar masses through direct collapse of VMSs (the VMSs at low metallicity lose a relatively small fraction of their masses).

The analysis of the 6000 simulations of lower mass clusters presented in DiCarlo et al. (2020) shows that BHs of about 300 $M_\odot$ can form through dynamical interaction and collisions. The clusters, evolved using NBODY6++GPU, adopted the MOBSE stellar evolution (Mapelli et al., 2017; Giacobbo et al., 2018). This prescription is based on Hurley et al. (2000); Hurley et al. (2002) and it includes new prescriptions for massive stars reducing the mass loss in supernovae explosion and stellar winds. The systems were initialized with an initial mass in the range between 10^3 and 3×10^4 $M_\odot$. The initial central densities and initial half-mass radii were computed as a function of the initial mass of the cluster.

Simulations evolved with Monte Carlo codes reveal similar outcomes. Freitag et al. (2006) computed over 100 models, varying the cluster size, particle number, and central concentration. They systematically changed the number of stars between 10^5 and 10^8 represented by a maximum of 9×10^6 particles. Their result show that 20 % of the clusters with an initial central potential parameter $W_0 \geq 8$ form a VMS with a mass ≥ 400 $M_\odot$. Other simulations carried out using Monte Carlo models show that multiple VMSs can form within the same cluster (Gürkan et al., 2006).

The analysis of 2000 of simulations (Leigh et al., 2013; Giersz et al., 2015), evolved using the MOCCA (MOnte Carlo Cluster simulAtor) code, reveals the formation of IMBHs in dense stellar environment (Giersz et al., 2015). The outcome of these simulations indicates that about 20% of the simulated clusters generate a BH with a mass larger than 100 $M_\odot$. These BHs have formed through collisions between a VMS and a stellar BH. The formation path is very similar to the one indicated by our N-body simulations (see Figs. 3.8 and 3.4). However, in general, the IMBHs produced in MOCCA simulations tend to be systematically slightly more massive as the runaway main-sequence star collisions lead to more massive VMSs in MOCCA than in N-body. In fact, in MOCCA simulations the stellar evolution time-step is performed at the end of the relaxation time-step (that is about 10 Myr). As a consequence of that, the masses of main-sequence stars, the mass segregation, and central density are larger in the MOCCA simulations than in N-body simulations leading to a larger interaction rate.

The analytical work carried on by Stone et al. (2017) shows how stellar mass BHs in nuclear star clusters can grow into IMBH through runaway tidal captures of low mass stars. As stated in their work, runaway tidal captures can be triggered only in massive and compact clusters with a velocity dispersions $\sigma > 40$ km/s. According to their criteria, none of our models would have made IMBHs. However, Stone et al. (2017) do not include massive stars and primordial binaries in their study, which are the key elements for the IMBH formation mechanism proposed in our work.

As we have shown in this section the debate whether and how IMBH form in dense star clusters is ongoing for at least two decades. Recent MOCCA Monte Carlo simulations have provided a wealth of data and answered the question positively. It is important to confirm MOCCA Monte

Carlo results by direct N-body models, but the latter have suffered in the past from low statistical quality, if the particle number is small (say 10^4 or less), and very demanding computing time requirements, if the particle number is large (e.g. 10^5 or more). A strategy to balance low statistical quality of small N models has been to do larger samples of models and discuss their average (Giersz & Spurzem, 1994; DiCarlo et al., 2020); but relevant astrophysical processes in star clusters (like two-body relaxation, close few body encounters, stellar evolution, tidal forces) do not scale with the same power of N. Therefore large sets of small N-body simulations can provide useful information to some degree, but can never fully substitute N-body simulations with more realistic larger particle numbers. Baumgardt (2017) present a very nice study using the method of small N samples and scaling to real star clusters; but still they are missing the effects of binaries and tidal fields, because they are difficult to scale. Our models exhibit IMBH formation in dense star clusters with an initially large particle number of more than 100k stars, 10% of which are in binaries, and all relevant astrophysics; 80 such models were done using NBODY6++GPU for at least up to 300 Myr (8 models each for 10 different initial models). To our knowledge these are so far the largest direct N-body simulations of their kind, and in light of the discussion above they provide the so far strongest evidence for IMBH formation.

3.7 Summary

We have provided evidence for the formation of intermediate mass black holes (IMBH) through collisions of massive stars, formation, and evolution of binaries including black holes. Debated for decades and recently underpinned by a large set of Monte Carlo (MOCCA) simulations our direct N-body models are the largest and longest simulations supporting this idea of IMBH formation in dense star clusters, made possible by the use of the massively parallel GPU accelerated code NBODY6++GPU and the use of suitable supercomputers in Germany and China.

We ran and analyzed 80 N-body simulations of compact young massive star clusters with different central densities (central potential parameters $W_0 = 6, 7, 8, 9, 10$) and sizes (half mass radii $R_h = 0.6, 1.0$ pc). The simulated clusters were evolved for at least 300 Myr [14]. All our models lead to the collisional formation of at least one star above 100 $M_\odot$ (the upper initial mass function limit) and several simulations create stars with masses higher than $\sim 400\ M_\odot$ within the first ~ 10 Myr of cluster evolution. Most of the collisions were triggered by triple interactions between hard binaries and single objects. With the stellar evolution model assumed for this study, isolated massive stars cannot collapse directly into IMBHs (BHs with masses $> 100\ M_\odot$). Even stars with $\sim 500\ M_\odot$ lose most of their mass through stellar winds and collapse into a BH of about 30 $M_\odot$.

However, a sizable fraction (about 20%) of our simulations result in the formation of IMBHs by means of direct collisions between stellar-mass BHs and massive stars as already observed in MOCCA simulations (Giersz et al., 2015). This process is more likely in compact clusters as they form more massive stars and it takes less time for the BHs to sink into the center. Nevertheless, if only a small fraction of the stellar mass is accreted in a collision with a BH (e.g. a collision

[14] The simulations that formed an IMBH of about 350 $M_\odot$ were evolved for 500 Myr.

fraction of $f_c = 0.1$) the above process becomes unlikely for the formation of IMBHs in compact $\sim 7 \times 10^4 M_\odot$ clusters investigated in this study. The value of f_c has been discussed in many theoretical (Shiokawa et al., 2015; Law-Smith et al., 2019; Lu & Bonnerot, 2020; Bonnerot & Lu, 2020) as well as observational studies (Wen et al., 2020). Many of these works predict f_c to be in an interval between 0.2 and 0.5. Other studies argue that $f_c \leq 0.1$ might be possible (Metzger & Stone, 2016). All these studies compute f_c in a SMBH - low mass star collision event. Our case of interest involves a stellar BH colliding with a massive star; it is still poorly studied and requires future investigation.

In one simulation the IMBH form through a series of consecutive collisions that occurred in the first ~ 90 Myr (see Fig. 3.7). This IMBH is the final product of a merger between a 68 and a 70 $M_\odot$ BH. The 68 $M_\odot$ BH form during a collision between a 28 $M_\odot$ stellar BH and a 50 $M_\odot$ red giant (during the collision the stellar BH absorbs the entire core of the star while the envelope is assumed to be lost). While two consecutive BH mergers 17 : 28, 25 : 45 $M_\odot$ lead to the formation of the 70 $M_\odot$ BH. The event registered in this simulation is particularly interesting because it provides a straightforward explanation of GW190521, the last LIGO/VIRGO detection (Abbott et al., 2020). The GW190521 gravitational signal is produced by the merger of two black holes around 66 and 85 $M_\odot$. Both masses might fall in the predicted pulsation pair-instability "mass gap" (Woosley, 2017), therefore they might not have had a simple stellar origin. Our simulation reveals a possible way of forming BHs with similar masses and illustrates which dynamical processes can lead to their collision.

After its formation, the IMBH can still grow moderately colliding with other low mass BHs. Here it is important to mention that kicks from gravitational radiation consequent to BH-BH mergers have not been implemented in our code. As a consequence of that, we might have slightly overestimated the probability for the clusters to retain the IMBH. However, in many cases the mass ratio involved in IMBH-BH collisions is very small ($\frac{m_{BH}}{M_{IMBH}} \approx \frac{20}{300} \approx 0.067$), consequently the recoil velocity should not exceed the escape velocity (**?**Baker et al., 2008; Lousto & Zlochower, 2009; Kulier et al., 2015; Morawski et al., 2018; Zivancev et al., 2020).

During the growth process of all simulations with IMBHs, with one exception shown in Fig. 3.7, there are no BH - BH mergers[15] before the formation of the IMBH in a VMS - stellar BH collision. Therefore the inclusion of relativistic kicks will not change this result. After the IMBH has formed it occasionally collides with a stellar mass BH in an intermediate mass-ratio inspiral (IMRIs) event, which has the potential to kick the IMBH out of the cluster. If common, such a process might explain the missing observational evidence for IMBHs in present day globular clusters. IMBHs might have formed in many GCs early on and, once lost, float around in the galaxies.

Adding gravitational wave kicks and spins will be possible in the future using the approximate models of Baker et al. (2008) for the kick velocity (magnitude and direction) and a new model of how initial BH spins depend on mass and metallicity by Belczynski et al. (2017). Morawski et al. (2018) have analyzed large samples of BH mergers from MOCCA simulations, and show that the

[15] In general, BH-BH collisions events are rare. This type of binaries must undergo several strong close interactions to enter the post-Newtonian regime where gravitational radiations can lead to a rapid coalescence. Because of these interactions, the binary is often ejected from the cluster before the merger occurs.

BH retention fraction in the cluster varies between 20% and 100% depending on evolutionary time and parameters of the cluster. Brem et al. (2013) have included full Post-Newtonian dynamics in their N-body simulation and reproduced results of Rezzolla et al. (2008), who fitted fully relativistic models. This could also be used to derive recoil velocities, in the way done by Gerosa et al. (2018), the latter again using fully relativistic modeling.

Our results show that the models R06W6 and R06W9, despite the difference in the initial central density, have a comparable probability to form an IMBH. The different evolution of the inner part of the clusters in these two models seems to mitigate the impact of the initial central density on the probability to form an IMBH: in very concentrated systems, the high central density forces the clusters to expand because of early energy generation by primordial binaries; on the other hand, less dense clusters undergo core collapse. Therefore, already at the very beginning of the simulation, the initial difference in central concentration between the models is reduced.

Our results indicate that compact star clusters can rapidly generate an IMBH of few hundred solar masses in about 5 − 15 Myr. Assuming the scenario that nuclear star clusters are generated by globular clusters that spiral toward the nucleus (Tremaine et al., 1975), the IMBHs, if present in the clusters, can further grow in mass colliding with each other and swallowing smaller objects in the center of the nuclear cluster (Arca-Sedda & Gualandris, 2018; Arca-Sedda & Capuzzo-Dolcetta, 2019; Askar et al., 2020) leading to the formation of a SMBH. This scenario is investigated by Stone et al. (2017) adopting an analytical approach. They show how low mass BHs located in dense nuclear star cluster could rapidly grow in mass via runaway tidal captures, transforming the cluster into a SMBH.

With order 10^5 particles our models are currently the best available (in the sense of modeling all processes directly for the simulated particle number, without any scaling or averaging). However, young massive clusters in our galaxy and massive extragalactic clusters (also: nuclear star clusters) can be much more massive with particle numbers of up to 10^8 or more. NBODY6++GPU has been used for the million-body DRAGON simulations (Wang et al., 2015, 2016) and for million body simulation of a nuclear star cluster (Panamarev et al., 2019). But in the first case, the central density was much lower than in this work, so the DRAGON simulations are not prone to IMBH formation, and in the second case still, some scaling had to be used, because 10^6 particles are not enough to model nuclear star clusters. In the next ongoing studies, we are running dense star cluster models with a million bodies, and more in the future. It is feasible because only a shorter simulation time is needed (a few hundred Myr versus 12 Gyr for DRAGON). This will help us to get a better understanding of the statistics of the presence of IMBHs, not only in our Galaxy but also out to distant regions relevant for LIGO/Virgo and space-based gravitational wave detections.

The version of the code used to evolve our clusters is not based on the most updated stellar evolution recipes. Our treatment does include PISN and PPISN. Moreover, according to the adopted stellar winds prescription massive stars lose a large fraction of their initial mass. On the contrary, modern stellar winds theory (Vink et al., 2000; Gräfener & Hamann, 2008; Vink et al., 2011; Sander & Vink, 2020) predicts low metallicity massive stars to retain most of their masses. The most updated version of NBODY6++GPU (partly inspired by LIGO data) contains some recent stellar evolution updates[16] that include pulsation pair-instability and new treatments for stellar

[16]These updates were made after the completion of the simulations presented in this work.

winds (see Belczynski et al., 2008; Banerjee et al., 2019; Banerjee, 2020, for more information). this new version of the code is used for our ongoing simulations. We expect that results based on new stellar evolution prescription to be in reasonable agreement with the outcome of this work (see section 3.5.1); none of these new effects should prevent the dynamical formation mechanism of IMBHs discovered in our work; they might however modify the dynamical path that leads to the creation of IMBHs. Therefore future numerical and quantitative studies in this direction are needed. In future models we also plan to improve the modeling of the external tidal forces on the cluster, reflecting its true orbit around the host galaxy.

Chapter 4

Black hole mergers in compact star clusters and massive black hole formation beyond the mass-gap

The content of this chapter is based on the submitted paper Rizzuto et al. (2021a).

4.1 Abstract

We present direct N-body simulations, carried out with NBODY6++GPU, of young and compact low metallicity star clusters with 1.1×10^5 stars, a velocity dispersion of $\sim 10\,\mathrm{km/s}^{-1}$, a half mass radius $R_h = 0.6$ pc, and a binary fraction of 10% including updated evolution models for stellar winds and pair-instability supernovae (PISNe). Within the first tens of megayears of evolution, each cluster hosts several black hole (BH) merger events which nearly cover the complete mass range of primary and secondary BH masses for current LIGO/Virgo/Kagra gravitational wave detections. The importance of gravitational recoil is estimated statistically. We present several possible formation paths of massive BHs above the assumed lower PISNe mass-gap limit ($45M_\odot$) into the intermediate-mass BH (IMBH) regime ($> 100M_\odot$) which include collisions of stars and BHs as well as the direct collapse of stellar merger remnants with low mass cores. The stellar evolution updates result in the early formation of higher mass stellar BHs than for the previous model. The resulting higher collision rates with massive stars support the rapid formation of massive BHs. For models assuming a high accretion efficiency for star-BH mergers, we present a first-generation formation scenario for GW190521-like events – a merger of two BHs in the PISN mass-gap – which is dominated by star-BH mergers. This IMBH formation path is independent of gravitational recoil and therefore conceivable in dense stellar systems with low escape velocities. One simulated cluster even forms an IMBH binary ($153M_\odot$,$173M_\odot$) which is expected to merge within a Hubble time.

4.2 Introduction

Before the first LIGO gravitational-wave (GW) detection, many theoretical models of stellar evolution predicted stellar black holes (BHs) masses to be lower than 30 $M_\odot$. These models remained unchallenged for several years because all stellar BHs observed at the time had masses $\lesssim$ 20 $M_\odot$ (Ziółkowski, 2008; Özel et al., 2010). Surprisingly, the first LIGO detection, GW150914, revealed components more massive than 30 $M_\odot$ (Abbott et al., 2016). Such masses had been predicted by stellar evolution models at low metallicity introducing a dependence between stellar winds mass loss and metallicity (see Woosley et al., 2002; Vink et al., 2001, and references therein). This highlights the importance of stellar evolution models for the correct interpretation/prediction of GW events. An accurate theory for the evolution of massive stars is particularly important to predict the mass distribution of stellar BHs at their formation. For this, precise models of stellar winds and a correct description of the last stages of the stellar evolution before the collapse are required. At the onset of stellar collapse, stars with sufficiently large helium cores undergo a phase of electron-positron pair production that in turn leads to one or more violent explosions. Depending on the initial mass of the core, the star can experience pulsation pair-instability supernovae (PPSN) getting partially destroyed or it can experience the more violent pair-instability supernovae (PSN) and is destroyed completely (Fowler & Hoyle, 1964; Woosley et al., 2007; Woosley, 2017). Due to (P)PSN, isolated massive stars are not supposed to collapse into BHs in the mass range of approximately 50 – 130 $M_\odot$. This gap in the stellar BH mass distribution is known as the (P)PSN mass gap. The mass limits of this gap are affected by various uncertainties and therefore they depend on the details of the stellar evolution adopted. In this study, the assumed mass gap is 45 – 195 $M_\odot$.

The 66 - 85 $M_\odot$ BH merger (GW190521) detected by the LIGO/Virgo/Kagra collaboration (**?**) has started a debate about the origin of the two objects involved in the collision as both of BHs fall in the (P)PSN mass gap. In particular, the mass of the primary in GW190521 (85 $M_\odot$) poses a challenge to theoretical models. In a recent paper, Vink et al. (2021) has proposed a modified stellar evolution model such that $\sim$ 100 $M_\odot$ stars lose only little mass via stellar winds, small enough for the stars to collapse into BHs in the range of $\sim$ 85 $M_\odot$. A recent study, leveraging newly estimated uncertainties on (P)PSN mass loss, affirm that GW190521 could have formed through the classical isolated binary evolution (Belczynski, 2020). Other potential formation channels for BHs of such masses might involve population III stars (Liu & Bromm, 2020; Kinugawa et al., 2021) or might depends on details of the rates of carbon-oxygen nuclear reactions (Farmer et al., 2019).

As both observed merging BHs in question are above the conventional mass gap lower limit of $\sim$ 50 $M_\odot$ (Farmer et al., 2019; Woosley et al., 2020), and because there is evidence for residual eccentricity (Romero-Shaw et al., 2020; Gayathri et al., 2020) and/or spin precession (**?**), many authors have argued that GW190521 could have been produced dynamically through repeated mergers of smaller BHs (**?**). The most popular models involve multiple mergers of low mass BHs in dense and massive stellar environments with an escape velocity of a few hundred km/s (Arca Sedda & Benacquista, 2019; Fragione et al., 2020; Romero-Shaw et al., 2020; Kimball et al., 2020; Dall'Amico et al., 2021; Mapelli et al., 2021). According to these studies, young star clusters and globular clusters are less favoured because the recoil kick imparted to the merger

Model Name	r_c [pc]	ρ_c [$M_\odot$ / pc ^{3}]	R_h [pc]	σ [km/s]	t_{rh} [Myr]	t_s [Myr]	f_c	IMBH	M_{IMBH} [$M_\odot$]	t_{form} [Myr]
R06W61.0	0.19	1.1×10^5	0.6	15	56	1.4	1.0	6/8	102, 108, 153, 156, 172, 293	76, 3.9, 29, 21, 6.9, 44
R06W60.5	0.19	1.1×10^5	0.6	15	56	1.4	0.5	4/8	98, 99, 109, 113	34, 12, 6.5, 4.3

Table 4.1: Model parameters of the cluster simulations: r_c : initial core radius; ρ_c : initial central density; W_0 : central potential parameter for the King density profile (King, 1966); R_h : half mass radius; σ : dispersion velocity; t_{rh}: half mass relaxation time; t_s: segregation time scale for 100 $M_\odot$; f_c : fraction of mass absorbed by a compact object during a direct collision with a star; # IMBH : Number of BHs with masses $\gtrsim$ 100 $M_\odot$ formed out of 8 realisations; M_{IMBH}: IMBH masses; t_{form} : IMBHs formation times.

remnant could eject the final product of a BH - BH merger and halt its mass growth too early.

However, many of these studies might have underestimated the importance of star - BHs collisions for the formation of GW events mass range of GW190521. In agreement with previous studies (Giersz et al., 2015; Di Carlo et al., 2019; Kremer et al., 2020; Becker et al., 2020; Rizzuto et al., 2021b; Arca Sedda et al., 2021), the star cluster simulations we present in this chapter show that low mass BHs can reach the (P)PSN mass gap or even the IMBH mass range through stellar mergers. A similar outcome could be produced invoking tidal capture events (Stone et al., 2017). Moreover, they illustrate that GW190521-like events could be hosted by $\sim 10^5$ $M_\odot$ compact star clusters if the BHs involved in the collisions also grow by the accretion of stellar material.

This work is an extension of Rizzuto et al. (2021b) where we have shown that a few hundred solar masses IMBHs can form in low metallicity compact star cluster environments via multiple collisions[1]. We use updated stellar evolution models with pulsation pair instability prescriptions and new stellar winds recipes (following Banerjee, 2020) to evolve the most promising initial conditions presented in Rizzuto et al. (2021b). We describe the details of the stellar evolution models in the next section (Section 2) and present the initial conditions in Section 3. In Section 4 we discuss our results in comparison to our previous work. In the final section, we discuss and summarise the main results.

4.3 The Method

We present 16 new simulations of compact star clusters adopting the same initial conditions as in Rizzuto et al. (2021b) using updated the stellar evolution models in the NBODY6++GPU (Wang et al., 2015) code. NBODY6++GPU is capable of evolving star clusters with a realistic number of stars following the dynamical evolution of the system accurately as well as the stellar evolution of single and binary stars (see also **?**). The integrator follows the dynamical evolution of binary stars, even in phases of mass loss or when one of the two stars experiences a supernova explosion. In this case, the new trajectories of the remnant and its companion are computed accurately. (for more details see e.g. Rizzuto et al., 2021b, and references therein). In extension to Rizzuto

[1]As pointed out by Mark Gieles in private communication, the process that leads to the formation of massive objects in our simulation is not a runaway growth because the growth rate does not increase with growing mass.

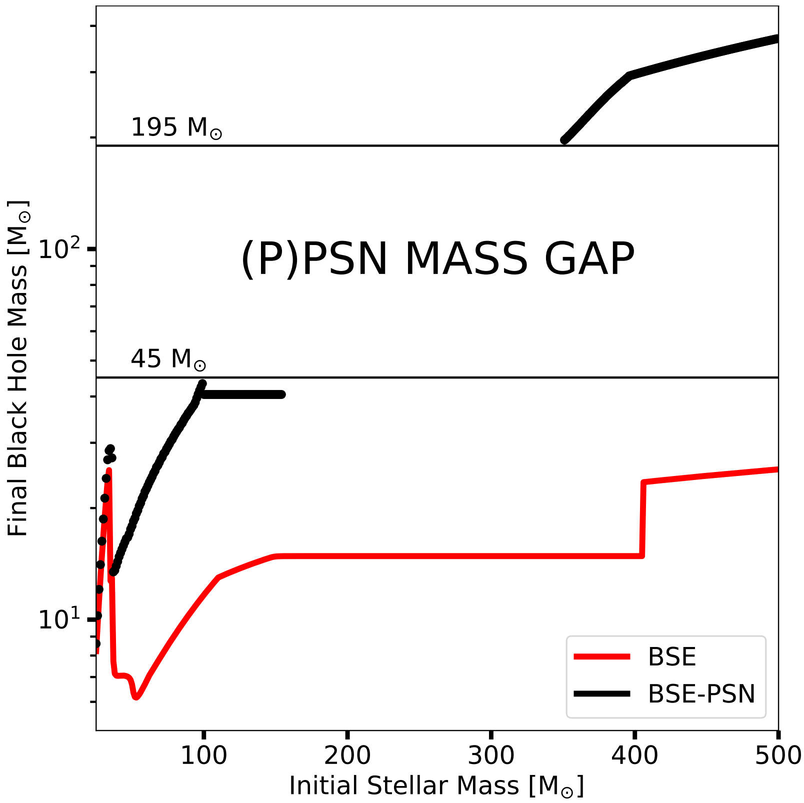

Figure 4.1: The final black hole mass as a function of initial stellar mass for stellar evolution model BSE (red) used in Rizzuto et al. (2021b) and the new model BSE-PSN (black) used here with updated stellar wind and pair instability supernova models. This is for single stars in isolation at metallicity $Z = 0.0002$. For BSE-PSN the mass gap with with no stellar mass black hole remnant ranges from 45 M$_\odot$ to 195 M$_\odot$.

et al. (2021b), the stellar evolution models of NBODY6++GPU have been significantly updated and improved (see Kamlah et al., 2021, for more details). Most of the updates have been published for NBODY7 already in Banerjee (2020). The major updates are:

1. New stellar wind models following Belczynski et al. (2010). which in turn follow the wind mass-loss rates given by Vink et al. (2001). With these models, BHs masses that originate from single stars depend strongly on the metallicity. For instance, a 100 M$_\odot$ isolated main-sequence star would leave a 15 M$_\odot$ BH at solar metallicity ($Z = 0.02$). At very low metallicity ($Z = 0.0002$), however, it can form a BH of about 60 M$_\odot$, in the absence of pair-instability models.

2. Pair-instability supernova and pulsation pair-instability supernova models (according to Belczynski et al., 2016) incorporated in the remnant formation and supernovae models as described in Fryer et al. (2012). Stars with helium core with masses > 40 M$_\odot$ undergo a violent phase of mass loss. For helium cores in the range between 60 – 135 M$_\odot$ the star is completely destroyed.

3. New prescription of BHs and NSs natal kick velocities that explicitly depend on the fallback fraction (Banerjee, 2020).

4. A model for electron capture supernovae (ECSN) following Podsiadlowski et al. (2004) and Gessner & Janka (2018) that produces neutron stars with low-velocity kicks that are therefore likely retained in medium-size star clusters.

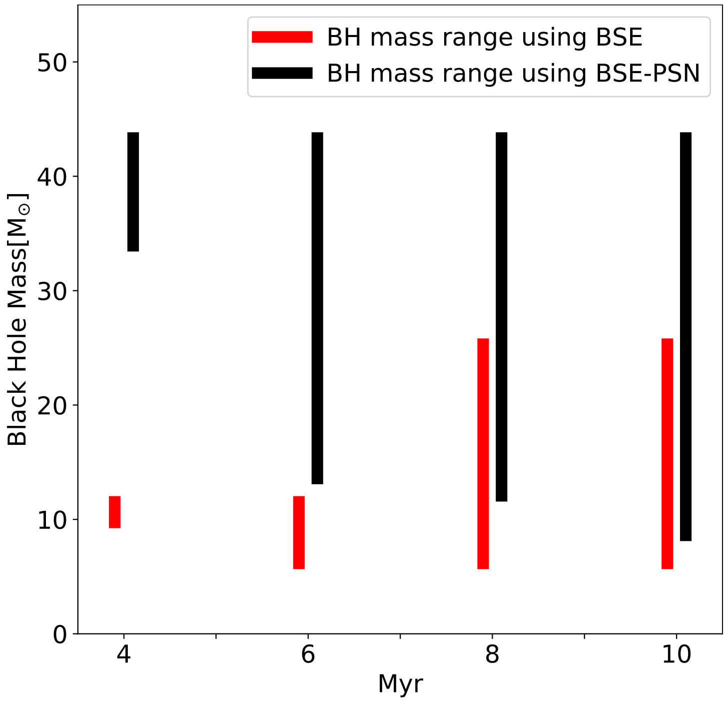

Figure 4.2: The plot shows in black (red) the BH mass range, at different times, produced by evolving heavy stars of 25 – 100 M$_\odot$ in isolation using BSE-PSN (BSE). While BSE-PSN produces BHs of ~ 40 M$_\odot$, already after 4 Myr, BSE starts to generate more massive BHs only after 6 Myr. Therefore, in the BSE-PSN (contrary to BSE) simulations, 40 M$_\odot$ BHs can coexist with massive stars of ~ 50−70 M$_\odot$. The BHs have a higher probability to collide with more massive stars and grow more rapidly in mass.

The gravitational energy loss and resulting merger of compact objects is computed following **?** and the implementation is presented in Rizzuto et al. (2021b). An important physical process that is not yet implemented in the code is relativistic recoil for compact object collisions. As we will see in the next sections, its absence might artificially enhance the probability of forming massive BHs (see Banerjee, 2021, for more details on relativistic recoil implementation in NBODY7).

Hereafter, We use the term BSE to refer to the previous stellar evolution prescription (Rizzuto et al., 2021b) while for the updated recipes we use the term BSE-PSN. The updates in BSE-PSN have a strong impact on the mass distribution of the stars and their remnants in our simulations. With BSE, an isolated massive star at metallicity $Z = 0.0002$, even as massive as 500 M$_\odot$, can never collapse into stellar-mass BH more massive than 30 M$_\odot$, as shown in Fig. 4.1 (red line). At the same metallicity, the updated model BSE-PSN with new stellar wind and the (P)PSN models, results in more massive stellar BHs. Main-sequence stars with masses in the range 80 – 100 M$_\odot$ leave a remnant of about 40 M$_\odot$ and very massive stars with masses of a few ~ 10^2 M$_\odot$ collapse directly into IMBHs, as illustrated by the black dots in Fig. 4.1. The mass-gap, without any remnant black holes, is thus limited to 45 – 195 M$_\odot$ (Fig. 4.1) in our models.

The new stellar evolution model also affects the BH formation time. The black bars in Fig. 4.2 indicate the stellar BH mass ranges as a function of time. To estimate these mass ranges we evolved massive stars in isolation with BSE-PSN setting $Z = 0.0002$. Already after 4 Myr BHs with 35 – 45 M$_\odot$ form as remnants of the most massive stars ($\gtrsim$ 80 M$_\odot$). Lighter stars explode later, pushing the lower BH mass limit down to ~ 9 M$_\odot$ after 10 Myr. On the contrary, with the BSE prescriptions, heavy stars in the range between 80 M$_\odot$ and 100 M$_\odot$ lose ~ 90% of their mass leading to early BHs with much lower masses of ~ 9 – 12 M$_\odot$. With time the upper mass limit increases only to ~ 25 M$_\odot$ (red bars in Fig. 4.2). As we will see in Section 4.5, this difference between the old and the new stellar evolution models impacts the overall formation path of massive BHs: in the BSE-PSN simulations, stellar BHs above 35 $M_{\odot}$ appear in the system when $\sim$ 70 $M_{\odot}$ stars are still alive. Therefore they have a higher probability to increase their mass by accretion of stellar material through close stellar interactions.

There are also updates concerning the neutron star (NS) modelling. While in BSE almost all NSs were ejected from the cluster due to the high natal kick velocities, in BSE-PSN the lower velocity kicks associated with ECSNe enable the formation of a NS population after 10 Myr. However, for the short cluster evolution times considered in this study, none of our models shows any NS-NS or NS-BH merger.

Tidal capture events might play an important role in the growth of massive BHs. A recent analytical model, Stone et al. (2017) show that if every tidal capture event of a BH results in a collision, stellar-mass BHs, located in dense stellar environments, can grow up to 10^6 $M_{\odot}$ within $\sim$ 1 Gyr. Our simulations include tidal capture prescriptions that lead to rapid circularization rather than a collision. The radius of the final circular orbit is set assuming angular momentum conservation. Therefore, in general, tidal capture events do not lead to collisions and might not contribute directly to the BHs mass growth. Nevertheless, the circular BH-star binary, once formed, have good chance to experience mass transfer or even mergers. Moreover, our instant tidal capture prescription requires knowledge of the orbital elements (pericenter and eccentricity) of the interacting objects. It is not activated during few-body chaotic encounters, where pericenter and eccentricity are not well-defined quantities. Therefore in some close interactions, we might underestimate the total number of tidal capture events.

4.4 Initial Conditions

Star clusters are expected to form from massive turbulent molecular clouds where gas is rapidly converted into stars. The high level of turbulence in these regions generates clumpy substructures in the whole star forming cloud. Numerical simulations indicate that violent relaxation erases initial substructure on a dynamical time scale (Scally & Clarke, 2002; Hurley & Bekki, 2008) and leaves a spherical density profile compatible with an Elson, Fall and Freeman (Elson et al., 1987) or a King (King, 1966) density profile. Moreover, in the early stages, gas and newly formed stars coexist in the same system. For moderately dense environments, only a small fraction of the cloud is converted into stars, the remaining gas is later ejected by stellar feedback and supernovae explosions. Although star clusters at formation are very compact, since they typically have sizes $\lesssim$ 1 pc (Marks & Kroupa, 2012; Fujii et al., 2021), gas ejection can lead to a rapid, strong expansion that can increase the size of the system to $\sim 5-10$ pc. This is especially true for low-mass star clusters ($10^3 - 10^4$ $M_{\odot}$). These types of systems are expected to lose their primordial gas in an interval of time of about $\sim$ 9 Myr (**?**Fujii et al., 2021).

On the other hand, observations show that young massive clusters (YMCs) such as NGC 3603, Trumpler 14, and Arches are devoid of dense gas despite being about $\sim$ 2 Myr old (sse Longmore et al., 2014, and citations therein). All these systems are very compact, with a photo-metric mass $> 10^4$ $M_{\odot}$ and and radii respectively equal to $0.7, 0.5, 0.4$ pc (Portegies Zwart et al., 2010). They are likely to originate from very dense gaseous environments, which thanks to their high density

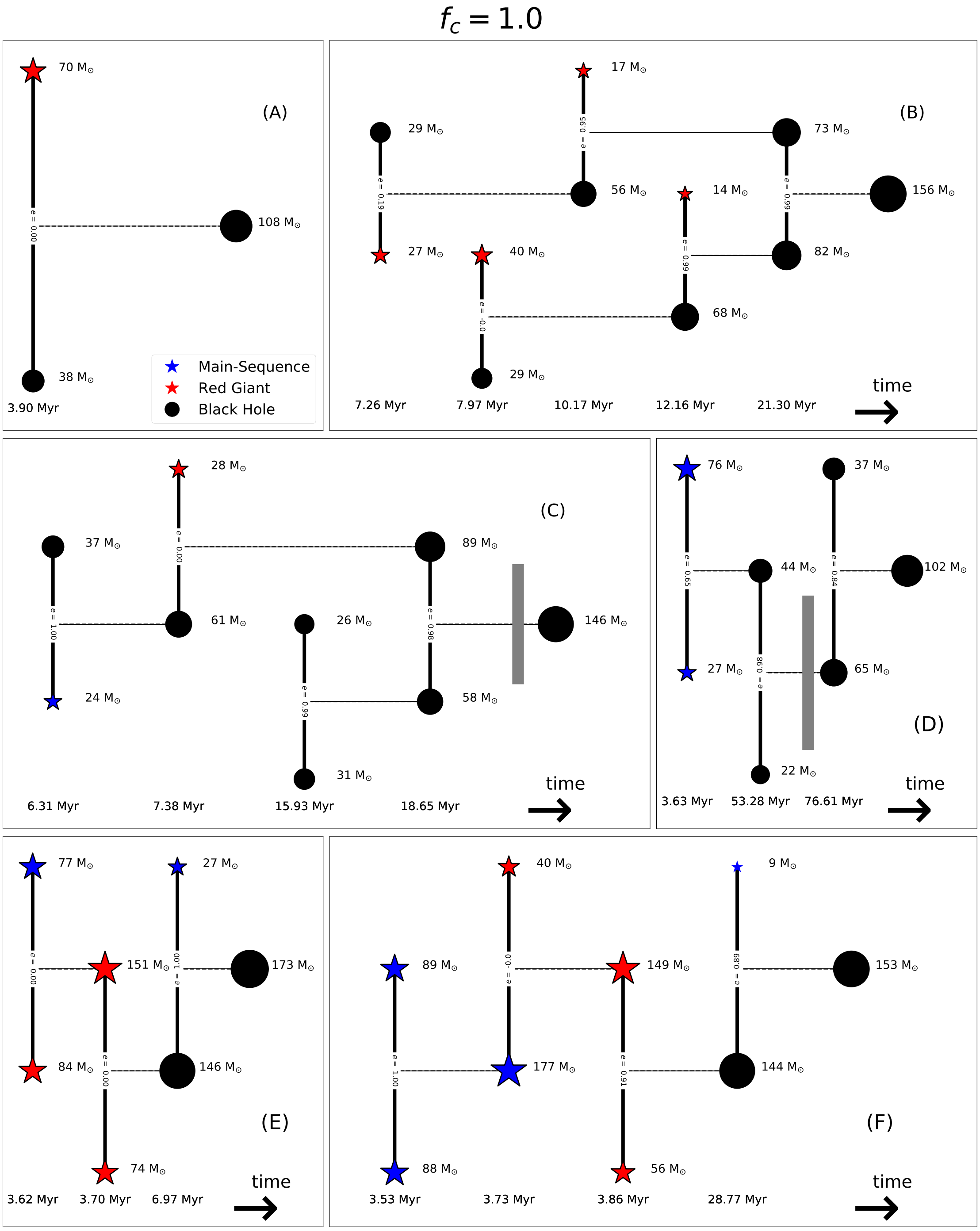

Figure 4.3: The formation paths of all six (A - F) BHs more massive than 100 $M_\odot$ formed in the $f_c = 1.0$ model. Main sequence stars and red giants are indicated by blue and red stars, respectively. Black holes are shown by filled black circles. The symbol sizes indicate the respective masses. The collisions on the right of the grey vertical segment would be certainly suppressed by relativistic kicks. Time goes from left to right and we give the masses and the eccentricities at the time of the collision. Paths C and D involve BH mergers before a GW190521-like mass gap merger which could have been prevented by recoil kicks. Path B offers a GW190521-like formation path only involving stellar accretion. Paths A, E, and F result in the formation of massive BHs in the IMBH range without stellar black hole mergers. For all examples, except C, we show the full formation path. The full path of C up to 100 Myr is shown in Fig. 4.4.

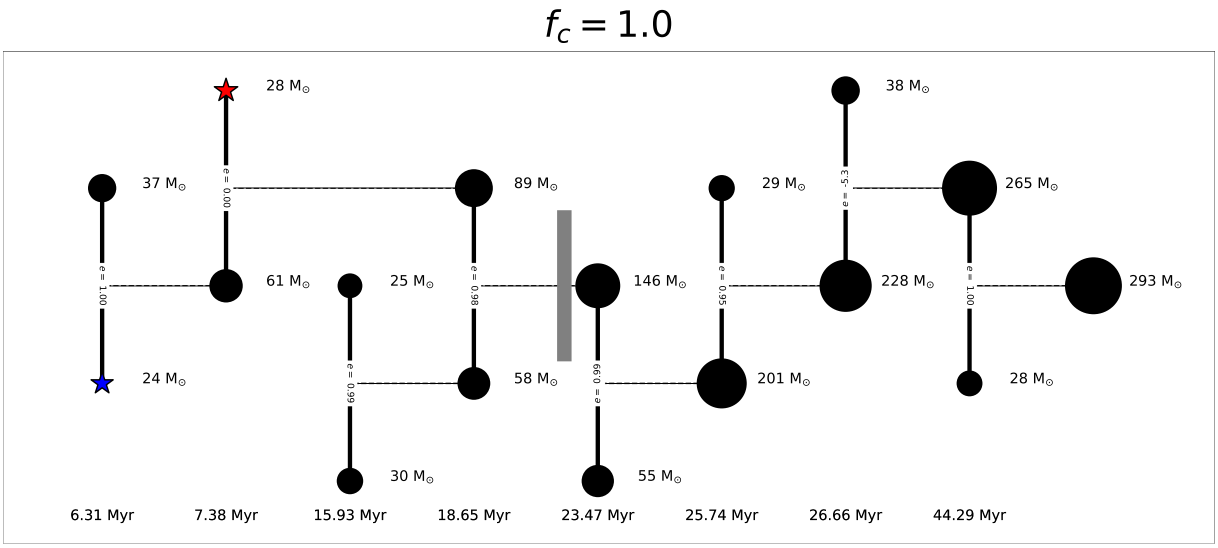

Figure 4.4: The formation path of the most massive BH formed in the 16 simulations. The final IMBH of 293 $M_\odot$ has formed through a chain of eight collisions. Panel C in Fig. 4.3 shows only the first 4. 6 collisions involve only BHs. This IMBH formed only because we did not include relativistic recoil kicks for BH - BH mergers. With kicks the mergers after the grey vertical line would not have happened as one of the progenitors had left the system already.

can maintain a high stellar formation efficiency, rapidly converting most of the gas into stars. In other words, these YMCs remove a big fraction of their primordial gas through exhaustion rather than ejection (Longmore et al., 2014). Therefore they can retain their initial compactness. The stellar formation phase for these systems has a very short duration, leaving a star cluster with a very narrow age spread (see e.g. Lahén et al., 2019, 2020, for the simulated formation of such systems in a galactic environment).

A recent three-dimensional radiation hydrodynamical simulations of YMCs formation support the picture just presented, indicating that stellar feedback suppresses star formation only in clouds with low surface density; When the initial surface density exceeds a certain threshold most of the gas is converted into stars (Fukushima & Yajima, 2021). In this last case, the star formation phase can last as little as 1 Myr.

Therefore, compact YMCs are ideal systems to be followed with direct N-body simulations, in spite of the fact that they are little affected by processes associated with gas ejections. We adopted the same initial conditions of the eight realizations of the model R06W6 presented in Rizzuto et al. (2021b). The model represents the state of young compact star clusters of 110.000 stars with 10% in binaries after gas removal. Their initial densities follow a King profile with initial half mass radius $R_\mathrm{h} = 0.6\,\mathrm{pc}$ and central potential parameter W_0 [2] $= 6$. Again, we assume that the systems maintain their initial compactness as the initial gas is removed by exhaustion from star formation. In addition, we assume the star formation phase is short-lived (see e.g Lahén et al.,

[2]The central potential parameter is defined as $W_0 = \frac{\psi(0)}{\sigma^2}$ where $\psi(0)$ is the potential at the centre of the cluster and $\sigma^2$is a parameter linked to the velocity dispersion of the system. See (King, 1966) for more details.

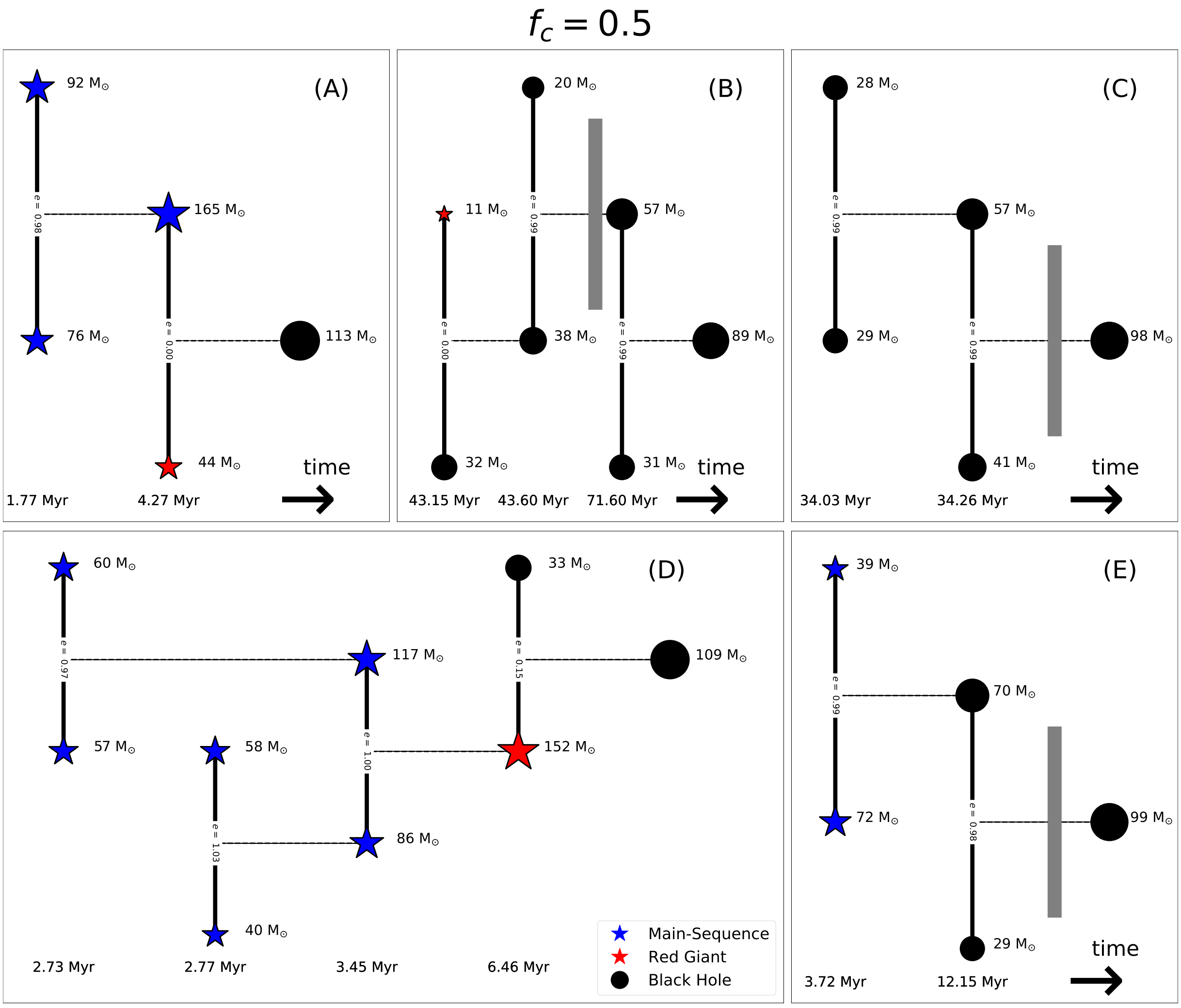

Figure 4.5: The formation paths of the five (A-E) massive black holes in the $f_c = 0.5$ model. The notation is the same as in Fig. 4.3. While this model also produces massive black holes, none of the formation paths involves a merger of two mass-gap BHs, like GW190521.

2019). Hence we neglect the initial age spread and we initialise zero-age main-sequence stars with a Kroupa initial mass function (Kroupa, 2001). All the systems started with a primordial binary fraction of 10%, initialised with a uniform semi-major axis distribution on a logarithmic scale from 0.001 AU to 100 AU, a uniform distribution of mass ratios, and thermal distribution of eccentricities.

In the simulations we allow BHs to accrete mass from a star in case of a collision. The fraction of stellar mass absorbed by a BH during such a star - BH collision, which we define as collision factor f_c, has a significant impact on the formation of IMBHs (see Rizzuto et al., 2021b). This mass fraction, in general, is difficult to estimate, as it depends on the relative velocity of the two colliding objects as well as the internal structure of the stars, etc. A quantitative assessment of this number requires complex hydrodynamical simulations. In this work, we treat this fraction $f_{\rm c}$ as a free parameter. We run 8 simulations setting $f_{\rm c} = 0.5$, and the other 8 with $f_{\rm c} = 1.0$.

4.5 Results

In Fig. 4.3, Fig. 4.4, and Fig. 4.5 we show the formation paths of the most massive BHs in the simulations for $f_{\rm c} = 1.0$ and $f_{\rm c} = 0.5$, respectively. Overall, these simulations with updated binary stellar evolution models confirm our previous result (Rizzuto et al., 2021b) that massive black holes in the mass-gap and even IMBHs more massive than 100 $M_\odot$ can form in compact star clusters through multiple mergers. With the new stellar prescriptions, the runs registered an even higher probability to form massive BHs. The latter build up their mass through at least one of these three channels:

1. Star - BH mergers: stellar BHs increase their mass by collisions with one ore more massive stars (see for instance panels A and B of Fig. 4.3 and panel D of Fig. 4.5).

2. BH - BH mergers: BHs grow by mergers with other BHs (i.e. panel C of Fig. 4.3 and panel C of Fig. 4.5).

3. The collapse of stars that are the product of previous collisions: a VMS formed through a series of subsequent collisions could acquire a large hydrogen-rich envelope maintaining a small helium core (M_c < 45 $M_\odot$), it is therefore little or not affected by (P)PSN and can collapse directly into an IMBH (i.e. panel F of Fig. 4.3 and panel A of Fig. 4.5.

This last formation channel was also observed in a recent set of N-body simulations by Di Carlo et al. (2021), who also assume no mass loss in stellar merger events. The importance of stellar mergers, however, depends on the prescription used to model collisions between stars. Our assumption of no mass loss might overestimate the impact of stellar mergers. For example, Glebbeek et al. (2009) use a detailed stellar evolution code and take into account the internal structure of massive stars formed through multiple collisions. They indicate that steller mergers likely lose most of their mass in the form of stellar winds. Moreover, our method does not account for remnant rotation. Even though the consequences of rotation have not yet been completely explored (Burrows & Vartanyan, 2021), high stellar spin is expected to enhance the mass-loss rate (Maeder & Meynet, 2000).

In general, at least two of the three processes mentioned above are always involved in the formation of a massive BH. For instance, the IMBH shown in panel C of Fig. 4.3 forms through the first and the second channel; while panel E of Fig. 4.5 presents an IMBH generated via the second and the third channel. The most massive BH in all simulations has a mass of 293 $M_\odot$. This object forms through 8 collisions 6 of them are BH - BH collisions as shown in Fig. 4.4. This long chain of BH mergers happens when, as in our simulations, relativistic recoil kicks are not considered. When two BHs collide, the relativistic recoil kick velocity depends on the mass ratio as well as the spin amplitude and direction of the two colliding objects. It can reach a few thousand kilometres per second (?Baker et al., 2008; Lousto & Zlochower, 2009; Kulier et al.,

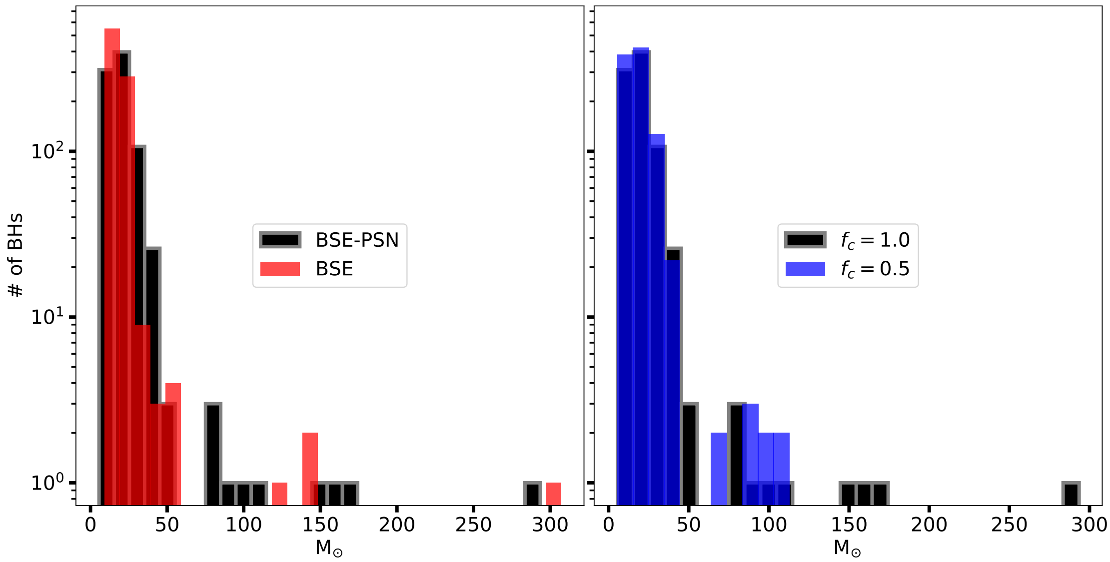

Figure 4.6: *Left panel:* Mass distribution of all BHs formed in the BSE model (red) and the BSE-PSN model (black) with $f_c = 1.0$ after 100 Myr of evolution. Simulations with BSE-PSN form more and more massive BHs in the (P)PSN mass gap and the IMBH mass regime. *Right panel:* Comparison of the BH mass distribution of the BSE-PSN model with $f_c = 1.0$ (black, same as left panel) to the model with $f_c = 0.5$ (blue). Lower accretion fractions for star-BH collisions result in less massive BHs.

2015; Morawski et al., 2018; Zivancev et al., 2020). Since the typical escape velocity in our clusters is 20-40km/s, it seems extremely unlikely that the 293 $M_\odot$ IMBH with this formation path can form in star cluster environments.

The first four collisions on the chain of mergers that lead to the 293 $M_\odot$ are reported in panel (C) of Fig. 4.3. Overall this panel shows two BH - star mergers and two BH - BH collisions that in the end generate a 146 $M_\odot$ IMBH. Since we expect that most stellar-mass BHs are born with a low initial spin, as indicated partially by the current GW data (Abbott et al., 2019; Miller et al., 2020; Roulet et al., 2020), and suggested by recent theoretical models (Fuller & Ma, 2019), the 146 $M_\odot$ IMBH has a non-negligible probability to form even with the inclusion of relativistic recoil as we shall discuss below.

Therefore, the $f_c = 1.0$ simulations provide two possible formation paths for GW190521. Path C is a second-generation event and has a low probability due to a first generation BH merger, as discussed above. Path B is more likely as the BH merger event itself is a first generation BH merger.

4.5.1 The impact of stellar evolution updates

After 100 Myr of cluster evolution, the BH mass distribution of the updated BSE-PSN model is very similar to the previous results as shown in the left panel of Fig. 4.6). The typical formation paths for the most massive BHS, however, differ significantly. In the Rizzuto et al. (2021b)

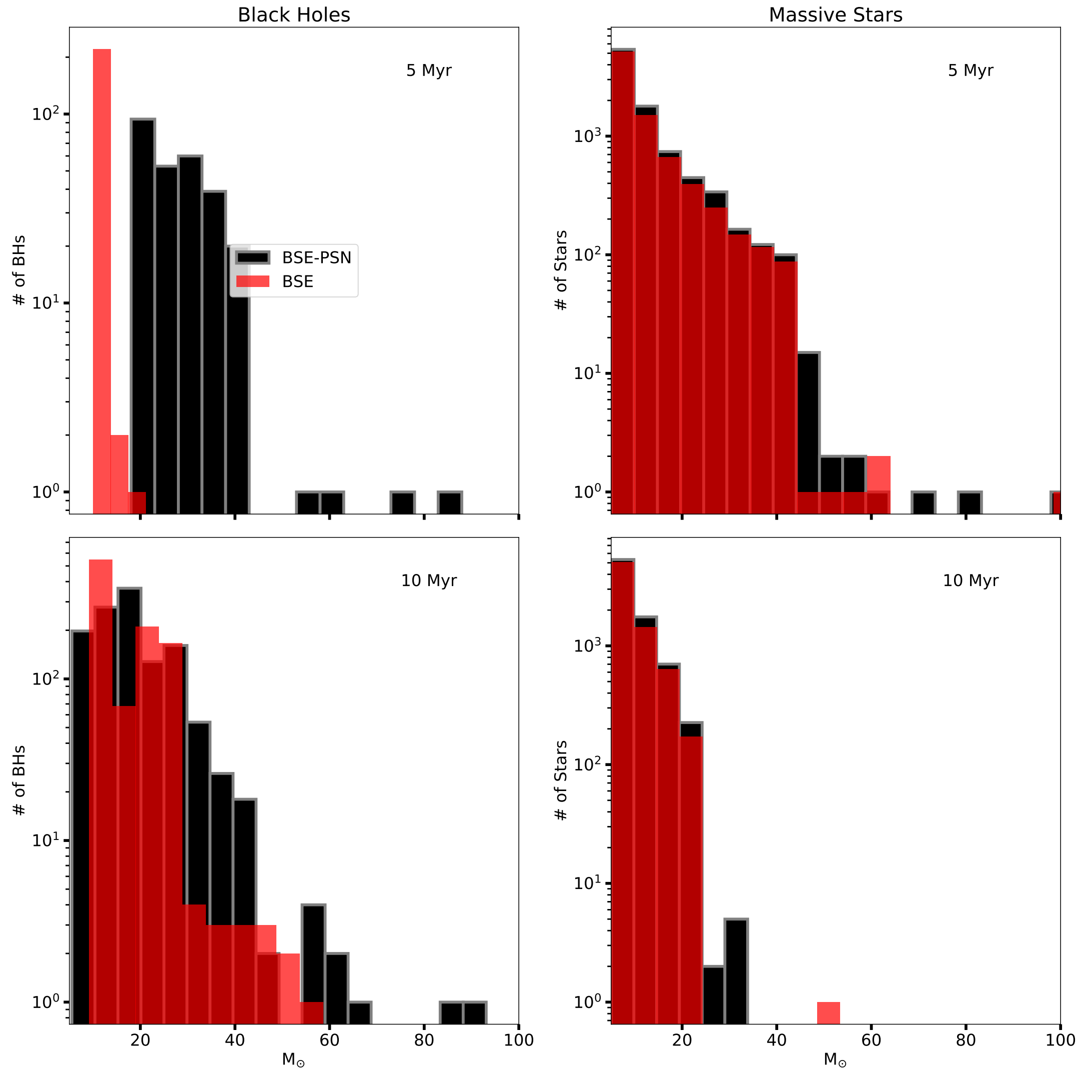

Figure 4.7: The two left (right) panels show the BH (massive stars) mass distribution after 5 Myr (top) and 10 Myr (bottom) of cluster evolution. In the BSE-PSN simulations (black histograms) 40 $M_{\odot}$ BHs form early in the simulation while massive stars $\sim$ 60 $M_{\odot}$ are still present (top panels). In contrast, the BSE clusters contains only $\sim$ 10 $M_{\odot}$ BHs after 5 Myr (red histograms). After 10 Myr the BSE-PSN model formed more massive BHs (bottom left panel) with a comparable stellar mass distribution (bottom right panel).

simulations (red histogram of Fig. 4.6, left panel) the BHs in the IMBH mass regime manly through mergers of BHs with VMSs: massive star experiences multiple stellar collisions reaching masses of 200 – 400 $M_\odot$. A large fraction of this is then accreted by a stellar BH in a collision. Typically, it is a single collision between a stellar BH and a VMS that determines whether or not the cluster forms an IMBH. While this formation path can also occur in BSE-PSN (see e.g. panel D of Fig. 4.5) it is not the dominant one.

In the BSE-PSN simulations, stellar BHs, before reaching the IMBH mass range, typically experience multiple collisions with massive stars and other BHs. In several cases, IMBHs form entirely, or almost entirely, via repeated BH mergers, as illustrated in panels B and C of Fig. 4.5 and panel D of Fig. 4.3. These formation paths are extremely rare in BSE; only 1 out of 80 simulations formed an IMBH through multiple BH - BH collisions.

The origin of this difference is the collision rate. The updated BSE-PSN model has about four times higher collision rate between massive stars and stellar BHs and three times higher BH-BH collision rate than BSE , and BH - BH. To understand this difference we briefly review the early cluster evolution. Within the first 4 Myr, the clusters undergo core-collapse driven by mass segregation of the most massive objects. Right after this initial collapse fast expansion is triggered by the mass loss of massive stars. For BSE-PSN massive stellar BHs form rapidly (see Fig. 4.2 and the top left panel of Fig. 4.7) and already populate the inner part of the cluster while the central density is at its maximum and when massive stars with a large collision cross-sections are still alive (top right panel of Fig. 4.7). High collision rates for star-BH and BH-BH mergers are the results.

This is not the case for BSE simulations. The first BHs that appear in the core-collapse phase of the BSE simulations have a mass of only $\sim$ 10 $M_\odot$ (see top left panel of Fig. 4.7) and they need a relatively long time to reach the inner part of the system, they typically reach the centre. At this time the clusters are not very dense anymore and $\gtrsim$ 40 $M_\odot$ stars are already gone. More massive stellar BHs ($\sim$ 30 $M_\odot$) start to populate the BSE simulations only after the most massive stars have already exploded (bottom panels of Fig. 4.7).

In contrast, $\sim$ 40 $M_\odot$ BHs populate the BSE-PSN clusters while massive stars are still alive (top panels of Fig. 4.7). Due to their short segregation time, these BHs can reach the core of the cluster, while it is still dense, and collide with one or more massive stars. At the same time while sinking into the centre they support and enhance the core collapse. To summarize, in the BSE clusters, since the first stellar BHs have low mass (10 $M_\odot$), they have little chance to reach the centre when it is still very dense; Instead, in BSE-PSN the first stellar BHs that appear in the system are more massive (40 $M_\odot$), therefore, they can reach the centre while it is still compact and therefore they have a higher probability to collide with other objects.

Overall, the simulations with BSE-PSN seem to generate a larger number of massive BHs. The left panel of Fig. 4.6 shows that BSE-PSN formed about 10 BHs more massive than 75 $M_\odot$, while BSE simulation only form 4 BHs. This difference is also connected with the fact that BSE-PSN can form massive BHs, as we mentioned previously, through direct collisions of VMSs. The direct collapse channel cannot occur in BSE because the stellar winds prescriptions are extreme and all VMSs lose most of their material before the collapse.

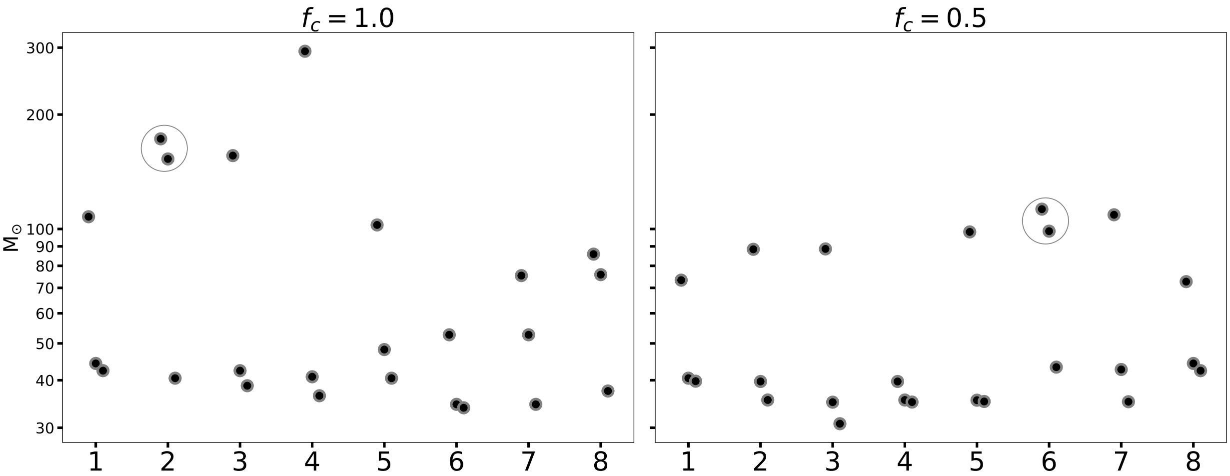

Figure 4.8: The mass of the three most massive BHs in each of the 8 realisations of the cluster simulations with $f_c = 1.0$ (left panel) and $f_c = 0.5$ (right panel). The first massive black hole is typically heavier in the $f_c = 1.0$ simulations, while the second and third have comparable masses to $f_c = 0.5$ models.

4.5.2 Comparison between simulations with different collision fractions

Fig. 4.8 compares the most massive BHs formed in the $f_c = 1.0$ simulations with the $f_c = 0.5$ simulations. As expected the former is more likely to generate BHs with higher masses. $f_c = 1.0$ models appear to be two times more likely to form IMBHs since already a single star - BH collision is enough to generate a BH heavier than 100 $M_\odot$ (as shown in panel (A) of Fig. 4.3). This can also be seen in the right panel of Fig. 4.6 showing the BH mass distributions generated by the two models: below $\sim 40\ M_\odot$ the two distributions are very similar. However, only the $f_c = 1.0$ model results in the formation of IMBHs above 150. The massive BHs of $f_c = 0.5$ model are lower masses in the range between 60 and 110 $M_\odot$.

As we mentioned earlier, because of the absence of observational and theoretical constraints, we choose f_c to be a free parameter. The constraints on f_c presented in the literature refer to tidal disruption events between a low mass star and a supermassive BH. They estimate an f_c in the range between $\sim 0.2 - 0.5$ (Shiokawa et al., 2015; Lu & Bonnerot, 2020; Wen et al., 2020) because most of the mass is lost in high-speed jets formed during mass accretion. However, when a low mass BH collides with a massive star, the scenario might be very different. Massive stars form very rapidly a compact core, so it might not be surprising that the actual core of the star is entirely absorbed by the BH right after the collision. Later on, the resulting BH, immersed in the envelope of the star, might continue to absorb stellar material. Due to the large size of the envelope of a massive star, the high-speed jets might be contained by the envelope itself, keeping most of the gas in the vicinity of the black hole. This situation resemble a similar scenario as described in Safarzadeh & Haiman (2020) and Rice & Zhang (2021). Under these assumptions, f_c might be close to unity.

The charts in Fig. 4.9 visualise the formation paths of the BH more massive lower limit of the (P)PSN mass gap (> 45 $M_\odot$) for the $f_c = 1.0$ and $f_c = 0.5$ models. Most stellar BHs reach

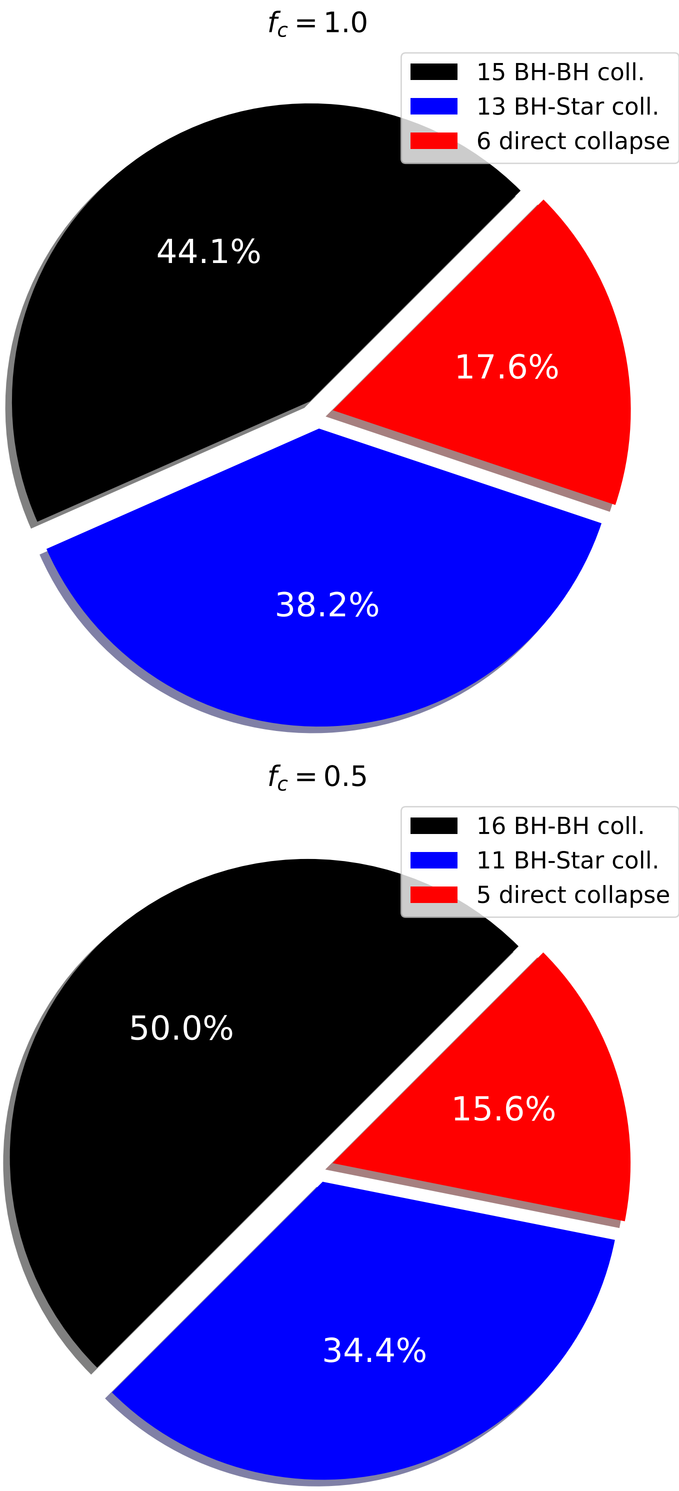

Figure 4.9: The Fig. shows in what percentage BH - BH mergers, BH - star coalescence, and direct collapse of stars (produced by previous collisions) contribute to the re-population of the (P)PSN mass gap in our simulations.

BH merger	V_{esc} (km/s)	P_1	P_2	P_3
Fig. 4.3 panel B Gen-a	38.1	3.05 %	82.2 %	100.0 %
Fig. 4.3 panel C Gen-a	40.3	1.91 %	0.00 %	0.00 %
Fig. 4.3 panel C Gen-b	38.6	0.00 %	0.00 %	0.00 %
Fig. 4.3 panel D Gen-a	29.2	0.00 %	0.00 %	0.00 %
Fig. 4.3 panel D Gen-b	25.8	0.00 %	0.00 %	0.00 %
Fig. 4.5 panel B Gen-a	31.2	0.00 %	0.00 %	0.00 %
Fig. 4.5 panel B Gen-b	27.1	0.00 %	0.00 %	0.00 %
Fig. 4.5 panel C Gen-a	35.7	4.44 %	99.0 %	100.0 %
Fig. 4.5 panel E Gen-a	41.5	0.00 %	0.00 %	0.00 %

Table 4.2: The table reports, for each BH - BH collision illustrated in Fig. 4.3 and 4.5, the retention probability of the BH merger remnant in the star cluster. V_{esc}: cluster escape velocity of the BH merger remnant. P_1: retention probability for an initial Gaussian spin distribution peaked on $S_1 = 0.2$, with a $\sigma = 0.2$ for the stellar BHs. P_2: retention probability for $S_2 = 10^{-2}$. P_3: retention probability for $S_3 = 10^{-3}$.

the mass gap by a merger with another BH. The next most important path is a collision with a star, followed by the direct collapse of a stellar merger remnant. The relative importance of the formation paths does not change significantly with the assumed accretion fraction - even setting $f_c = 0.5$, the star - BH collision channel produced 11 BHs in the mass gap just 2 less than the one produced with $f_c = 1.0$.

4.5.3 Comparison with LIGO/Virgo/Kagra gravitational wave detections

Our runs generated a large variety of BH mergers. The $f_c = 1.0$ simulations, for example, resulted in 27 BH - BH collisions (just 2 more than the $f_c = 0.5$ runs). These BH merger events cover almost the entire mass range of the LIGO/Virgo/Karga detections as shown in Fig. 4.10. Di Carlo et al. (2020) presented comparable results for a larger set of simulations of lower mass metal-poor star clusters. Interestingly, two-star cluster realisations with $f_c = 1.0$ have produced events with primary and secondary masses very similar to the GW190521 mass-gap detection. These BH merger events are highlighted in panels (B) and (C) of Fig. 4.3. Path B is particularly interesting as it indicates that BH mergers in the GW190521 mass range could originate from BHs which have grown by BH - star collisions. This formation path is not influenced by BH merger kicks. Therefore GW190521-like events might naturally occur in compact star clusters and they do not necessarily require very massive environments such as nuclear star clusters. The only requirements are that the environment is compact enough to trigger several BH - star mergers and that a large fraction of the stellar mass is accreted onto the BH during the collision.

As we have mentioned above, the simulations presented here do not include relativistic

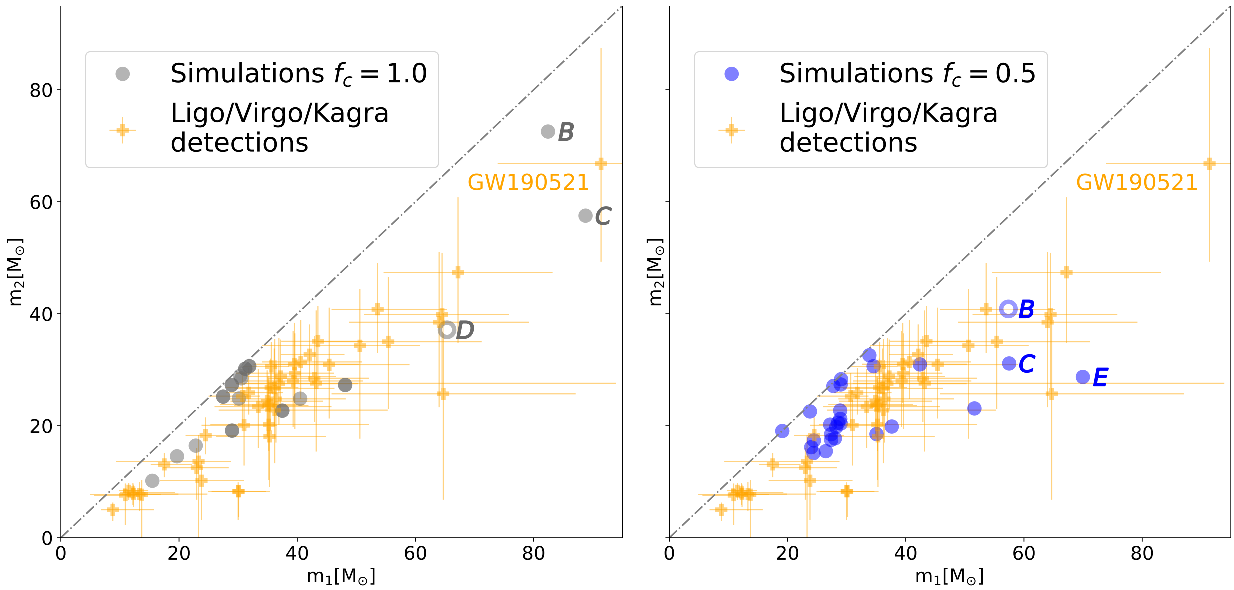

Figure 4.10: The panels show the primary (m_1) and secondary (m_2) BH masses of all BH mergers in the simulations for an accretion fraction of $f_c = 0.5$ (left, grey circles) and $f_c = 1.0$ (right, blue circles). The letters indicate the simulated formation paths highlighted in Fig. 4.3 and 4.5. The currently available LIGO/Virgo/Karga gravitational wave detections including error bars are indicated in orange. BH merger events that might be excluded due to gravitational recoil kicks are indicated with open circles. In general, the simulated events cover a similar parameter space as all currently available observations. The $f_c = 1.0$ simulations provide two possible formation paths for GW190521. Path C is a second-generation event and has a low probability due to a first generation BH merger. Path B is more likely as the event itself is a first generation BH merger.

velocity recoil kicks for compact object merger remnants. Therefore all massive BHs formed through two or more BH - BH collisions would have a much lower formation probability in the presence of kicks. The probability to retain a compact merger remnant in the cluster depends on its escape velocity as well as the spin and the mass ratio of the colliding BHs. Following Arca Sedda et al. (2021) we compute the kick velocity distributions for different assumed natal spins and quantify the retention probability of the BH merger remnants. We test three different initial spin distributions for stellar-mass BH, centered around $S_1 = 0.1$ with a Gaussian standard deviation of $\sigma = 0.1$, and fixed spins of $S_2 = 0.01$ and $S_3 = 0.001$, respectively.

We compute the retention probability for each BH - BH collision reported in Fig. 4.3 and 4.5 for all three spin distribution and present the results in Tab. 4.2.

Under the assumption that stellar BHs are born with very low spins (S_2 or S_3, Fuller & Ma, 2019), only the events (B) in Fig. 4.3 and (C) in Fig. 4.5 would survive the relativistic kick. In these cases, since the mass ratio is close to unity, the recoil velocity is lower than the escape velocity. For all the other cases $V_{\rm recoil} \gtrsim 50$ km/s therefore merger remnants have little to no chance to stay bound to the cluster.

If we assume the stellar BHs to be slowly rotating with distribution S_1 (as suggested by observations, e.g. Abbott et al., 2019), some BH - BH mergers have a non-negligible probability to stay in the star cluster for certain spin orientations. Under this assumption the first BH collision reported in the panel (C) of Fig. 4.3 has a probability of 1.9 % to stay in the cluster because of comparable masses. Therefore, similar events, which in turn resemble GW190521, could have been hosted in compact but not very massive star clusters as long as the BHs involved in the collisions are born with a low initial spin similar to S_2.

Another interesting event, that has non negligible probability to occur (see Tab. 4.2), is illustrated in panel (C) of Fig. 4.5. The plot shows the merger of a 57 $M_\odot$ and a 41 $M_\odot$ BH. Due to the similar masses the BHs this collision might indicate a possible formation channel for detected events like GW190701_203306 ($m_1 \approx 53.6$ $M_\odot$, $m2 \approx 40.7$ $M_\odot$ **?**).

To estimate the gravitational recoil velocity we implicitly assume that the spin of a BH is not affected during a collision with a massive star. While the BH spins of several low mass X-ray binaries are likely to be influenced by mass transfer from the companion into the BH (Podsiadlowski et al., 2003; Fragos & McClintock, 2015; Sørensen et al., 2017), all the three BH spins measured in high-mass X-ray binaries appear to have been affected very little by mass accretion (Qin et al., 2019). However, even allowing for larger BH spins for star-BH collisions our results would not change.

Two IMBH binaries form at the centre of two different realizations. The first one, a (173 $M_\odot$, 153 $M_\odot$) BH binary, whose formation paths are shown in panels (E) and (F) of Fig. 4.3, forms in the second realisation of $f_c = 1.0$ (see Fig.4.8). Right after formation, the two IMBHs evolve into a hard binary. At the end of the simulation ($t \approx 100$ Myr) this binary has an eccentricity of 0.81 and a semi-major axis of 1.88 AU, therefore, if evolved in isolation, will merge in about 11.5 Gyr. Both IMBHs in this binary formed from the direct collapse of a VMS. According to the stellar model we adopted, a star-forming from multiple stellar mergers might retain a small helium core. This in turn leads to a weaker (P)PSN allowing the star to collapse into a massive BH or even into an IMBH. We note that this result is connected to significant uncertainties of stellar evolution and we do not include the effect of rotation in VMSs, which could increase stellar winds mass-loss rate (Maeder & Meynet, 2000) and it could affect the final stage of the massive star Burrows & Vartanyan (2021). The second IMBH binary forms in the sixth realization of model $f_c = 0.5$ (see right panel of Fig. 4.8) and it involves two black holes of 113 and 99 $M_\odot$ (see panels (A) and (E) of Fig. 4.5). However, since the 99 $M_\odot$ object is the product of a 70 and 29 $M_\odot$ BH merger, it is very likely to escape the cluster right after formation (see Tab. 4.2). Even if it stays in the cluster this IMBH binary would have an expected merging time in isolation greater than the Hubble time (at the end of the run the binary has eccentricity equal to 0.75 and semi-major axes of 3.25 AU). Nevertheless, the merging time could be considerably reduced by chaotic and hierarchical interactions.

4.6 Conclusions

We study a collisional formation scenario for IMBHs and BHs in the (P)PSN mass gap in young compact star clusters utilizing direct N-body simulations carried out with a version of NBODY6++GPU that contains relativistic treatments to include the GW energy loss in compact binaries. We rerun 16 realizations of the model R06W6 introduced in Rizzuto et al. (2021b) with updated stellar evolution recipes. The upgrades follow the implementations in Banerjee (2020) and include new metallicity-dependent stellar winds prescriptions, recipes for the electron-capture supernovae, and treatments for (P)PSN. The latter creates a mass gap in the BH mass spectrum between 45 and 195 $M_\odot$ (see Fig. 4.1).

Overall our simulations show that $\sim 10^5$ $M_\odot$ compact star clusters have a good chance to generate BHs in the (P)PSN mass gap or even in the IMBH mass range ($\gtrsim 100$) as shown in Fig. 4.6. Together with BH - BH collisions, BH - star collisions seem to play an important role in the formation of massive BHs. We parameterize the fraction of stellar mass absorbed by the BH to be unity ($f_c = 1.0$) or 50% ($f_c = 0.5$). The Simulations with $f_c = 1.0$ and $f_c = 0.5$ can generate BH merger events with primary and secondary BH masses compatible with nearly the whole mass range of LIGO/Virgo/Kagra gravitational wave detections (see Fig. 4.10). As we do not follow gravitational recoil, we have, a posterior, estimated, the retention probability for a BH - BH merger in the star cluster and have identified all unlikely formation paths.

The model assuming efficient accretion ($f_c = 1.0$) of stellar material in a merger with a BH generates two BH merger events with primary and secondary masses compatible with the mass-gap merger event GW190521 (**?**). For one event, both colliding BHs grow entirely through BH - star mergers (see panel (B) Fig. 4.3). Therefore, the final merger is independent of gravitational recoil kicks and might not only be expected in high escape velocity systems such as nuclear star clusters. GW190521 like mergers might also form in lower mass compact star clusters at low initial metallicity. The only requirement is that the system is compact enough to trigger many BH - star collisions and that the amount of mass accreted by the BH during the collision is close to unity.

The chain of collisions that led to the second GW event involves two BH - star collisions and one BH - BH collision before the final merger (see panel (C) of Fig. 4.3). When these two compact objects merge, the final product should experience a recoil kick which depends on the spin orientation and magnitude of the colliding objects. For low spins, ~ 0.1 the probability that the product of this BH - BH collision stays in the cluster is low (1.9%) but non-zero, therefore this formation path is not excluded.

Contrary to the $f_c = 1.0$ model, the 8 realizations of the model $f_c = 0.5$ did not form BH mergers in the mass range of GW190521 because $f_c = 0.5$ simulations tend to form less massive progenitor BHs (see Fig. 4.8, and right panel of Fig. 4.6). However, the total number of BHs in the (P)PSN mass gap generated by the two models through BH - star collision is comparable (see Fig. 4.9). Even imposing $f_c = 0.5$, BH - star mergers can bring stellar BHs in the (P)PSN mass range. In one simulation we even form a hard IMBH binary of 153$M_\odot$ and 173 $M_\odot$ (see (E) and (F) of Fig. 4.3) which is expected to merge within a Hubble time. Its formation, however, depends on details of the evolution of very massive stars which are only approximately captured by the stellar evolution models used in this study.

Chapter 5

Tidal captures in dense stellar environments

5.1 Introduction

Collisional systems with very high densities $\rho \gtrapprox 10^6\,\mathrm{M}_\odot/\mathrm{pc}^3$ are as interesting as they are difficult to explore. They are fascinating because the processes that regulate their evolution may conceal mechanisms that lead to the formation of very massive objects for which little is known about their origin. For instance, intermediate-mass black holes, which could power the most energetic X-ray sources observed (Mezcua et al., 2015; Mezcua, 2017), or super massive black holes (SMBHs), which inhabit the centre of most large galaxies (see Kormendy & Ho, 2013, and citations therein), or even more exotic objects such as super massive stars whose formation has been proposed as an explanation for the HeCNONaMgAl abundance anomalies (Gieles et al., 2018). At the same time, they are laborious to investigate because they require accurate and expensive N-body simulations. Analytical models can mostly provide qualitative descriptions of the phenomena occurring in such environments. Accurate numerical experiments are necessary to verify or disproof the analytical estimations. Moreover, only numerical methods can provide detailed quantitative results.

The first numerical study of collisional spherical systems with densities above $\rho > 10^7\,\mathrm{M}_\odot/\mathrm{pc}^3$ was carried out by approximating the solution of the equation of motions via Monte Carlo simulations (Sanders, 1970). This study, despite neglecting the effect of mass segregation, indicates that such systems reach a very high merger rate and they can lead to the collisional formation of massive objects. Subsequently, multi-mass Fokker-Planck simulations indicated that the core of compact and very massive systems can trigger a cascade of mergers, enhanced by mass segregation, that can lead to the formation of heavy BHs with masses around ~ 100 $\mathrm{M}_\odot$ (**?**). Results that have been confirmed by low particle number ($N = 1000$) direct N-body simulations of similar stellar systems (Lee & Ostriker, 1993). The observation of a very energetic X-ray source located in the young compact cluster MGG-11 (Matsumoto & Tsuru, 1999; Kaaret et al., 2001) suggested the presence of an IMBH of $\sim 1000\ \mathrm{M}_\odot$ in the cluster. Motivated by this discovery, Portegies Zwart & McMillan (2002); Portegies Zwart et al. (2004) realized a series of direct multi-mass N-body simulations to model the dynamical evolution of MGG-11-like clusters and showed that such a system, due to the short mass segregation time, can trigger a chain of mergers that lead to the formation of a massive star of $\sim 10^3$ M$_\odot$ that would directly collapse into an IMBH of similar mass. With 128.000 stars, these are the first direct N-body simulations of dense star clusters with a realistic number of particles. Nevertheless, they lack many important stellar evolution prescriptions[1] and they explore only the early evolution (the first $\sim$ 10 Myr) of the clusters. In addition, the criteria adopted for stellar collisions is very basic: they assume a merger to occur when the distance between two stars becomes smaller than the sum of the stellar radii. Adopting this criterion they ignore all the possible collisions induced by tidal disruption (TC) or triggered by tidal capture (TC). In fact, analytical studies indicate that TC events might significantly enhance the overall collision rate of the system (Lee & Ostriker, 1986) and might lead to the formation of SMBHs in very dense stellar environments (Stone et al., 2017).

The analysis of several hundreds Monte Carlo simulations of very high-density clusters (Giersz et al., 2015) takes a further step towards a more complete understanding of dense systems. These simulations revealed a *fast* and a *slow* scenario for the formation of IMBHs. The former is triggered by large cluster concentrations ($\rho \gtrapprox 10^7$ M$_\odot$/pc^3) that lead to the formation of $\sim 10^3 - 10^4$ M$_\odot$ BHs in the first few Myrs of the cluster evolution, right after the explosions of the most massive stars. In such scenario the IMBH form in two steps: firstly a very massive star (VMS) grow through many stellar collisions, secondly, a low mass black hole meets the VMS in the core and absorbs most of its mass. On the other hand, in the slow formation scenario, a low mass BH starts to grow in mass much later on in the cluster evolution, typically at the beginning of core-collapse. The timescale for the BHs to reach the IMBH mass range is of the order of a few Gyrs and in some cases, it can exceed the Hubble time. Direct N-body simulations of compact star clusters confirm the fast scenario (Rizzuto et al., 2021b). They also show that young compact star clusters can generate IMBHs in a time scale of $\sim$ 10 Myr through VMS-BH collisions. Although these simulations produced at most IMBHs about 350 M$_\odot$ because clusters with masses $M > 10^5$ M$_\odot$ and densities $\rho \geq 10^8$M$_\odot$/pc^3 were not explored being computationally too expensive.

Most of the the numerical studies that model the evolution of collisional stellar environments seem to indicate that sufficiently compact systems can lead to the formation of massive objects or they can even trigger runaway collisions[2]. None of this work, not even the most recent one, tried to quantify the role that TC might play on this scenario. For instance, Rizzuto's and Giersz's models include prescription for TC assuming that every tidally captured star rapidly circularize in a stable hard binary. However, they did not assess the weight that these events have on the formation of IMBH. They did not disentangle the effect of tidal capture from other process. It is therefore very difficult to understand whether TC is the dominant process on the formations of very massive BHs in dense stellar systems as suggested by analytical studies (Stone et al., 2017).

This work is dedicated to understanding quantitatively the role that TC events have on the formation of massive objects in dense stellar environments, and which conditions can trigger tidal capture runaway collisions. For this purpose, we simulate the evolution of several compact star clusters with the help of the direct N-body code FROST (Rantala et al., 2021) coupled with tidal

[1]For instance stellar winds for massive stars was not included.

[2]An objects undergoes a collisional runaway growth if the mass growth rate does increase with growing mass

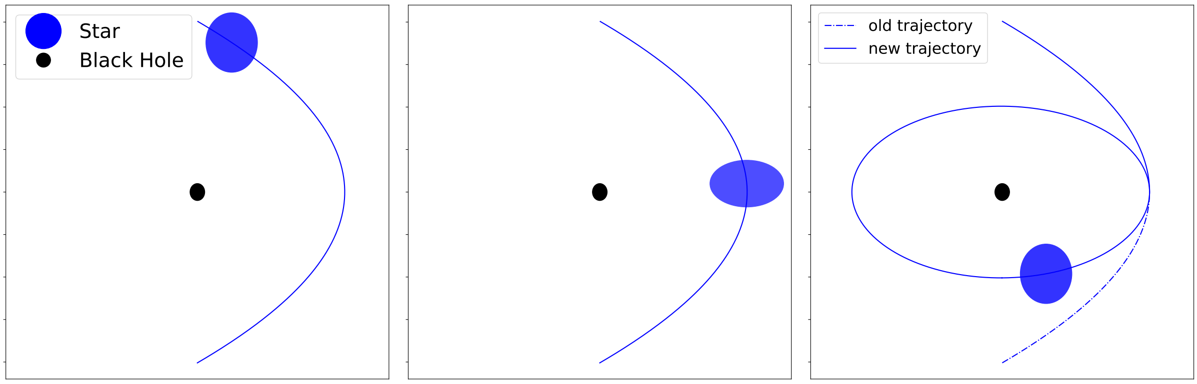

Figure 5.1: Schematic illustration of a star tidally captured by a BH. On the left panel, the star orbits the BH moving in an open orbit ($e \gtrsim 1$). The star, while passing through the pericenter, BH exerts a tidal force over the star and stretches it out (central panel). As a consequence of the deformation, the star begins to oscillate: part of the orbital energy is transformed into oscillatory energy. Consequently, the orbital energy can become negative; If this is the case, the star is tidally captured and moves in a bound orbit around the BH (right panel).

interaction recipes to take into account the effects of tides in close encounters. In Section 2, we described in more detail the numerical treatments adopted to follow the dynamical evolution of our systems. The initial conditions of the clusters are presented in Section 3. In Section 4 we present the analysis of our runs focusing the discussion on the role played by TC in the formation of heavy BHs. In the final section (Section 4) we summarize the main results of this work and discuss possible future projects.

5.2 The Method

To study the collisional tidal capture scenario for the formation of massive BHs we realized 9 simulations of compact star clusters evolved using the direct N-body algorithm FROST (Rantala et al., 2021). This code, thanks to its efficient CUDA-MPI parallelization scheme, can integrate massive and dense systems up to 10^6 particles. It uses a 4^{th} order forward integrator inserted in a 4^{th} order Hamiltonian splitting scheme that, together with the time-step symmetrization scheme, ensure high integration accuracy and extremely low energy error. To resolve the trajectories of particles in close encounters, or to resolve the orbit of hard binaries FROST uses the logarithmic Hamiltonian regularization method presented in Rantala et al. (2020). The latter guarantees accurate and efficient integration of energetic few-body interaction, and, since it includes post-Newtonian correction up to the 2.5 order (Blanchet et al., 2006), it can correctly determine the trajectories of compact object binaries up to few instants before the coalescence.

When a star is close enough to a compact object, it can experience a tidal force strong enough to rip it apart. We include this effect in our N-body code. Therefore, every time a star of mass m_1 and radius R_1 approaches a compact object of mass m_2 we assume the star to be tidally disrupted

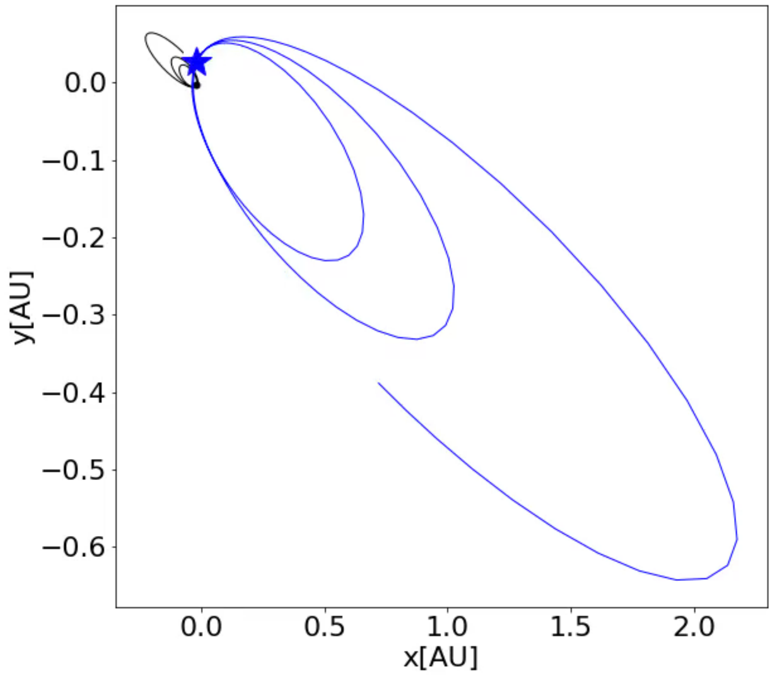

Figure 5.2: The figure displays the evolution of a BH tidally interacting with a 1 $M_\odot$ star initially moving in a hyperbolic orbit with pericenter $r_p = 4R_\odot$ and eccentricity $e = 1.001$. The tidal force is model using the DFTC prescription (see eq. 5.5). With this prescription the two objects after capture spiral in and collide in less than a year.

if their separation r is smaller then the tidal radius $r < r_{\rm tide}$. Following the disruption criterion defined in Kochanek (1992) the tidal radius $r_{\rm tide}$ we adopted in this work is:

$$r_{\rm tide} = 1.3R_1 \left(\frac{m_1 + m_2}{2m_1}\right)^{1/3} \tag{5.1}$$

During tidal disruptions or direct collisions between a star and BH, the mass accretion is expected to happen at super-Eddington rate as long as the BH is in the stellar mass range. Consequently, a fraction of incoming mass will be lost in outflows. The exact amount of mass loss is still debated in the literature. For this work, we assumed that the BH absorbs 50% of the total mass of the star and the other half is instantly removed from the system.

When the star m_1 moves in a orbit with pericenter $r_p > r_{\rm tide}$ the star will not be tidally destroyed. However, it might still experience a non-negligible tidal force that might lead to an energy exchange that in turn might affect the orbit of the star itself. When a star passes close enough to a BHs, the tidal interaction between the two objects might lead the star to deform and oscillate (as illustrated in the central panel of Fig.5.1). A fraction of the orbital energy of the two-body system is therefore transformed into the internal energy of the star. The orbital energy loss, that follows this process, might induce objects, that move along parabolic or quasi parabolic orbits, to form bound systems. To estimate the energy lost during a parabolic encounter, Press & Teukolsky (1977) approximate the oscillatory motion of the perturbed star through an expansion in spherical harmonics. With their procedure, the fraction of orbital energy deposited into the star is:

$$\Delta E = \int_{-\infty}^{+\infty} \frac{dE}{dt} dt \approx \frac{Gm_1^2}{R_1} \left(\frac{m_2}{m_1}\right)^2 \sum_{l=2}^{\infty} \left(\frac{R_1}{r_p}\right)^{2l+2} T_l(\eta). \tag{5.2}$$

In practical applications, the series is truncated at $l = 3$ because higher terms give only a small contribution to the final value of ΔE. The coefficients T_l are dimensionless functions of the parameter η, which represents the duration of the pericenter passage in respect to the hydrodynamical timescale of m_1 as it follows from its definition:

$$\eta := \left(\frac{m_1}{m_1 + m_2}\right)^{1/2} \left(\frac{r_p}{R_1}\right)^{3/2}. \tag{5.3}$$

The actual values of T_l depend on the internal structure of the deformed object. In our simulation, since we relate a polytropic index n to each star according to their mass, it depends on the structure of the polytrope. For low mass stars with $m < 0.7\ \mathrm{M}_\odot$ we associate the polytropic index $n = 1.5$. While for stars with $m > 0.7\ \mathrm{M}_\odot$ we set $n = 3$. With this choice heavy stars, tend to be less affected by tidal interactions[3]. In fact, the values of T_2 and T_3, computed for $n = 3.0$, are significantly smaller then the values computed for $n = 1.5$ (Portegies Zwart & Meinen, 1993, see Fig. 1 in). Our code evaluates T_2,T_3 for every close interaction by means of the rapid fitting function presented in Portegies Zwart & Meinen (1993). The latter reproduces the values of T_l computed by Lee & Ostriker (1986).

The formula reported in eq. 5.3, have been derived exclusively for parabolic encounters (eccentricity = 1). To extend this formulation for eccentricities slightly larger or slightly smaller than 1 we utilize the prescription illustrated in Mardling & Aarseth (2001) appendix A, which provides a generalization of eq. 5.3 by introducing a new expression for η (that we indicate with the Greek letter ζ) that depends explicitly on the eccentricity of the orbit:

$$\zeta := \eta \left(\frac{1}{1+e}\right)^{\alpha(\eta)/2} \tag{5.4}$$

where $\alpha(\eta) = 1 + \frac{1}{2}\left|\frac{\eta-2}{2}\right|$, therefore for $e = 1$ we restore the original formulation. Numerical experiments show that using $T_l(\zeta)$ instead of $T_l(\eta)$ lead to better accuracy for hyperbolic orbits ($e \gtrsim 1$). For orbits of smaller eccentricity, the tides switch from the dynamical to equilibrium regime. The amount of tidal energy dissipation, therefore, decreases with decreasing eccentricity. To take into account this effect, we multiply the energy dissipation ΔE by the eccentricity e of the orbit for $e < 1.0$ (a similar prescription is used in Baumgardt et al., 2006).

After describing the procedures adopted to estimate ΔE, the amount of energy dissipated during tidal interactions, there remains the problem of understanding how to use ΔE to change the orbit of the two interacting objects. For this work, we adopted two different prescriptions which we outline in detail in the next two sections.

5.2.1 The instant emission tidal capture prescription

The first method we adopt is the instant emission tidal capture (IETC) criteria summarized in the following steps:

[3]With this very simple approximation we are assuming that only stars with a large convective envelope can be efficiently induced to oscillate

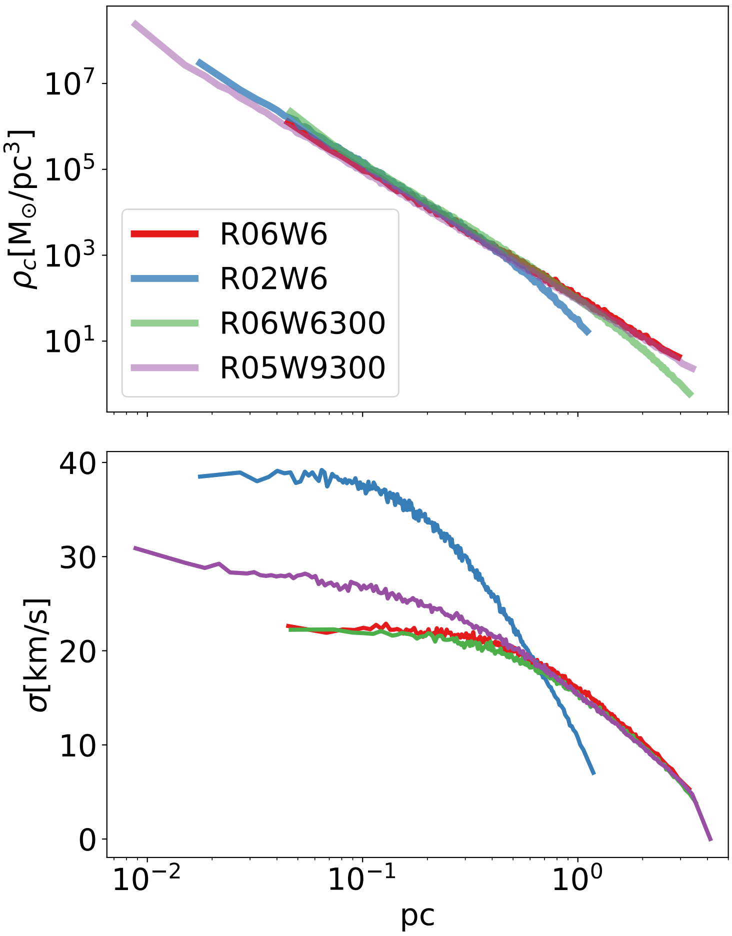

Figure 5.3: The plot shows on the upper panel, the initial radial density profile of the 4 star cluster initial conditions used in this work. The right panel show their initial dispersion velocity profile. Intentionally, the model R02W6 has been initialized with a central dispersion velocity of $\sim$ 40 km/s, to test whether such cluster will trigger tidal capture runaway collisions as found analytically by Stone et al. (2017).

1. When a star moves in an open orbit ($E_0 \geq 0$) close to a BH (or compact object), the tidal energy dissipated ΔE is computed as soon as the star passes close to the pericenter.

2. If the new energy $E = E_0 - \Delta E < 0$, the star is tidally captured and we assume that this lead to an instant collision.

3. If $E = E_0 - \Delta E > 0$, the motion of the particles is left unchanged.

Here we need to mention that the outcome that follows a TC event is very debatable, and it is highly unclear whether tidal captures lead to fast mergers as we assumed. What we can say for sure is that a star after being captured, if not affected by external perturbations, follows a bound but very eccentric orbit (see right panel of Fig. 5.1 as an illustration). If internal mechanisms (such as viscosity) of the star are adequately efficient to rapidly dissipate the oscillatory motion of the star, at the second pericenter passage, the star will experience again a strong tidal interaction that leads to orbital energy loss and consequently to the shrink of the semi-major axes. The process repeats until, or the star gets destroyed and swallowed by the BH, or the two bodies circularize. The outcome mainly depends on the ability of the star to radiate away the internal energy gained during the tidal interactions. If the radiation is not very efficient, the star would expand and it would be tidally disrupted after few pericenter passages. If, on the other hand, the heating radiates away efficiently the energy in excess, the two interacting objects are expected to form a circular stable binary. The star would be, in any case, consumed by the BH through stable mass transfer only in a much longer timescale. If the mechanism for dumping the oscillations is not sufficiently efficient, tidal capture with a small pericenter might lead to a chaotic random evolution (Mardling & Aarseth, 2001). In fact, the pericenter passages that follow the capture can further excite but also dump oscillation modes in the deformed star. In other words, the orbit and the star can randomly exchange packages of energy in both directions. The resulting trajectories of the object are unpredictable and resemble a random walk.

One of the main caveats to the IETC method is that it ignores the effect of external perturbations. After tidal capture, a star moves in a very wide elliptical orbit which possible can be affected by intruders especially in very dense stellar environments where TC events are more likely to occur. Moreover, this method is unreliable during chaotic few-body interactions. In, the IETC prescription, the code needs to know the orbital elements (semi-major axes and eccentricity) of two approaching particles. However, these quantities are not well defined during chaotic encounters.

5.2.2 Modeling tidal interactions with a drag force

To address those issues we implement in FROST the approach described by Samsing et al. (2017) that uses the drag force tidal capture (DFTC) method. With this model, tidal interactions are approximated using a drag force given by:

$$F_{\rm t}(r,v) = C\frac{v}{r^4} \tag{5.5}$$

where r, v are the respectively the relative separation and relative velocity of the two tidally interacting bodies, while C, is a normalization factor and it is chosen so

$$\int_{orb} F_t(r,v)dr = \Delta E \tag{5.6}$$

here ΔE is the same quantity computed in the instant emission treatment. This definition of C ensures the two methods give practically the same results for an unperturbed two-body interaction because they generate the same total amount of energy dissipated per orbit. The Fig. 5.2 displays the trajectory of a 1.0 $M_\odot$, captured by a 10.0 $M_\odot$ BH. The two-body system, evolved with the DFTC method, ends up in a collision in 0.9 years: even with the drag force prescription the BH and star merge almost instantly, as long as external objects are not included. The steep dependency $F_{\rm t} \propto \frac{1}{r^4}$ ensures the tidal interactions to be effectively activate during very close encounter and to be negligible at long distances. In summary with the drag force method, we are able to model tidal capture events following the trajectories of the interacting objects from the moment of the capture to the collision. We are therefore able to take into account how possible intruders might affect the orbit and at the same time, we are able to self-consistently include tidal interactions in few body encounters.

Model Name	stellar population	W_0	R_h[pc]	σ_c[km/s]	$\rho_c[M_\odot/pc^3]$	$M_{IMBH}[M_\odot]$	# BHs
R06W6	200 Myr old	6	0.6	22	1.1×10^6	/	453
R02W6	200 Myr old	6	0.2	39	3.0×10^7	/	451
R06W6IMBH	$0.08 < m^*[M_\odot] < 3$	6	0.6	22	2.1×10^6	300.0	0
R05W9IMBH	$0.08 < m^*[M_\odot] < 3$	9	0.5	32	2.2×10^8	300.0	0

Table 5.1: Initial parameters of the cluster simulations: stellar population: a) Kroupa (2001) IMF with stellar masses $0.08\,M_\odot < m^* < 100\,M_\odot$ evolved for 200 Myr, b) Kroupa (2001) IMF with stellar masses $0.08\,M_\odot < m^* < 3\,M_\odot$; W_0 : central potential parameter for the King density profile (King, 1966); R_h : half mass radius; σ_c : initial central dispersion velocity; ρ_c : initial central density; M_{IMBH}: mass of the central IMBH ; # BHs: number of stellar BHs presented in the cluster at initial time.

5.3 Initial Conditions

We used the code MCLUSTER (Küpper et al., 2011)to generate the initial conditions of 4 star clusters. whose properties are summarized in Tab. 5.3. All the 4 models are initialized with 256.000 single stars with positions and velocities sampled from a King (1966) density profile. Two models, R06W6, R02W6, contain 200 Mry old stellar populations. Their initial conditions have been generated in two steps: firstly the mass of the star have been sampled from Kroupa (2001) IMF assuming a minimum and a maximum stellar mass of 0.08 $M_\odot$ and 100 $M_\odot$ respectively. Subsequently, each individual star has been evolved for 200 Mry using the most updated version of the synthetic stellar evolution package BSE (see Chap. 4 for more details). Therefore, these two models contain mainly low mass stars, about 4500 low mass compact objects such as neutron stars (NSs) and white dwarfs (WDs), and about 450 stellar BHs whose mass reange from 5 $M_\odot$ up to 45 $M_\odot$. The model R06W6 has an initial half mass radius of $R_h = 0.6$ pc and an initial central density parameter $W_0 = 6$ which together lead to a central density $\rho \approx 1.1 \times 10^6\,M_\odot/pc^3$ and a central dispersion velocity $\sigma_c = 22$ km/s. Despite its very high density, R06W06 is expected to not be compact enough to trigger tidal capture runaways. The analytical model developed in Stone et al. (2017), indicates that only clusters with a central dispersion velocity $\sigma_c \gtrapprox 40$ km/s can produce runaway collisions. Therefore, we generated the model R02W6, which has the same central density parameter of R02W6, but is three times smaller in size. Whit these initial conditions W02R6, according to Stone's model, should be dense enough to trigger runaway collisions and lead to the formations of massive BHs. This extreme initial setup could resemble the core of a nuclear stars cluster where super massive BHs might have formed. Several Monte Carlo simulations (Giersz et al., 2015), and direct N-body simulations (Rizzuto et al., 2021b,a), indicated that compact star clusters can form IMBHs of few $\sim 10^2\,M_\odot$. Some of the Monte Carlo runs also illustrates that the IMBHs, once formed, ejects all the low mass BHs from the cluster through energetic few-body encounters. After a few hundred Myr. The cluster is left only with low mass stars and the IMBH. Motivated by the outcome of these runs, the models R06W6300 and the model R05W9300 are initialized with a central 300 $M_\odot$ IMBH surrounded only by stars with masses between 0.08 $M_\odot$ and 3 $M_\odot$ sampled from (Kroupa, 2001) IMF.

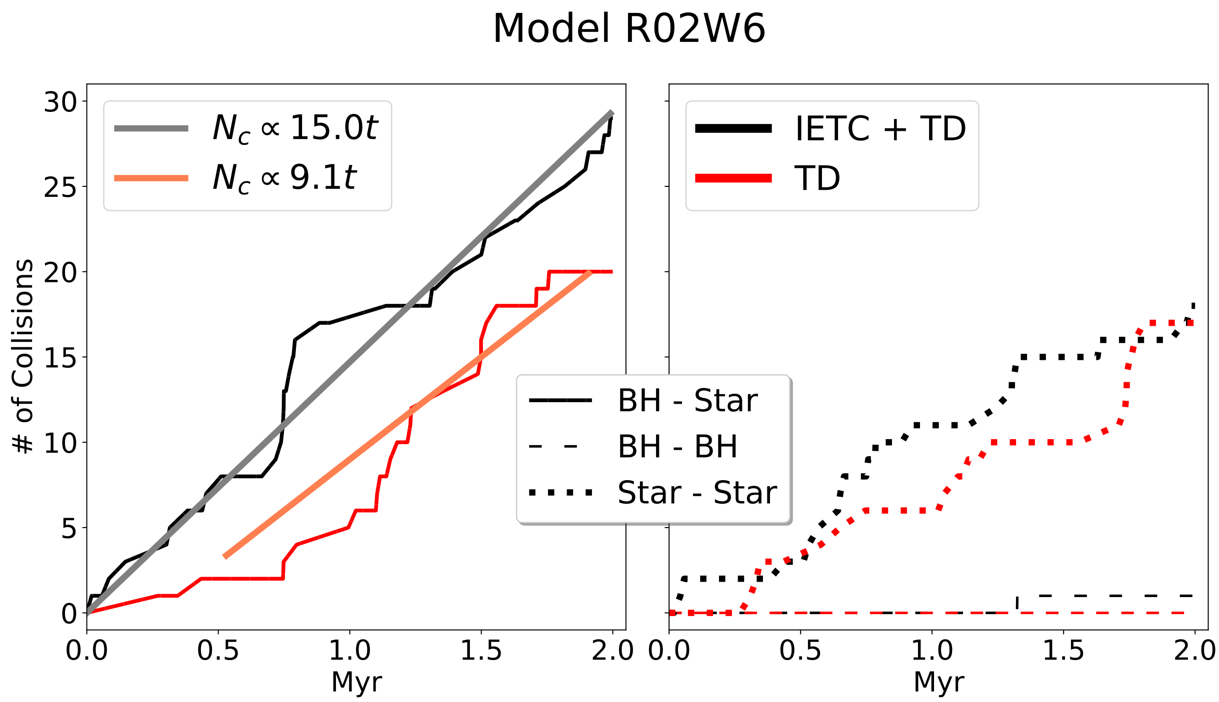

Figure 5.4: The plot shows the number of collisions as a function of time that occurred in the model R02W6 using the IETC prescription (in black) and without any tidal capture treatment (in red). The left panel reports the cumulative BH-star collisions (continued line); the IETC recipes appears to have increased the probability of star-BH collisions. This can be observed comparing the black and the red continuous lines. The trends of these lines are indicated with a grey and coral segment respectively. These trends estimate about 9 events per Myr for the simulation without any tidal treatments and 15 events per Myr for the simulation that include the instant emission prescription. The right panel indicates the cumulative star-star collisions (dotted line) and cumulative BH-BH collisions (dashed line) which as expected are not influenced by IETC.

Model Name	Instant Emission	Drag Force	# star-star	# BH-star	# BH-BH	Final Time[Myr]
R06W6	✓	✗	5	70	1	80
R06W6	✗	✓	6	30	0	20
R06W6	✗	✗	5	18	0	20
R02W6	✓	✗	17	29	1	2
R02W6	✗	✗	16	21	0	2
R06W6300	✓	✗	1	8	0	20
R06W6300	✗	✗	1	4	0	20
R05W9300	✓	✗	5	57	0	2
R05W9300	✗	✗	6	43	0	2

Table 5.2: Parameters of the cluster simulations: Instant Emission: indicates whether the instant emission tidal capture prescription was activated; Drag Force: indicates whether drag force treatment for tidal interactions was activated; # star-star: number of collisions between stars; # star-BH: number of collisions between a BH and a star; # BH-BH: number of collisions between BHs; Final Time: simulation termination time.

5.4 Results

In order to quantify the impact that TC events have on the total number of mergers in a simulation, we generate, for each model shown in Tab. 5.3, two realizations: one including the instant emission tidal capture prescription, and one without any prescription for tidal interactions. In addition, to test the validity of the instant emission assumption we run an extra realization of the model R06W6 that to mimic the effect of tidal interactions between two objects uses the drag force prescription. In total, we realized 9 simulations; the properties of these runs are summarized in Tab. 5.2.

We dedicate the second part of this section to the outcome of the simulations containing no IMBHs. We study how the collision rate is affected by the central density, paying particular attention to the quantitative effect that tidal capture prescriptions have on the overall number of BH-star collisions.

In the first part, we discuss and analyze the 4 realizations containing a central IMBH. with these runs, we aim to measure the mass growth rate of the IMBHs in clusters with different densities. We also investigate how the rate changes when tidal capture treatments are included.

5.5 Simulations with no central IMBH

5.5.1 Model R02W6

R02W6 is the most compact system we study in this work. Thanks to its initial high central density ($\rho_c \approx 10^7 \mathrm{M}_\odot/\mathrm{pc}^3$) even the realization with no tidal capture prescription activated (see red lines in Fig. 5.4) reports in total 21 BH - star collisions and 15 star-star collisions in just two years of evolution. The simulation that includes the possibility for a stellar BH to capture a star through the instant emission tidal capture prescription, register $\sim 30\%$ more BH - star collision.

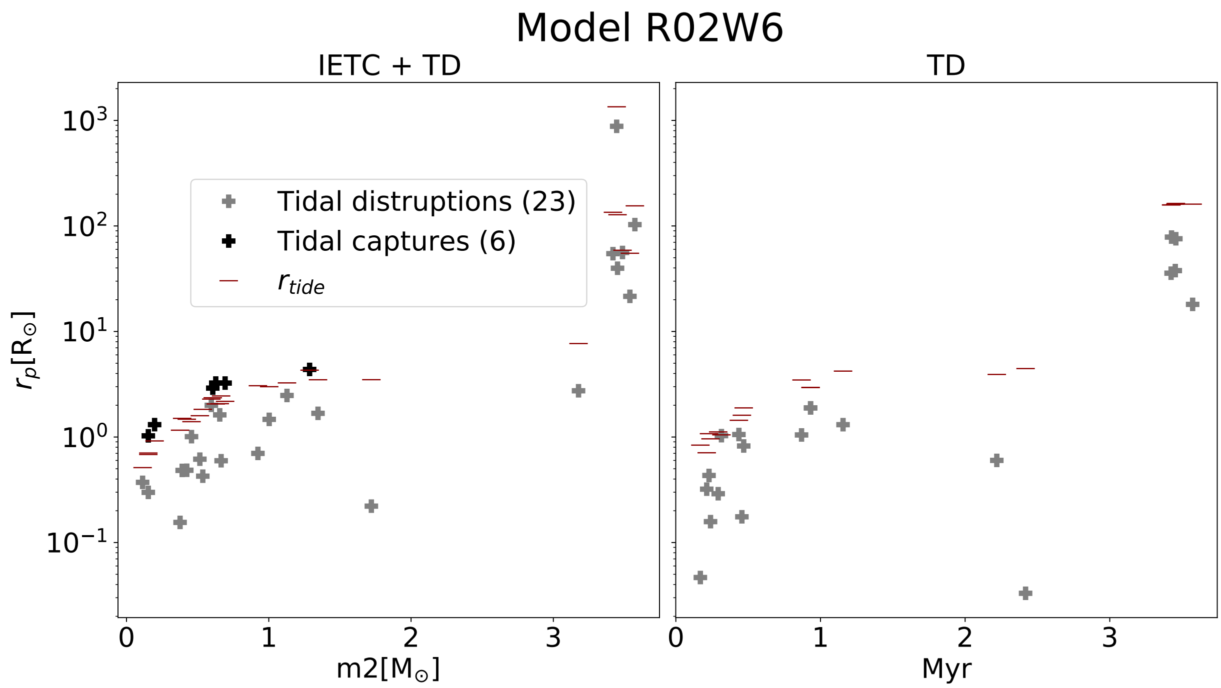

Figure 5.5: The large crosses (grey and black) indicate every BH-star collision registered in R02W6, showing the pericenter of the merger as well as the mass of the destroyed star. The plot also illustrates with small dark-red crosses the tidal radius of each event. Tidal captures are indicated in black while tidal disruptions are in grey. The left and the right panel report the result for the realization with and without tidal capture treatments respectively.

Since the capture is enabled only during close encounters between a star and a compact object the number of star-star collisions remain unchanged (see black lines in Fig. 5.4). As illustrated in the left panel of Fig. 5.5, R02W6 presents a total of 23 tidal disruption events and 6 tidal capture events. Most of the tidally captured stars are low mass stars, with masses $< 1.0\ M_\odot$, because they are the most common particle in the system and they have a larger tidal capture cross-section as explained in the previous section. Also, the tidally disrupted star tend to be relatively small, although few of them have had a mass above $> 3.0\ M_\odot$. These are the stars that reached the red giant phase, therefore their stellar radii and consequently their tidal radii increased by about two orders of magnitude.

5.5.2 Model R06W6

The merger rate reported in the R06W6 simulation with tidal prescription activate is roughly 1.5 events per Myr, as shown in the left panel of Fig. 5.6. Such collision rate is roughly an order of magnitude lower than the rate registered in R02W6. A similar difference in merger rate can be observed also when tidal capture prescriptions are deactivated, as can be observed comparing Figs. 5.4 and 5.6.

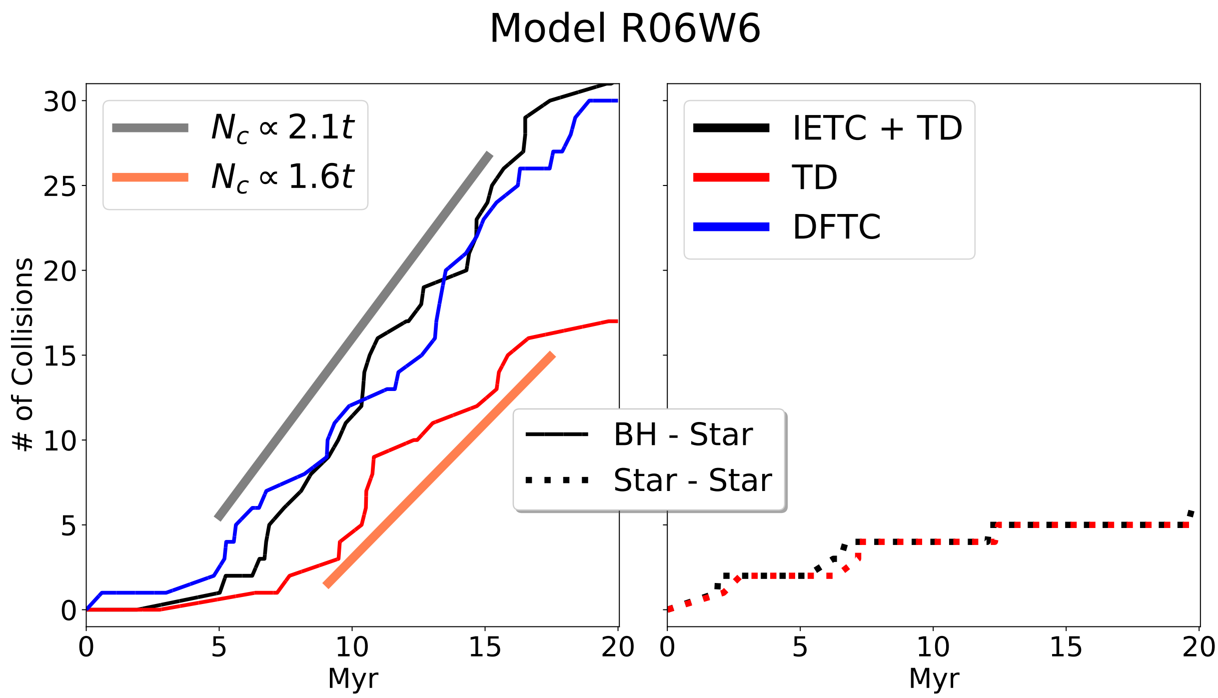

Figure 5.6: Same as Fig. 5.4 but for model R06W6. In addition, this plot reports in blue the result of the realization that used the model tidal interactions using a drag force.

This difference can be explained with the "n-sigma-v" estimate that approximate the collision rate with $n\Sigma v$, where n is the particle density, Σ is the interaction cross section and v is the typical velocity of the system, often approximated with the dispersion velocity: $v \approx \sigma$. For tidal disruptions and tidal captures the cross - section is proportional to the inverse square of the dispersion velocity: $\Sigma \propto \frac{1}{\sigma^2}$ (Lee & Ostriker, 1986; Heggie & Hut, 2003). Consequently, $n\Sigma v \propto \frac{n}{\sigma}$. Since the density of R02W6 is $\sim$ 25 times larger then the density in R06W6 (see Tab. 5.3), and its central dispersion velocity is a factor of $\sim$ 2 higher, it follows from the the "n-sigma-v" estimate that R02W6 should experience $\sim$ 12 more collisions per unit time, in good agreement with what observed in our numerical experiment. The left panel of Fig. 5.6 also illustrates the total number of collisions generated in the simulation that uses the tidal interaction drag force treatment. As expected the total number of BH-star collisions is substantially equal to the instant emission prescription. For these initial conditions, the two recipes appear to produce consistent outcomes. Nevertheless, they might produce divergent results when adopting initial conditions with a substantial fraction of primordial binaries, since, as we explained in the previous sections.

5.6 Simulations with central IMBH

The central IMBH of the model R05W6300 destroyed a total of 44 stars when tidal capture is not activated. With IETC included, the number of collision rises of 30% reaching 57 events (see

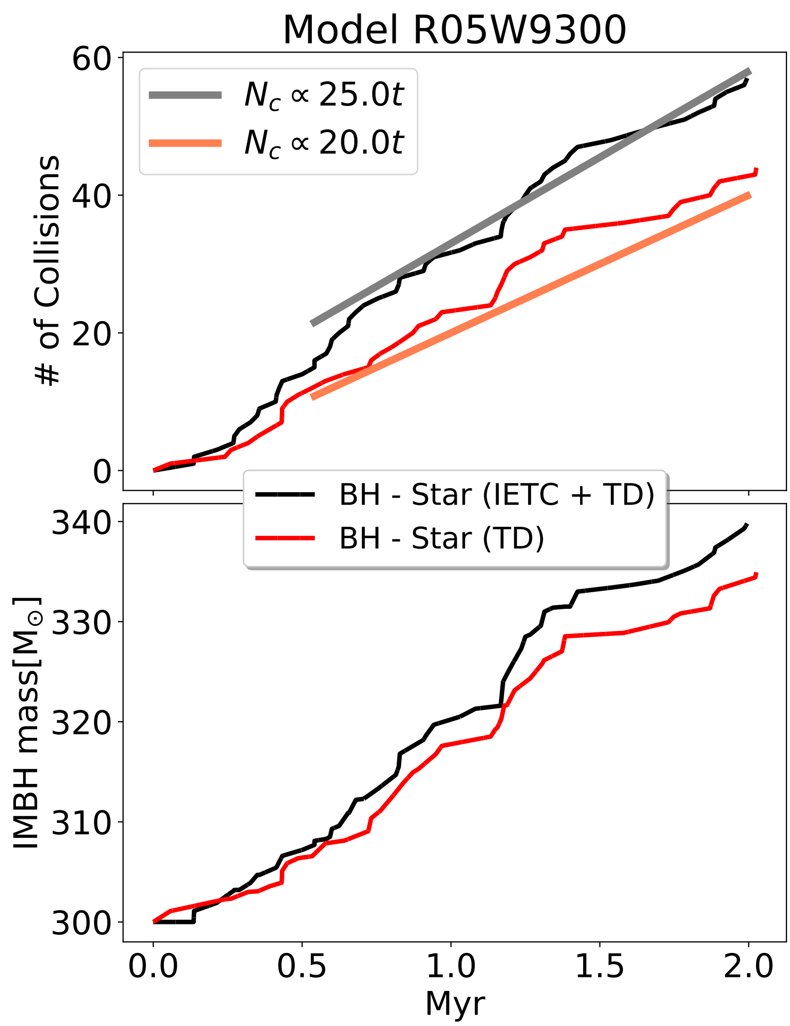

Figure 5.7: Upper panel: In black (red) the cumulative number of BH-star collisions reported in the realization of the model R05W9300 including instant emission tidal capture (without tidal treatments). Lower panel: The mass of the central IMBH as function of time for the same realization mentioned in the upper panel.

Fig. 5.7). However, among all these 57 mergers only 7 are induced by tidal capture and they all involve low mass stars, as shown in Fig. 5.8.

The difference in the number of collisions between the two models with and without tidal prescriptions is at least partly reflected in the mass growth of the IMBH as indicated in the bottom panel of Fig. 5.7. This panel shows that at the end of 2 Myr evolution, the IMBH in the realization with IETC, grows by about 40 $M_\odot$, just about 13% more than the realization with no tidal interaction prescription included. Despite the 30% difference in the number of collisions, the discrepancy in mass growth, between the two realizations, is less pronounced. This is because IETC does not enhance the probability of colliding with massive stars, which give the largest contribution to the final mass of the IMBH. We expect the difference in IMBH mass growth between the simulation with and without IETC to increase for long-term evolutions when all massive stars disappear from the system and only light stars remain.

We repeated the same numerical experiment for the less compact model R06W6300. After 20 Myr of evaluations, this model with IETC registered 9 IMBH - star collisions as illustrated in the

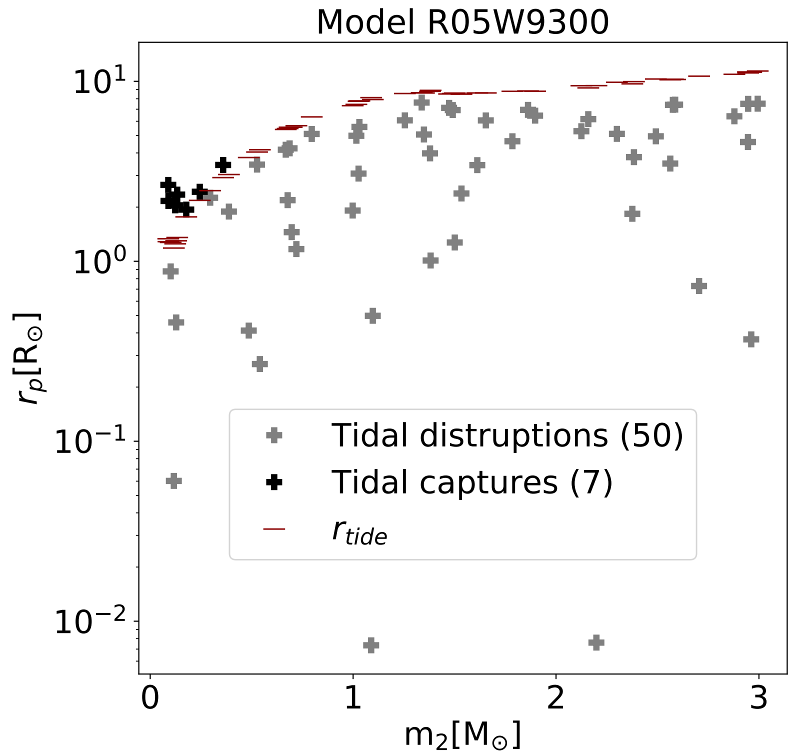

Figure 5.8: Same as Fig. 5.5 for the realization of the model R05W9300 that include tidal capture using the instant emission recipe.

upper panel of Fig. 5.9, of which 4 triggered by TC events. Despite the low number of collisions, from these preliminary results, it appears the collisions rate double when IETC switches on. This can also be observed comparing the black line with the red line in Fig. 5.9.

5.7 Conclusions

In this work, we investigated the role that tidal capture might have in the formation of massive BHs in very compact star clusters. We, therefore, include tidal capture prescriptions in the direct N-body code FROST (Rantala et al., 2021), and we realized a total of 9 simulations. In the first set of simulations, we initialized the clusters with a 200 Myr old stellar population. These systems contain about 450 stellar black holes surrounded by about 255500 low mass particles. The outcome of these runs indicates that tidal captures had a significant impact on the overall collision rate. In fact, The less-dense system, R06W6 registered, with tidal prescriptions included a total of 30 BH - star collisions in 20 Mrys, without tidal prescriptions only 18 mergers in the same period of time. Tidal captures increased also the collision rate of R02W6 by about 30%. However, non of these two models generate significantly massive BHs because the systems were not integrated for enough long time. We might observe the formation of massive objects for longer evolution. At the moment of writing this thesis, we are carrying on the runs and we aim to terminate the evolution after a few hundred Myr. The second set of simulations are initialized with a central IMBH of 300 $M_\odot$ enclosed by 256.000 low mass stars. This setup was chosen to investigate the mass growth of the central BH. The most compact model of this set, R05W9300, have shown

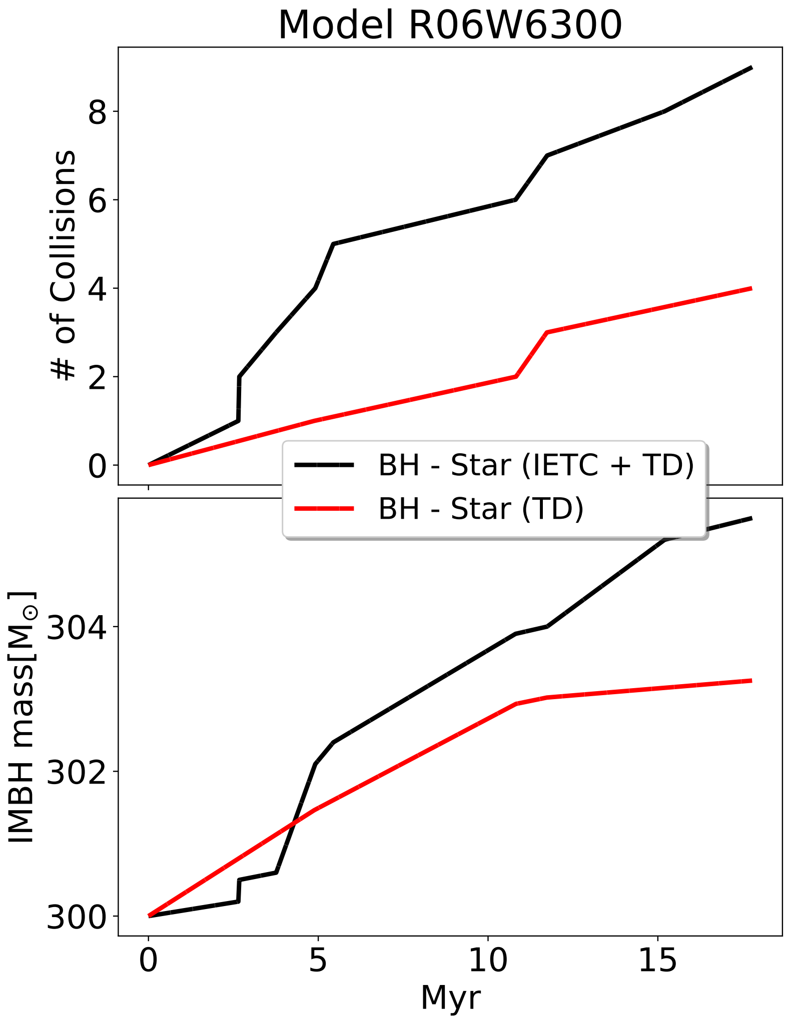

Figure 5.9: Same as Fig. 5.7 for the model R06W6300.

promising initial conditions for the magnification of the BH mass. In just 2 Myr the central object absorbed about 12% of its initial mass through tidal disruptions and tidal captures events. Also in this case we are continuing the run aiming to reach a few hundreds Myr of evolution.

Chapter 6

Conclusions

6.1 Summary

In this thesis, we explored the evolution of compact stellar environments by means of direct N-body simulations. At first, we focused on the early evolution of very dense low metallicity young star clusters. We generated 80 simulations of stellar systems with initial masses equal to $\sim 10^5$ M$_\odot$. To replicate the state of a star cluster right after gas removal, the systems are initially very compact ($R_h \leq 1.0$) and they are populated by $N = 110.000$ zero-age main-sequence stars with masses in the range between 0.08 M$_\odot$ and 100 M$_\odot$ sampled from the Kroupa (2001) IMF. About 10% of the stars are initialized in primordial binaries and the metallicity of the systems is set to $Z = 0.0002$. We evolved the clusters for 300 Myr using the code NBODY6++GPU. After the first $\sim$ 2 Myr the stellar systems experience a strong expansion due to stellar winds and supernova explosions. The strong expansion phase continues for about 10 Myr until the death of the most massive stars. Afterwards, the systems, driven by two-body relaxation effects, continue increasing their sizes but at a smaller rate. During the first $\sim$ 8 Myr, when the system is still dense, in almost all 80 runs very massive stars (VMSs) of $\gtrsim$ 300 M$_\odot$ form through a rapid series of stellar collisions. These VMSs, in some realizations, collide with low mass black holes (BHs). In 16 of these realizations, where BHs were allowed to absorb a large fraction of the stellar mass, these VMS - BH mergers lead to the formation of intermediate-mass BHs (IMBHs) with masses that range from 110 M$_\odot$ up to 350 M$_\odot$. In one simulation, an IMBH of 140 M$_\odot$ forms through a chain of three BHs coalescences with masses of 17 : 28, 25 : 45, 68 :70 M$_\odot$. According to the stellar evolution model adopted for this work, the two objects involved in the last collision (68-70 M$_\odot$) are about two times heavier than the most massive remnant obtainable by an isolated star. For this reason, the formation channel revealed by our simulations is particularly interesting, because it indicates a possible mechanism to generate BH collisions with both components significantly more massive than the heaviest stellar BH and it might explain the origin of some of the most recent gravitational wave events such as GW190521 and GW190929. Motivated by these interesting results we decided to repeat the same numerical experiment but using an updated model for stellar evolution. We therefore included in NBODY6++GPU (pulsation) pair-instability supernova prescriptions and metallicity-dependent stellar winds treatments. With these new recipes the stellar BH mass distribution span from 5 $M_\odot$ up to 45 $M_\odot$. We used the updated code to evolve, for 100 Myr, 16 realizations adopting the same initial conditions of the first set. These new runs reveal several mechanisms to efficiently repopulate the pulsation pair instability mas gap. They indicate that stellar-mass BHs can reach masses well above 45 $M_\odot$ through collisions with stars, collisions with other BHs, or through the direct collapse of VMSs. Simulations that allow a high accretion efficiency for star-BH mergers reveal formation scenarios for GW190521-like events; in one realization the two colliding components reached respectively $\sim$ 80 $M_\odot$ and $\sim$ 70 $M_\odot$ entirely by star-BH mergers. This IMBH formation path is independent of gravitational recoil and therefore conceivable in dense stellar systems with low escape velocities. Another realization reported a chain of mergers, involving 2 BH-star collisions and 1 BH-BH coalescence, that led $\sim$ 90 $M_\odot$ and $\sim$ 60 $M_\odot$ BHs to collide. We estimated statistically the importance of the gravitational recoil for this event and we showed that, if the stellar BH involved in the chain of mergers are slowly rotating ($S \sim 0.1$), the final merger has a non-negligible probability to occur. Finally, is relevant to mention that one simulated cluster reported the formation of an IMBH binary (153 $M_\odot$,173 $M_\odot$) with an estimated coalescence time smaller than the Hubble time.

The first two sets of simulations have been evolved using NBODY6++GPU, which currently is the only direct N-body code capable of generating simulations of massive star clusters of realistic sizes, following the gravitational and stellar evolution with high accuracy. However, using this code for more than three years, we encountered several technical issues mainly due to the complicated coding design of this software. NBODY6++GPU is written primarily in Fortran70, based on codes developed in the late 1960s/early 1970s. Over the years many functionalities have been added, such as stellar evolution models and prescription to include external potentials. However, these new layers of code that have overlapped over the years have not always been added in the most organic way. As a result, it is often difficult to incorporate new updates or include new physical processes in NBODY6++GPU. In addition, the code is sometimes incompatible with modern compilers, and simulations of very dense systems are often delicate and unstable. Therefore, we have decided to run the last set of simulations using the code FROST. This software, written in modern C and parallelized with a hybrid CUDA-MPI scheme, has the proven ability to follow the gravitational evolution of compact stellar systems up to $N = 10^6$ particles with high accuracy. To handle few body close encounters it uses the logarithmic Hamiltonian regularization method which includes post-Newtonian correction up to 2.5 order. This new code does not yet have built-in prescriptions to model the evolution of binary stars. However, it can efficiently evolve very compact and dense clusters. We incorporated tidal capture (TC) treatments in FROST and we evolved 9 simulations of $N = 256.000$ particles and half mass radii ≤ 0.6 pc to investigate the role that TC events play in the formation of massive BHs. We generated 4 initial conditions models. In order to focus our study exclusively on the effect of TC, and avoid complications due to stellar evolution, none of these models contains stars more massive than $\gtrsim 8$ $M_\odot$. Two models contain about 450 stellar BHs embedded in a stellar system of 200 Myr old stars with masses that range between 0.08 $M_\odot$ and 3.5 $M_\odot$. For the run based on these initial conditions, our preliminary results show that TC events increased the BH-star merger rate by more than 30%. The other two models are initialized with a central IMBH of 300 $M_\odot$ surrounded by low mass stars. In such configuration the densest simulated star cluster reveals an IMBH mass growth of about 20 $M_\odot$ /Myr; TC events contribute about 13 % of this growth rate. These results, although very promising, are still partial and the simulations, which are very expensive, are still in progress and will end after at least 100 Myr of evolution.

6.2 Future prospects

Our numerical experiments show that it is not uncommon for compact young star clusters to repopulate the (P)PSN mass gap dynamically without imposing any non-conventional stellar evolution scenario. They also indicate dynamical pathways to generate mergers between BHs lying in this mass range. In future work, we aim to generate a much larger sample of compact star cluster simulations and characterize the properties of such BH mergers. Our goal is to obtain robust statistical distributions of spins, eccentricities and masses of these events. We expect such distributions can have broad implications not only for GW astrophysics but also for stellar physics. For instance, if future observations suggest that the mergers involving BHs in the mass gap do not match the expected characteristic of collisions produced in star clusters, then the existence of BHs in the mass gap would indicate that our current stellar evolution models for massive stars need to be rectified.

The N-body code we would like to use for our future runs is FROST. As we mentioned earlier, before being able to evolve simulations of realistic star clusters, FROST needs to be coupled with a synthetic binary stellar evolution package. Therefore, our first future project is to incorporate a binary stellar evolution model, such as BSE or equivalent, in FROST. The inclusion of stellar evolution recipes must be done in an organic way. In order to facilitate the eventual updating of stellar evolution, the stellar modules must be well separated from the original code.

Another important outcome observed in our investigation is the formation of massive BHs in the IMBH mass range ($\gtrsim$ 100 $M_\odot$) originating from previous BH and stellar mergers. Such assembly recalls the dynamical formation path of supermassive BHs. Our results might be giving us a glance on how the very first seeds of supermassive BHs might have formed. This scenario deserves to be explored in greater depth through the numerical exploration of stellar systems with densities comparable to the nuclear star clusters ($\rho \approx 1.1 \times 10^7\ M_\odot/pc^3$). We started exploring such systems numerically in the last project of this thesis. Preliminary results are already very promising, but it is necessary to evolve the simulations for a longer time and then generate simulations with a number of particles $N > 10^6$ to resemble the real dynamics of small nuclear star clusters.

Appendices

Appendix A

Matrix exponential form of the evolution operator

Let $H(z)$ be the Hamiltonian of a system whose state is described by the parameter $z = (q, p)$, a single variable that denotes the canonical coordinates. Let, in addition, define the Hamiltonian operator $\hat{H}(z) := \{z, H\}$, where $\{z, H\}$ = are the Poisson bracket. The latter, in canonical coordinates, are defined as $\{A, B\} := \frac{\partial A}{\partial q}\frac{\partial B}{\partial p} - \frac{\partial B}{\partial q}\frac{\partial A}{\partial p}$, where $A(q, p)$ and $B(q, p)$ are two generic functions of p and q. Taking advantage of this definition, the equation of motion of the system, described by $H(z)$, can be expressed with the single expression:

$$\frac{dz}{dt} = \hat{H}(z) \tag{A.1}$$

The formal solution of this equation is given by the following matrix exponential:

$$z(t) = \exp(t\hat{H})(z(0)) \tag{A.2}$$

In order to show that the expression A.2 is the actual solution of eq. A.1, we need to use the actual definition of the matrix exponential:

$$\exp(t\hat{H})(z(0)) := \sum_{n=0}^{\infty} \frac{1}{n!}\hat{H}^n(z(0))t^n. \tag{A.3}$$

From this, it follows that:

$$\frac{dz}{dt} = \frac{d}{dt}\left[\exp(t\hat{H})(z(0))\right] = \hat{H}\exp(t\hat{H})(z(0)) = \hat{H}(z) \tag{A.4}$$

The equation eq. A.2 represents the time evolution of the state of the system z from the instant 0 to the instant t. Hence, the expression $\exp(t\hat{H})$ represents the time evolution operator of the system associated with the Hamiltonian H. Due to its exponential form, it can be easily manipulated in analytical expressions, and, as we see in the appendix C it turns out to be very useful to develop an analytical framework to study symplectic integrators.

Appendix B

A brief introduction to symplectic integrators

Let us assume we are interested on finding a numerical approximation of a generic ordinary differential equation of the form:

$$\frac{dz}{dt} = f(z) \tag{B.1}$$

The most basic numerical method we can apply to find the approximated solution is the Euler method. This technique approximates the evolution of the function $z(t)$ with a function $\widetilde{z}$ that follows the 1^{th} order Taylor expansion of the real solution:

$$\widetilde{z}(t_0 + dt) = z_0 + \frac{dz}{dt}dt \tag{B.2}$$

where z_0 is the value of $z(t)$ at $t = t_0$

To investigate the performance of this method we use it to integrate the harmonic oscillator, whose Hamiltonian is $H = \frac{p^2}{2} + \frac{q^2}{2}$ and the equation of motion are:

$$\begin{cases} \frac{dq}{dt} = p \\ \frac{dp}{dt} = -q \\ q(t=0) = q_0 \\ p(t=0) = p_0 \end{cases} \tag{B.3}$$

The integrator predicts the evolution of the system computing the coordinate at step $i + 1$ using the coordinate at step i as follow:

$$\begin{cases} q_{i+1} = q_i + p_i dt \\ p_{i+1} = p_i - q_i dt \end{cases} \tag{B.4}$$

A simple numerical experiment would show that for sufficiently small values of dt the method approximate the solution fairly well for the first few oscillations. However, the numerical solution becomes unreliable for long-time integration. This is because the Euler Method leads to unbounded artificial excitation of the initial energy. We can observe that simply computing the energy of the approximated system after N integration steps is:

$$E_N \propto p_N^2 + q_N^2 = (1 + dt^2)^N (q_0^2 + p_0^2) \propto (1 + dt^2)^N E_N \tag{B.5}$$

however small dt may be E_N will diverge from E_0 for sufficiently large N. A similar consideration applies to the well-known classical 4th order Runge-Kutta method. If used to evolve the system B.3 this scheme would lead to unreliable long-time integration results because it generates monotonous artificial damping that comes from the method itself. In general, for long-time integration, we cannot rely on numerical methods with unbounded energy errors. Ideally, we would like to evolve an energy-conserving system with a numerical scheme that does conserve energy as well. Unfortunately for non-integrable systems, such integrator cannot be built (see Zhong & Marsden, 1988). Nevertheless, it is still possible to find numerical schemes that provide good and reliable performance for long-term integrations. Consider for example the following variation of the Euler scheme, called symplectic Euler method[1]:

$$\begin{cases} q_{i+1} = q_i + p_i dt \\ p_{i+1} = p_i - q_{i+1} dt \end{cases} \tag{B.6}$$

with such a scheme the energy error does not diverge over time. To understand why we first observe that from B.6 follows:

$$p_N^2 + q_N^2 + dt q_N p_N = p_{N-1}^2 + q_{N-1}^2 + dt q_{N-1} p_{N-1} = p_0^2 + q_0^2 + dt q_0 p_0 \tag{B.7}$$

Therefore the phase-space trajectories of the approximated solution must lie on the ellipse described by equation B.7. The artificial error generated by the integrator is bounded and the approximated energy oscillates around the true energy with an error proportional to dt, independently on the number of steps performed by the integrator.

The Symplectic Euler method belongs to the class of symplectic integrators. Such integrators have the great benefit of producing bounded energy numerical error because (as we will explain more in detail in the appendix C) they describe the exact evolution of a surrogate Hamiltonian close to the original one. For this reason, they can provide robust approximations also for long-time integrations.

[1]We evidence in red what differs the symplectic Euler method from the standard Euler method.

Appendix C

How to Build a symplectic integrator

In this appendix, we show an explicit method to build a symplectic integrator for separable Hamiltonians. A separable Hamiltonin takes the form: $H(q, p) = H_A(q, p) + H_B(q, p)$ where both H_A and H_B can be integrated in the absence of the other part. Under the assumption that H_A and H_B are both symplectic, it is easy to see that a generic product $\exp(aH_A)\exp(bH_B)\exp(cH_A)$... with a, b, c arbitrary numbers, it is also symplectic because the combination of two symplectic maps is a symplectic map itself (see Hairer et al., 2003). To make sure that the integrator is of nth order we need to find a set of real number that satisfies:

$$\exp(H_A + H_B) = \prod_{i=1}^{k} \exp(c_i dt H_A)\exp(d_i dt H_B) + O(dt^n). \tag{C.1}$$

In principle this problem can be solved expanding in power of dt the left and right side of the equation and choosing the real coefficients to equate each term of equal power. An elegant procedure, described in Yoshida (1991), employes the CBH formulas to find numerical coefficients c_i, d_i and add the extra condition that the numerical integrator must be time-symmetric. Following this procedure it is easy to find the leap-frog integrator:

$$\exp(H_A + H_B) \approx \exp(\frac{1}{2}dt H_A)\exp(dt H_B)\exp(\frac{1}{2}dt H_A) \tag{C.2}$$

that is a symplectic time-symmetric, 2nd order integrator.

Appendix D

Building a the Leap Frog integrator for the Kepler Hamiltonian

Since the Hamiltonian of the Kepler problem $H(q,p) = \frac{p^2}{2\mu} - \frac{M\mu}{q}$ is separable, the leap-frog integrator, we described in the previous appendix, can be used to integrate its equation of motion. A possible way to construct the integrator for such system is:

$$\exp\left(dtH(q,p)\right) \approx \exp\left(\frac{dt}{2}\frac{p^2}{2\mu}\right)\exp\left(-dt\frac{M\mu}{q}\right)\exp\left(\frac{dt}{2}\frac{p^2}{2\mu}\right) \tag{D.1}$$

To understand how this operator concretely acts on the state (q_0, p_0) let us define the "kick" K and the "drift" D operators as follow:

$$K := \exp\left(-dt\frac{M\mu}{q}\right) \tag{D.2}$$

$$D := \exp\left(\frac{1}{2}dt\frac{p^2}{2\mu}\right). \tag{D.3}$$

Applying K to initial state (q_0, p_0) and using the definitions illustrated in the appendix A we obtain effect that such operetor has on the state:

$$\exp\left(-dt\frac{M\mu}{q}\right)(q_0, p_0) = \sum_{n=0}^{\infty}\frac{1}{n!}\left(\frac{M\mu}{q}\right)^n(q_0, p_0)dt^n \approx (q_0, p_0 - dt\frac{M\mu}{q_0^2}) \tag{D.4}$$

in words K, generate a shift in the space of momentum provoking a change in the initial momentum of the particle. Similarly the drift operator D when applied to the state (q_0, p_0) shifts the particle position:

$$\exp\left(-dt\frac{p^2}{2\mu}\right)(q_0, p_0) \approx (q_0 - dt\frac{p_0}{\mu}, p_0). \tag{D.5}$$

The leap-frog we just descried $\exp\left(dtH(q,p)\right) \approx DKD$ is also known as the "drift-kick-drift" algorithm. Another possible way to approximate the time operator of the Keplerian Hamiltonian is by means of $\exp\left(dtH(q,p)\right) \approx KDK$ known as the "kick-drift-kick" leap-frog integrator.

Bibliography

G. D., Shapiro S. L., 1987, ApJ, 321, 199

Aarseth S. J., 1999, PASP, 111, 1333

Aarseth S. J., 2003, Gravitational N-Body Simulations

Aarseth S. J., 2012, MNRAS, 422, 841

Abbate F., Possenti A., Ridolfi A., Freire P. C. C., Camilo F., Manchester R. N., D'Amico N., 2018, MNRAS, 481, 627

Abbott B. P., et al., 2016, Physical Review, 116, 061102

Abbott B. P., et al., 2017, Physical Review, 119, 161101

Abbott B. P., et al., 2019, Physical Review X, 9, 031040

Abbott R., et al., 2020, Physical Review, 125, 101102

Agarwal B., Khochfar S., Johnson J. L., Neistein E., Dalla Vecchia C., Livio M., 2012, MNRAS, 425, 2854

Applegate J. H., 1986, ApJ, 301, 132

Arca Sedda M., Benacquista M., 2019, MNRAS, 482, 2991

Arca-Sedda M., Capuzzo-Dolcetta R., 2019, MNRAS, 483, 152

Arca-Sedda M., Gualandris A., 2018, MNRAS, 477, 4423

Arca-Sedda M., Amaro-Seoane P., Chen X., 2020, arXiv e-prints, p. arXiv:2007.13746

Arca Sedda M., Rizzuto F. P., Naab T., Ostriker J., Giersz M., Spurzem R., 2021, arXiv e-prints, p. arXiv:2105.07003

Askar A., Davies M. B., Church R. P., 2020, arXiv e-prints, p. arXiv:2006.04922

Bahcall J. N., Wolf R. A., 1976, ApJ, 209, 214

Baker J. G., Boggs W. D., Centrella J., Kelly B. J., McWilliams S. T., Miller M. C., van Meter J. R., 2008, ApJL, 682, L29

Banerjee S., 2020, arXiv e-prints, 639, arXiv:2004.07382

Banerjee S., 2021, MNRAS, 500, 3002

Banerjee S., Belczynski K., Fryer C. L., Berczik P., Hurley J. R., Spurzem R., Wang L., 2019, arXiv e-prints, p. arXiv:1902.07718

Baumgardt H., 2017, MNRAS, 464, 2174

Baumgardt H., Hilker M., 2018, MNRAS, 478, 1520

Baumgardt H., Hut P., Makino J., McMillan S., Portegies Zwart S., 2003, ApJL, 582, L21

Baumgardt H., Hopman C., Portegies Zwart S., Makino J., 2006, MNRAS, 372, 467

Baumgardt H., Sollima A., Hilker M., 2020, in Bragaglia A., Davies M., Sills A., Vesperini E., eds, IAU Symposium Vol. 351, IAU Symposium. pp 400–403, doi:10.1017/s1743921319007695

Becker D., Spera M., Kremer K., Rasio F., 2020, in American Astronomical Society Meeting Abstracts #235. p. 369.10

Begelman M. C., Rees M. J., 1978, MNRAS, 185, 847

Begelman M. C., Volonteri M., Rees M. J., 2006, MNRAS, 370, 289

Belczynski K., 2020, ApJL, 905, L15

Belczynski K., Kalogera V., Bulik T., 2002, ApJ, 572, 407

Belczynski K., Kalogera V., Rasio F. A., Taam R. E., Zezas A., Bulik T., Maccarone T. J., Ivanova N., 2008, ApJS, 174, 223

Belczynski K., Bulik T., Fryer C. L., Ruiter A., Valsecchi F., Vink J. S., Hurley J. R., 2010, ApJ, 714, 1217

Belczynski K., et al., 2016, AAP, 594, A97

Belczynski K., Ryu T., Perna R., Berti E., Tanaka T. L., Bulik T., 2017, MNRAS, 471, 4702

Blanchet L., Buonanno A., Faye G., 2006, Physical Review D, 74, 104034

Bonnell I. A., Bate M. R., 2006, MNRAS, 370, 488

Bonnerot C., Lu W., 2020, MNRAS, 495, 1374

Brem P., Amaro-Seoane P., Spurzem R., 2013, MNRAS, 434, 2999

Brightman M., et al., 2016, ApJ, 829, 28

Burrows A., Vartanyan D., 2021, NAT, 589, 29

Casares J., Jonker P. G., 2014, SSR, 183, 223

Chernoff D. F., Shapiro S. L., 1987, ApJ, 322, 113

Chernoff D. F., Weinberg M. D., 1990, ApJ, 351, 121

Chin S. A., 1997, Physics Letters A, 226, 344

Chin S. A., Chen C. R., 2005, Celestial Mechanics and Dynamical Astronomy, 91, 301

Cohn H., 1980, ApJ, 242, 765

Colbert E. J. M., Mushotzky R. F., 1999, ApJ, 519, 89

Crowther P. A., Schnurr O., Hirschi R., Yusof N., Parker R. J., Goodwin S. P., Kassim H. A., 2010, MNRAS, 408, 731

Dall'Amico M., Mapelli M., Niccolò Di Carlo U., Bouffanais Y., Rastello S., Santoliquido F., Ballone A., Arca Sedda M., 2021, arXiv e-prints, p. arXiv:2105.12757

Davies M. B., 2015, Formation Channels for Blue Straggler Stars. p. 203, doi:10.1007/978-3-662-44434-4_9

Davies M. B., Piotto G., de Angeli F., 2004, MNRAS, 349, 129

Dehnen W., 2017, MNRAS, 472, 1226

Di Carlo U. N., Giacobbo N., Mapelli M., Pasquato M., Spera M., Wang L., Haardt F., 2019, MNRAS, 487, 2947

Di Carlo U. N., et al., 2020, MNRAS, 498, 495

Di Carlo U. N., et al., 2021, arXiv e-prints, p. arXiv:2105.01085

DiCarlo U. N., et al., 2020, arXiv e-prints, p. arXiv:2004.09525

Edri H., Rafter S. E., Chelouche D., Kaspi S., Behar E., 2012,] 10.1088/0004-637x/756/1/73

Eggleton P. P., Fitchett M. J., Tout C. A., 1989, ApJ, 347, 998

Eggleton P. P., Fitchett M. J., Tout C. A., 1990, ApJ, 354, 387

Elson R. A. W., Fall S. M., Freeman K. C., 1987, ApJ, 323, 54

Farmer R., Renzo M., de Mink S. E., Marchant P., Justham S., 2019, ApJ, 887, 53

Farrell S. A., Webb N. A., Barret D., Godet O., Rodrigues J. M., 2009, NAT, 460, 73

Feng H., Soria R., 2011, NAR, 55, 166

Figer D. F., 2005, NAT, 434, 192

Filippenko A. V., Ho L. C., 2003, ApJL, 588, L13

Fowler W. A., Hoyle F., 1964, ApJS, 9, 201

Fragione G., Ginsburg I., Kocsis B., 2018, ApJ, 856, 92

Fragione G., Loeb A., Rasio F. A., 2020, ApJL, 902, L26

Fragos T., McClintock J. E., 2015, ApJ, 800, 17

Freitag M., Rasio F. A., Baumgardt H., 2006, MNRAS, 368, 121

Fryer C. L., Belczynski K., Wiktorowicz G., Dominik M., Kalogera V., Holz D. E., 2012, ApJ, 749, 91

Fujii M. S., Saitoh T. R., Hirai Y., Wang L., 2021, arXiv e-prints, p. arXiv:2103.02829

Fukushige T., Heggie D. C., 1995, MNRAS, 276, 206

Fukushima H., Yajima H., 2021, arXiv e-prints, p. arXiv:2104.10892

Fuller J., Ma L., 2019, ApJL, 881, L1

Fürst F., et al., 2016, ApJL, 831, L14

Gayathri V., et al., 2020, arXiv e-prints, p. arXiv:2009.05461

Gebhardt K., Rich R. M., Ho L. C., 2002, ApJL, 578, L41

Gebhardt K., Rich R. M., Ho L. C., 2005, ApJ, 634, 1093

Gerosa D., Hébert F., Stein L. C., 2018, Physical Review D, 97, 104049

Gessner A., Janka H.-T., 2018, ApJ, 865, 61

Giacobbo N., Mapelli M., Spera M., 2018, MNRAS, 474, 2959

Gieles M., Heggie D. C., Zhao H., 2011, MNRAS, 413, 2509

Gieles M., et al., 2018, MNRAS, 478, 2461

Giersz M., Heggie D. C., 1994, MNRAS, 268, 257

Giersz M., Heggie D. C., 1996, MNRAS, 279, 1037

Giersz M., Spurzem R., 1994, MNRAS, 269, 241

Giersz M., Leigh N., Hypki A., Lützgendorf N., Askar A., 2015, MNRAS, 454, 3150

Gladstone J. C., 2013, MEMSAI, 84, 629

Glebbeek E., Gaburov E., de Mink S. E., Pols O. R., Portegies Zwart S. F., 2009, AAP, 497, 255

Gräfener G., Hamann W. R., 2008, AAP, 482, 945

Gürkan M. A., Freitag M., Rasio F. A., 2004, ApJ, 604, 632

Gürkan M. A., Fregeau J. M., Rasio F. A., 2006, ApJL, 640, L39

Gutermuth R. A., Megeath S. T., Pipher J. L., Williams J. P., Allen L. E., Myers P. C., Raines S. N., 2005, ApJ, 632, 397

Hairer E., Lubich C., Wanner G., 2003, Acta Numerica, 12, 399

Heger A., Fryer C. L., Woosley S. E., Langer N., Hartmann D. H., 2003, ApJ, 591, 288

Heggie D. C., 1974, Celestial Mechanics, 10, 217

Heggie D. C., 1975, MNRAS, 173, 729

Heggie D., Hut P., 2003, The Gravitational Million-Body Problem: A Multidisciplinary Approach to Star Cluster Dynamics

Hobbs G., Lorimer D. R., Lyne A. G., Kramer M., 2005,] 10.1111/j.1365-2966.2005.09087.x

Hurley J. R., Bekki K., 2008, MNRAS, 389, L61

Hurley J. R., Pols O. R., Tout C. A., 2000, MNRAS, 315, 543

Hurley J. R., Tout C. A., Pols O. R., 2002,] 10.1046/j.1365-8711.2002.05038.x

Hut P., Bahcall J. N., 1983, ApJ, 268, 319

Ishii M., Ueno M., Kato M., 1999, PASJ, 51, 417

Kaaret P., Prestwich A. H., Zezas A., Murray S. S., Kim D. W., Kilgard R. E., Schlegel E. M., Ward M. J., 2001, MNRAS, 321, L29

Kaaret P., Feng H., Roberts T. P., 2017, ARAA, 55, 303

Kamlah A. W. H., et al., 2021, arXiv e-prints, p. arXiv:2105.08067

Kim M., López K. M., Jonker P. G., Ho L. C., Im M., 2020, MNRAS, 493, L76

Kimball C., et al., 2020, arXiv e-prints, p. arXiv:2011.05332

King I. R., 1966, AJ, 71, 64

King A., Lasota J.-P., 2020, MNRAS,

Kinugawa T., Nakamura T., Nakano H., 2021, MNRAS, 501, L49

Kızıltan B., Baumgardt H., Loeb A., 2017, NAT, 545, 510

Klessen R. S., 2001, ApJ, 556, 837

Kochanek C. S., 1992, ApJ, 385, 604

Koliopanos F., 2017, in XII Multifrequency Behaviour of High Energy Cosmic Sources Workshop (MULTIF2017). p. 51 (arXiv:1801.01095)

Kong A. K. H., 2007, ApJ, 661, 875

Kormendy J., Ho L. C., 2013, ARAA, 51, 511

Kozai Y., 1962, AJ, 67, 591

Kremer K., et al., 2020, arXiv e-prints, 903, arXiv:2006.10771

Kroupa P., 2001, MNRAS, 322, 231

Krumholz M. R., 2015, The Formation of Very Massive Stars. p. 43, doi:10.1007/978-3-319-09596-7_3

Kulier A., Ostriker J. P., Natarajan P., Lackner C. N., Cen R., 2015, ApJ, 799, 178

Küpper A. H. W., Maschberger T., Kroupa P., Baumgardt H., 2011, MNRAS, 417, 2300

Kustaanheimo P., Stiefel E., 1965, Crelles Journal, 71, 276

Lahén N., Naab T., Johansson P. H., Elmegreen B., Hu C.-Y., Walch S., 2019, ApJL, 879, L18

Lahén N., Naab T., Johansson P. H., Elmegreen B., Hu C.-Y., Walch S., Steinwandel U. P., Moster B. P., 2020, ApJ, 891, 2

Law-Smith J., Guillochon J., Ramirez-Ruiz E., 2019, ApJL, 882, L25

Lee H. M., 1987, ApJ, 319, 801

Lee H. M., Ostriker J. P., 1986, ApJ, 310, 176

Lee H. M., Ostriker J. P., 1993, ApJ, 409, 617

Leigh N., Giersz M., Webb J. J., Hypki A., De Marchi G., Kroupa P., Sills A., 2013, MNRAS, 436, 3399

Lidov M. L., 1962, PLANSS, 9, 719

Liu B., Bromm V., 2020, ApJL, 903, L40

Liu J.-F., Bregman J. N., Bai Y., Justham S., Crowther P., 2013, NAT, 503, 500

Longmore S. N., et al., 2014, in Beuther H., Klessen R. S., Dullemond C. P., Henning T., eds, Protostars and Planets VI. p. 291 (arXiv:1401.4175), doi:10.2458/azu_uapress_9780816531240-ch013

Lousto C. O., Zlochower Y., 2009, Physical Review D, 79, 064018

Lu W., Bonnerot C., 2020, MNRAS, 492, 686

Luo Y., Shlosman I., Nagamine K., Fang T., 2020, MNRAS, 492, 4917

Lützgendorf N., et al., 2013, AAP, 552, A49

Lynden-Bell D., 1999, Physica A Statistical Mechanics and its Applications, 263, 293

Lynden-Bell D., Eggleton P. P., 1980, MNRAS, 191, 483

Lynden-Bell D., Wood R., 1968, MNRAS, 138, 495

Madau P., Rees M. J., 2001, ApJL, 551, L27

Maeder A., Meynet G., 2000, AAP, 361, 159

Mapelli M., 2016, MNRAS, 459, 3432

Mapelli M., 2021, arXiv e-prints, p. arXiv:2106.00699

Mapelli M., Giacobbo N., Ripamonti E., Spera M., 2017, MNRAS, 472, 2422

Mapelli M., Santoliquido F., Bouffanais Y., Arca Sedda M., Giacobbo N., Artale M. C., Ballone A., 2020, arXiv e-prints, p. arXiv:2007.15022

Mapelli M., et al., 2021, MNRAS, 505, 339

Mardling R. A., 1996, in Wijers R. A. M. J., Davies M. B., Tout C. A., eds, NATO Advanced Science Institutes (ASI) Series C Vol. 477, NATO Advanced Science Institutes (ASI) Series C. p. 81 (arXiv:astro-ph/9512036)

Mardling R. A., Aarseth S. J., 2001, MNRAS, 321, 398

Marks M., Kroupa P., 2012, AAP, 543, A8

Matsumoto H., Tsuru T. G., 1999, PASJ, 51, 321

Matsumoto H., Tsuru T. G., Koyama K., Awaki H., Canizares C. R., Kawai N., Matsushita S., Kawabe R., 2001, ApJL, 547, L25

McCrady N., Gilbert A. M., Graham J. R., 2003, ApJ, 596, 240

McMillan S. L. W., 2008, Classical and Quantum Gravity, 25, 114007

McMillan S. L. W., Hut P., 1996, ApJ, 467, 348

Mengel S., Tacconi-Garman L. E., 2007, AAP, 466, 151

Metzger B. D., Stone N. C., 2016, MNRAS, 461, 948

Mezcua M., 2017, International Journal of Modern Physics D, 26, 1730021

Mezcua M., Roberts T. P., Sutton A. D., Lobanov A. P., 2013, MNRAS, 436, 3128

Mezcua M., Roberts T. P., Lobanov A. P., Sutton A. D., 2015, MNRAS, 448, 1893

Mikkola S., Aarseth S. J., 1993, Celestial Mechanics and Dynamical Astronomy, 57, 439

Mikkola S., Aarseth S. J., 1998, NA, 3, 309

Miller S., Callister T. A., Farr W. M., 2020, ApJ, 895, 128

Moe M., Di Stefano R., 2017, ApJS, 230, 15

Morawski J., Giersz M., Askar A., Belczynski K., 2018, MNRAS, 481, 2168

Nakada Y., 1978, PASJ, 30, 57

Nash P. E., Monaghan J. J., 1978, MNRAS, 184, 119

Nitadori K., Aarseth S. J., 2012, MNRAS, 424, 545

Noyola E., Gebhardt K., Bergmann M., 2008, ApJ, 676, 1008

Noyola E., Gebhardt K., Kissler-Patig M., Lützgendorf N., Jalali B., de Zeeuw P. T., Baumgardt H., 2010, ApJL, 719, L60

Oppenheimer J. R., Snyder H., 1939, Physical Review, 56, 455

Özel F., Psaltis D., Narayan R., McClintock J. E., 2010, ApJ, 725, 1918

Panamarev T., Just A., Spurzem R., Berczik P., Wang L., Arca Sedda M., 2019, MNRAS, 484, 3279

Pasham D. R., Strohmayer T. E., Mushotzky R. F., 2014, NAT, 513, 74

Patruno A., Portegies Zwart S., Dewi J., Hopman C., 2006, MNRAS, 370, L6

Pelupessy F. I., Portegies Zwart S., 2012, MNRAS, 420, 1503

Pelupessy F. I., Jänes J., Portegies Zwart S., 2012, NA, 17, 711

Peters P. C., Mathews J., 1963, Physical Review, 131, 435

Peterson R. C., Seitzer P., Cudworth K. M., 1989, ApJ, 347, 251

Peterson B. M., et al., 2006, ApJ, 641, 638

Podsiadlowski P., Rappaport S., Han Z., 2003, MNRAS, 341, 385

Podsiadlowski P., Langer N., Poelarends A. J. T., Rappaport S., Heger A., Pfahl E., 2004, ApJ, 612, 1044

Pooley D., Rappaport S., 2006, ApJL, 644, L45

Portegies Zwart S. F., McMillan S. L. W., 2002, ApJ, 576, 899

Portegies Zwart S. F., Meinen A. T., 1993, AAP, 280, 174

Portegies Zwart S. F., McMillan S. L. W., Hut P., Makino J., 2001, MNRAS, 321, 199

Portegies Zwart S. F., Baumgardt H., Hut P., Makino J., McMillan S. L. W., 2004, NAT, 428, 724

Portegies Zwart S. F., McMillan S. L. W., Gieles M., 2010, ARAA, 48, 431

Press W. H., Teukolsky S. A., 1977, ApJ, 213, 183

Preto M., Tremaine S., 1999, AJ, 118, 2532

Qin Y., Marchant P., Fragos T., Meynet G., Kalogera V., 2019, ApJL, 870, L18

Quinlan G. D., Shapiro S. L., 1989, ApJ, 343, 725

Quinlan G. D., Shapiro S. L., 1990, ApJ, 356, 483

Rantala A., Pihajoki P., Mannerkoski M., Johansson P. H., Naab T., 2020, MNRAS, 492, 4131

Rantala A., Naab T., Springel V., 2021, MNRAS, 502, 5546

Remillard R. A., McClintock J. E., 2006, ARAA, 44, 49

Rezzolla L., Barausse E., Dorband E. N., Pollney D., Reisswig C., Seiler J., Husa S., 2008, Physical Review D, 78, 044002

Rice J. R., Zhang B., 2021, ApJ, 908, 59

Rizzuto F. P., Naab T., Spurzem R., Arca-Sedda M., Giersz M., Ostriker J. P., Banerjee S., 2021a, arXiv e-prints, p. arXiv:2108.11457

Rizzuto F. P., et al., 2021b, MNRAS, 501, 5257

Roberts T. P., Middleton M. J., Sutton A. D., Mezcua M., Walton D. J., Heil L. M., 2016, Astronomische Nachrichten, 337, 534

Romero-Shaw I., Lasky P. D., Thrane E., Calderón Bustillo J., 2020, ApJL, 903, L5

Roulet J., Venumadhav T., Zackay B., Dai L., Zaldarriaga M., 2020, Physical Review D, 102, 123022

Ryu T., Tanaka T. L., Perna R., Haiman Z., 2016, MNRAS, 460, 4122

Sabbi E., et al., 2012, ApJL, 754, L37

Safarzadeh M., Haiman Z., 2020, ApJL, 903, L21

Saha P., 2009, MNRAS, 400, 228

Samsing J., MacLeod M., Ramirez-Ruiz E., 2017, ApJ, 846, 36

Sana H., et al., 2012, Science, 337, 444

Sander A. A. C., Vink J. S., 2020, arXiv e-prints, p. arXiv:2009.01849

Sanders R. H., 1970, ApJ, 162, 791

Scally A., Clarke C., 2002, MNRAS, 334, 156

Shiokawa H., Krolik J. H., Cheng R. M., Piran T., Noble S. C., 2015, ApJ, 804, 85

Smith N., Tombleson R., 2015, MNRAS, 447, 598

Sørensen M., Fragos T., Steiner J. F., Antoniou V., Meynet G., Dosopoulou F., 2017, AAP, 597, A12

Spitzer L., 1987, Dynamical evolution of globular clusters

Spitzer Lyman J., Hart M. H., 1971, ApJ, 164, 399

Spurzem R., 1999, Journal of Computational and Applied Mathematics, 109, 407

Stone N. C., Küpper A. H. W., Ostriker J. P., 2017, MNRAS, 467, 4180

Stothers R. B., Chin C.-w., 1997, ApJ, 489, 319

Strohmayer T. E., Mushotzky R. F., 2003, ApJL, 586, L61

Takekawa S., Oka T., Iwata Y., Tsujimoto S., Nomura M., 2020, ApJ, 890, 167

Tout C. A., Aarseth S. J., Pols O. R., Eggleton P. P., 1997, MNRAS, 291, 732

Tremaine S. D., Ostriker J. P., Spitzer L. J., 1975, ApJ, 196, 407

Vink J. S., de Koter A., Lamers H. J. G. L. M., 2000, AAP, 362, 295

Vink J. S., de Koter A., Lamers H. J. G. L. M., 2001, AAP, 369, 574

Vink J. S., Muijres L. E., Anthonisse B., de Koter A., Gräfener G., Langer N., 2011, AAP, 531, A132

Vink J. S., Higgins E. R., Sander A. A. C., Sabhahit G. N., 2021, MNRAS, 504, 146

Volonteri M., 2010, AAPR, 18, 279

Wang L., Spurzem R., Aarseth S., Nitadori K., Berczik P., Kouwenhoven M. B. N., Naab T., 2015, MNRAS, 450, 4070

Wang L., et al., 2016, MNRAS, 458, 1450

Wang L., Kroupa P., Takahashi K., Jerabkova T., 2020, MNRAS, 491, 440

Webster B. L., Murdin P., 1972, NAT, 235, 37

Wen S., Jonker P. G., Stone N. C., Zabludoff A. I., Psaltis D., 2020, ApJ, 897, 80

Wisdom J., Holman M., 1991, AJ, 102, 1528

Woosley S. E., 2017, ApJ, 836, 244

Woosley S. E., Heger A., 2015, The Deaths of Very Massive Stars. p. 199, doi:10.1007/978-3-319-09596-7_7

Woosley S. E., Heger A., Weaver T. A., 2002, Reviews of Modern Physics, 74, 1015

Woosley S. E., Blinnikov S., Heger A., 2007, NAT, 450, 390

Woosley S. E., Sukhbold T., Janka H. T., 2020, ApJ, 896, 56

Wrobel J. M., Nyland K. E., 2020, arXiv e-prints, p. arXiv:2007.12093

Wrobel J. M., Nyland K. E., Miller-Jones J. C. A., 2015, AJ, 150, 120

Wu S. W., Bik A., Henning T., Pasquali A., Brand ner W., Stolte A., 2014, AAP, 568, L13

Yoshida H., 1991, in Kinoshita H., Yoshida H., eds, 24th Symposium on Celestial Mechanics,. p. 132

Zhong G., Marsden J. E., 1988, Physics Letters A, 133, 134

Ziółkowski J., 2008, Chinese Journal of Astronomy and Astrophysics Supplement, 8, 273

Zivancev C., Ostriker J., Kupper A. H. W., 2020, arXiv e-prints, p. arXiv:2004.06083

den Brok M., et al., 2015, ApJ, 809, 101

van den Bosch R., de Zeeuw T., Gebhardt K., Noyola E., van de Ven G., 2006, ApJ, 641, 852

Acknowledgements

I would like to thank Thorsten Naab, who supervised my PhD project and gave me much valuable advice, support and encouragement countless times. Similarly, I would like to thank Raner Spurzem for his very valuable collaboration, and the great hospitality I received when I visited his group in Beijing.

I am grateful also to my collaborators Mirek Giersz, Jeremiah Paul Ostriker, Manuel Arca Sedda, Sambaran Banerjee, Long Wang, Peter Berczik and Nicholas Stone who helped to enrich my work with suggestions and corrections.

I warmly thank all my Munich friends (listed here from nearest to furthest from my office): Tim-Eric Rathjen, Matto Frigo, Miha Černetič, Constantina Fotopoulou, Jessica Hislop, Chris Byrohl, Antti Rantala, Natalia Lahen, Kristina Lautenschütz, Pablo Sala, Oliver Emonds, Cecilia Giovani, Andreas Stoll, Alexandra Shelest, Ninoy Rahman, Jens Stücker, Sangsoo Ryu, Ulrich Steinwandel.

Thanks again to Tim-Eric, Constantina, Jessica, Antti and Alexandra for reading and correcting parts of this thesis.

A huge thank you to my family, who supported me during my studies and throughout my life.